The Pennsylvania State University
The Graduate School
College of Engineering

HIGH COUPLING D32 MODE CYMBAL TRANSDUCERS

A Thesis in
Acoustics
by
Timothy Benjamin Stonelake

Submitted in Partial Fulfillment
of the Requirements
for the Degree of

Master of Science

August 2011

The thesis of Timothy Benjamin Stonelake was reviewed and approved* by the following:

Richard J. Meyer, Jr.
Associate Professor of Materials Science and Engineering
Thesis Advisor

Thomas B. Gabrielson
Professor of Acoustics

Stephen C. Thompson
Professor of Acoustics

James F. Tressler
Special Signatory

Victor W. Sparrow
Professor of Acoustics
Interim Chair of The Graduate Program in Acoustics

*Signatures are on file in the Graduate School.

Abstract

Cymbal-type flextensional transducers are of interest to the underwater sound community because they provide a low profile, easily tunable element for integration in arrays. Cymbal-shaped caps amplify the d_{31} piezoelectric field coefficient and add it to the d_{33} coefficient, coupling these modes of a ferroelectric disk.

Recent work in single-crystal relaxor ferroelectrics has led to the discovery of a high-coupling mode in [011] poled PMN-29PT which has an excellent d_{32} coefficient, approximately two times greater than reported d_{31} values for [001] poled PMN-30PT. Integrating this crystallographically engineered cut into a cymbal-like structure promises improved projector output by amplifying this much larger piezoelectric coefficient. Additionally, the electromechanical coupling ($k_{32} > 0.9$) of this mode promises to improve the system bandwidth.

Incorporating this cut involves many possible geometric changes relative to the standard round cymbal design. This work covers the use of an FEA code to design a cymbal element that takes advantage of the improved coefficients. Models of the new cymbal design predict improvement in response of 3 dB across the band, with a further 3 dB improvement predicted if the [011] poled PMN-29PT material is used. The model of the new cymbal array with [011] poled crystal predicts an increase in effective coupling from 0.55 to 0.71 when compared to a benchmark round cymbal design.

A parametric study on the important geometric dimensions is reported, which shows predicted trends in output and coupling for each dimension. The relative strength of these relationships is reported for consideration when designing and tuning an array. Additionally, potential issues with using individual cymbal performance as an indicator of array output are presented.

Finally, an experimental study was performed on two cymbals, both a traditional round cymbal and a 'slotted' version. The results were then compared to their model predictions. A finite element simulation predicts improved output of 2-3 dB for a circular cymbal array if slots are added. This effect is attributed to a reduction in tangential stress in the slotted cymbals.

Table of Contents

List of Figures

List of Tables

List of Symbols

α	Angle of the cymbal ramp
γ	Shear strain in an elastic solid
δ	Axial strain in an elastic solid
ϵ_0	The permittivity of free space, $8.85 \times 10^{-12} \frac{F}{m}$
ϵ_{mn}^{A}	Electrical permittivity coupling electric displacement D_m with electric field E_n, measured with variable A held constant
η_{EA}	Electroacoustic efficiency
η	Loss factor, the ratio of loss modulus to storage modulus
θ	A phase angle
κ_{mn}	Electromechanical coupling for an m-n mode of operation
κ_{eff}	Effective coupling factor
κ^2	The definition of electromechanical coupling factor, often reported as $\kappa = \sqrt{\kappa^2}$
λ	Acoustic wavelength
ν	Poisson's ratio
ρ	Density
ϕ	The benchmark cymbal transducer diameter
ω	Angular frequency, $2\pi f$
a	General radius for a transducer
c	Sound speed
C	Electrical circuit capacitor, also a mechanical equivalent circuit compliance
d_c	Depth of cap for a cymbal transducer
d_h	Hydrostatic piezoelectric coefficient

d_{mn}	Piezoelectric field coefficient coupling the field E_m and the strain S_n
D_m	Electric displacement along the m face
D_f	Directivity factor
D.O.F.	Degrees of freedom
e	Euler's number
E_c	Coercive field for a ferroelectric
E_m	Electric field in the m direction
f	Frequency
f_a	Electrical antiresonance frequency, the freqeuncy of maximum $\|Z_E\|$ for a mode
f_r	Electrical resonance frequency, the freqeuncy of minimum $\|Z_E\|$ for a mode
F	Force
g	Piezoelectric voltage constant
I	Electric current
I_m	Maximum acoustic intensity
$Im\{\}$	Denotes the imaginary part of a complex quantity
j	The imaginary number, $\sqrt{-1}$
k	The acoustic wavenumber, $\frac{\omega}{c} = \frac{2\pi}{\lambda}$
ka	The product of the acoustic wavenumber and a transducer radius, not a unique constant
K_{mn}	Relative permittivity, $\frac{\epsilon_{mn}}{\epsilon_0}$
l	Length of the ramp for a cymbal transducer
L	Electrical circuit inductor, also the symbol for a mechanical equivalent circuit mass
m	Mass
P	Acoustic pressure, measured as the oscillation away from barometric pressure
q	Electric charge
Q, Q-factor	Measure of how resonant a transducer is
Q_m	Mechanical quality factor, a measure of mechanical loss
r	Radius
r_1	Apex radius for a cymbal transducer, not truly a radius for rectangular cymbals
r_2	Cavity radius for a cymbal transducer, not truly a radius for rectangular cymbals

R Electrical circuit resistor, also a mechanical equivalent circuit resistance, also the radius of a cymbal transducer

R_r Radiation resistance

$Re\{\}$ Denotes the real part of a complex quantity

s_{mn}^{A} Elastic compliance coupling strain S_m with stress T_n, measured with variable A held constant

S_{mn} Strain, deformation of the m face in the n direction

SL Source level

t Time, also the distance between two plates of a capacitor

t_c Cap thickness for a cymbal transducer

t_x Crystal thickness for a single-crystal cymbal transducer

T_c Curie temperature

T_{mn} Stress, applied on the m face in the n direction

T_m Temperature of maximum permittivity in relaxors

T_{R-T} Rhombohedral to tetragonal phase transition temperature

TFR Transmit Field Response

TVR Transmit Voltage Response

$TVAR$ Transmit Volt-Amp Response

U Volume velocity

v Particle velocity

V Voltage

w.r.t. With respect to

W Power

X_r Radiation reactance

Y Young's modulus, real or complex

Y' Storage modulus, the real part of Y

Y'' Loss modulus, the complex part of Y

Z_A Specific acoustic impedance, $\frac{P}{v}$

Z_E Electrical impedance, $\frac{V}{I}$

Z_{mech} Mechanical impedance, $\frac{F}{v}$

$[xyz]$ Electrical poling direction for a single-crystal

$<xyz>$ Crystal orientation vector

Acknowledgments

Looking back at the last two years of my life, I'm overcome with gratitude for the people that helped me arrive where I am today. I came to Penn State with the idea that I would take some classes in acoustics, a topic that had always interested me. What I have found since is a wonderful community of people who have each helped further my education and stoke my passion for the subject matter. I won't be able to name them all, but I'm going to do my best to highlight those who have helped me along this path. It is my sincere hope that those I've failed to mention here understand that I am grateful nonetheless.

To begin, I must thank the Graduate Program in Acoustics. Specifically Dr. Vic Sparrow, who has served diligently both as chair of our program, as well as one of my professors. Additionally, Karen Thal has been a valuable source of guidance in navigating the program and the graduate school as a whole. She has also offered invaluable laughs and an open door when I needed to talk.

When I came to interview with the program, I met with Dr. Rich Meyer to discuss some research opportunities. I knew immediately that we shared an interest in transducers and an appreciation for candid communication. In the years since, he has exceeded my expectations for an advisor, offering thoughtful guidance in matters well outside the scope of our work together.

Dr. Steve Thompson also spoke with me when I was first considering Penn State. He was a solid influence then in bringing me here, and has taken unselfish interest in my career since. Dr. Tom Gabrielson's class on transducers was integral in my development as an acoustician. I can only hope that over the course of my career I will be able to understand and explain these devices on a level approaching his. Dr. Steve Garret has inspired me to always push for a deeper understanding of the subject, and I am glad to call him a friend as I leave Penn State.

In the process of writing this document, Dr. Jim Tressler has been a source of insight and advice on the sometimes confounding practical side of these devices. I am grateful that he agreed to serve on my committee for this project, as the thesis that follows has benefited greatly. I would be remiss if I didn't thank my colleagues Doug Markley, Dr. Nevin Sherlock, Dr. Scott Porter, Zach Lowe, Tom Tremper, Tara Tubbs, Nik Vitt, Mike Wilson and, of course, Teresa

Homan for all their help along the way. Additionally, I am thankful for the generous support of the Office of Naval Research, the U.S. Naval Research Laboratory, and the Eric Walker Walker Assistantship program through Penn State ARL.

I have met some wonderful people during my time in State College. My fellow Acoustics students have been great friends, and frequently great mentors. We've grown together over the past two years, and I expect this bond to hold as we all move forward with our careers. I also want to thank all of the kids in Full Ammo Improv for allowing me to perform with them this past year. It was great fun, and a wonderful distraction. To my friends away from Penn State, thank you for your continued support. Specifically, Chris, Danielle, Elise, Jon, and Rachel were wonderful in encouraging me during my time here.

Finally, and most importantly, I must thank my family. My father has always been a strong influence in my academic life. Without him I likely wouldn't find myself a scientist and engineer, and I can credit him with my continued curiosity. My mother has been wonderful as well, teaching me over the years to be self-sufficient and to never take myself too seriously. They both have supported me lovingly throughout my life and education, and I will be forever indebted to them. To my brothers, and their significant others, thank you for your continued support and advice. You have all helped form who I am today. My extended family has been and continues to be a wonderful influence in my life, and I love you all.

"I never learn anything talking. I only learn things when I ask questions."

-Lou Holtz

Chapter 1

Overview, Objectives & Background

1.1 Hypothesis and objectives of this work

Single-crystal relaxor ferroelectrics show great promise in the field of underwater electroacoustic transduction. Their superior coupling and piezoelectric coefficients make them attractive materials for designers, but continued research must be done to prove their utility over PZT in harsh application environments. The purpose of this work is to utilize a particularly favorable crystal cut by integration into a transducer that has been designed for the properties of interest. [011] poled $0.71Pb(Mg_{1/3}Nb_{2/3})O_3$-$0.29PbTiO_3$ has an excellent d_{32} coefficient (-1880 pC/N) as well as high coupling in that direction ($\kappa_{32} = 0.94$) [1]. The transducer targeted is a variation of the *cymbal* (Fig. 1.1), developed at The Pennsylvania State University in 1995.

The hypothesis of this work is that these superior properties of [011] poled PMN-29PT crystal[1] will allow for improved transducer output and efficiency with the proper cymbal cap design, when compared with a known transducer array currently using [001] poled PMN-30PT crystal[2].

1.2 Brief history of electroacoustic transduction

Transduction is the process of converting energy from one form to another. In the case of this work, the conversion is from electrical energy, in the form of voltage and current, to acoustic energy, in the form of acoustic pressure and particle velocity. This is referred to as electroacoustic transduction.

F. V. Hunt speculates that the earliest form of electroacoustic transduction known to man was the electric spark [3]. In an acoustic medium such as air or water, a spark will excite waves of tremendous frequency content. This makes it a very useful source of sound. However, the

[1] A common shorthand for solid solution single-crystal systems is to dictate the constituent crystal by the first letters of its elements (PMN in this case for $0.71\mathbf{P}b(\mathbf{M}g_{1/3}\mathbf{N}b_{2/3})O_3$) and then a number for the percent of the lower population unit cell, along with the first letters of its elements (29PT for $0.29\mathbf{Pb}\mathbf{T}iO_3$). The O for oxide is assumed. In addition, as properties vary with poling direction, poling is specified out in front of the shorthand.

[2] Shorthand for $0.70Pb(Mg_{1/3}Nb_{2/3})O_3$-$0.30PbTiO_3$

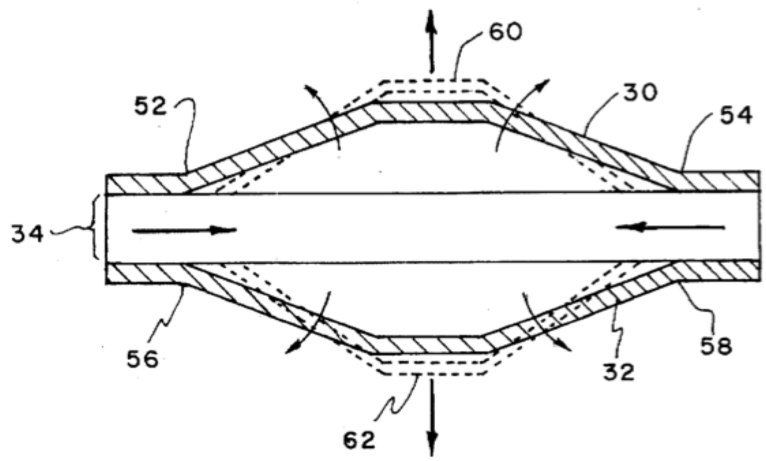

Figure 1.1. A cymbal transducer. The relative motion of the active material (center) and the caps (top and bottom) are shown. The standard cymbal is axis-symmetric about the vertical line of action. From U.S. patent #5,729,077 [2].

non-linear nature of the event and the difficulty in transmitting complex or continuous sequences can be quite limiting.

Excluding the spark, there are five commonly recognized classes of electroacoustic transduction: electrodynamic, electrostatic, electromagnetic, magnetostrictive, and piezoelectric[3]. Putting off piezoelectric for the time being, the remaining four are dealt with in order of their major breakthroughs. For a more engaging and thorough history of electroacoustic transduction, the reader is referred to Hunt [3].

1.2.1 Electrostatic

The first electrostatic acoustic transducer was invented by Benjamin Franklin in 1747 [3]. He constructed a metal ringer suspended between two bells, each mounted to the outside of a Leyden jar[4]. When a charge was built up on the outside of one of the jars, the ringer would be attracted to it until it touched, and the charge would be balanced through conduction. At this point the ringer would hold a different charge from the jar at the opposite end of the gap, which would lead to an electrostatic attraction resulting in it striking and sharing its charge with the opposite jar. This action would continue until there was no longer a charge (and therefore potential) difference between the jars. Capacitors, and consequently electrostatic transducers, are sometimes called condensers because they rely on the *condensation* of charge on one side of the circuit.

[3]Sometimes piezoelectric is split into piezoelectric and electrostrictive to create six classes. Their differences and the reason for lumping them together will be treated later. Another unique design not included in these classes is the carbon button microphone, which is a form of variable resistance transducer.

[4]The Leyden jar was an early form of capacitor, which could store static charge between inside and outside electrodes on the jar.

As is implied above, electrostatic transducers are also referred to as capacitive transducers because their common implementation is a form of variable capacitor. It is made by separating two parallel conducting plates and applying a voltage. As the voltage changes, the gap-dependent capacitance will also change to balance the charge on the plates. In this way, the electrostatic transducer can be used as a projector, as applying an alternating voltage causes one of the plates to move and the vibration can be coupled to an acoustic medium. Similarly the transducer can be used as a sensor, where an acoustic wave moves one of the plates and causes an alternating voltage at the terminals.

1.2.1.1 The condenser microphone

Condenser microphones are the most popular example of electrostatic transducers. E. C. Wente developed what has become the modern condenser microphone in 1916 [4]. He conceived of a flexible conductive diaphragm suspended closely to a fixed rigid backplate. The major difference between this and the earlier implementations of Thomas Edison and A. E. Dolber[5] is that Wente tuned his diaphragm resonance far above the frequency band of human speech[6] to approximately 16 kHz. This was accomplished by making an extremely narrow gap (0.0005") which acted as a relatively stiff air film (Fig. 1.2). Because the surface area of the air film was quite high in relation to its volume, the viscous and thermal losses were higher than in previous condensers. This blunted the frequency response of the diaphragm at resonance causing the flatter[7] curve indicative of modern condenser mics. It is the ability to achieve wide-band flat response that has made the condenser microphone dominant in both recording studios and in-air laboratory measurement markets to this day.

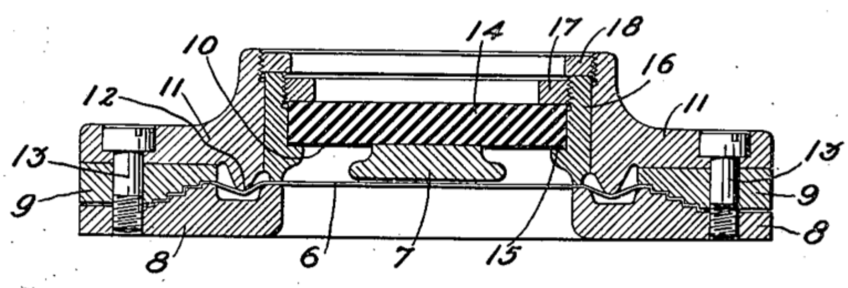

Figure 1.2. E.C. Wente's condenser microphone, showing the diaphragm (6) and back plate (7). From U.S. patent #1,333,744 [4].

[5] Edison and Dolber developed electrostatic transducers for early telephone transmitters.

[6] The voice-frequency band of telephony is 300-3500 Hz.

[7] *Flat* frequency response is a reference to the shape of the curve when response is plotted vs. frequency for a transducer. Wente describes the ideal frequency response as "a line parallel to the axis of frequency" in his patent.

1.2.1.2 Langevin's singing condenser

The tragedies of the Great War and the Titanic in the early 20$^{\text{th}}$ century led to a number of concepts for detection of submerged threats, either man-made or natural. While this had been done in 1914 by Fessenden and others, their use of low-frequency sound limited the size of objects that could be detected. In 1915 Paul Langevin, an accomplished physicist in France, undertook the project of making a transducer to test an ultrasound echo-ranging scheme proposed by Constantin Chilowsky [5]. Chilowsky conceived of operating a projector at 40 kHz, which would require significant transmit power due to the high attenuation of ultrasound in sea water. Langevin created a "singing condenser" capable of producing this output, but its design was troubled by issues of electric breakdown under the large electric fields required. After some successful tests with the singing condenser as a projector, Langevin turned his attention towards a piezoelectric drive element.

1.2.2 Electromagnetic

In 1820, Hans Christian Øersted discovered that electric current passing through a wire in the vicinity of a magnetic needle could produce motion in the needle [6]. His work marked the first formal experimentation determining the relationship between electricity and magnetism, now known as the field of *electromagnatics*. This discovery led to tremendous research in the field by some of the top minds of the time such as: Ampere, Ohm, Faraday, and Maxwell.

1.2.2.1 The electromagnet

A key step towards electromagnetic acoustic transduction was the invention of the electromagnet in 1824 by William Sturgeon. It is interesting to note that the idea of inducing magnetism in a piece of iron had been known prior to Sturgeon's electromagnet [3], and despite the fact that Sturgeon is credited as the inventor of the electromagnet, his invention is listed simply as an "improved electro-magnetic apparatus" [7]. His important contribution was the discovery that by coiling wire around a soft iron core, much greater magnetic forces could be generated than if the coil of wire was used without a core. Though it wasn't fully understood at the time, this was a result of magnetic domain motion under the influence of the electric current induced magnetic field. Magnetic domains are groupings of atoms or unit cells in a material that have aligned magnetic fields. As a magnetic field is applied across the bulk material, these domains will attempt to align with that field. This domain motion accounts for the significantly higher magnetic permeability that characterizes materials which make good cores.

1.2.2.2 The telegraph

The electromagnet would become a key component in the development of the telegraph. A charged electromagnet attracted a striker causing a bell to ring out the transmitted code (Fig.

1.3). Hunt credits Henry as the first to arrive at this arrangement, but history has remembered the name of Samuel Morse [3].

Fig. 5.

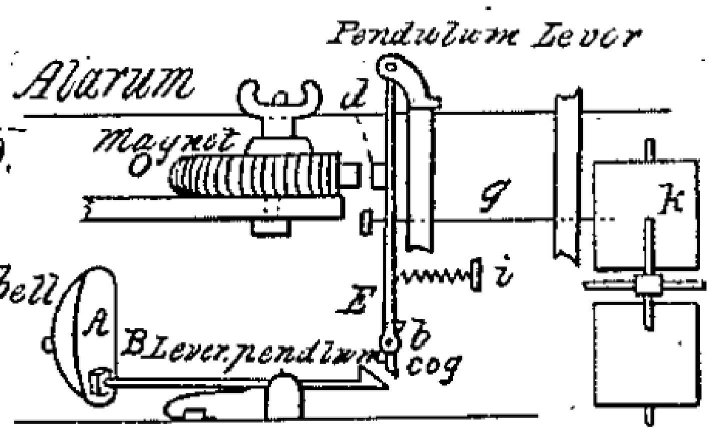

Figure 1.3. An electromagnet striker, as patented by Samuel Morse in 1840. From U.S. patent #1,647 [8].

1.2.2.3 Moving armature transducer

Alexander Graham Bell patented the first telephone system in 1876 [9]. In his telephone he used a moving armature device as both the transmitter and the receiver (Fig. 1.4). This system was short lived, as carbon button and condenser microphones eventually provided superior speech intelligibility.

While Bell's microphone was quickly usurped, descendants of the moving armature design have continued to have success as a loudspeaker because of how efficiently they can be packaged. The elegant *balanced armature* transducer offers a push-pull variation on the variable reluctance moving armature. This allows for some harmonic cancellation and near-linear low level drive [3]. Modern balanced armature transducers are small enough to be fit comfortably in the ear, which has lead to many in-ear designs for hearing aids and high-end earphones.

1.2.3 Electrodynamic

The term *electrodynamic* is somewhat misleading when considering the previous discussion of transducers. While electrostatic and electromagnetic transducers derive their names from the type of force used to create motion, the electrodynamic transducer does not. It is actually powered by magnetomotive force, which is generated from an electrical current. It's name was likely given simply as a description of the input electrical energy (electro-) and motional output (-dynamic).

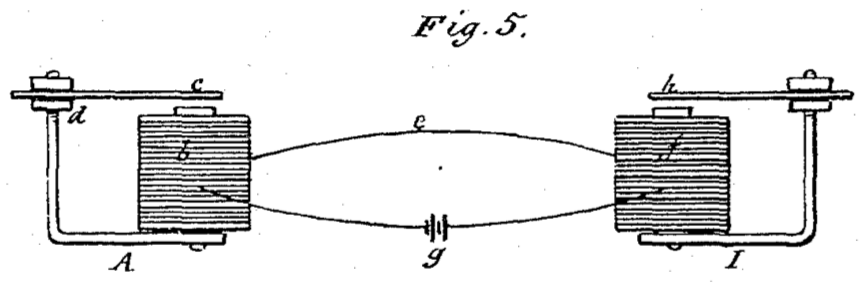

Figure 1.4. Bell's system of telephone transducers. Taken from U.S. patent #174,465

An example of a simple electrodynamic transducer is a clamped bar of magnetized iron with a wound coil of wire suspended around it. When current is passed through the wire, a magnetic field develops which causes a force on the magnetized bar (Fig. 1.5). The coil feels an equal and opposite force, causing it to move. This implementation of transducer is so prevalent, that the terms electrodynamic and 'moving coil' are used interchangeably.

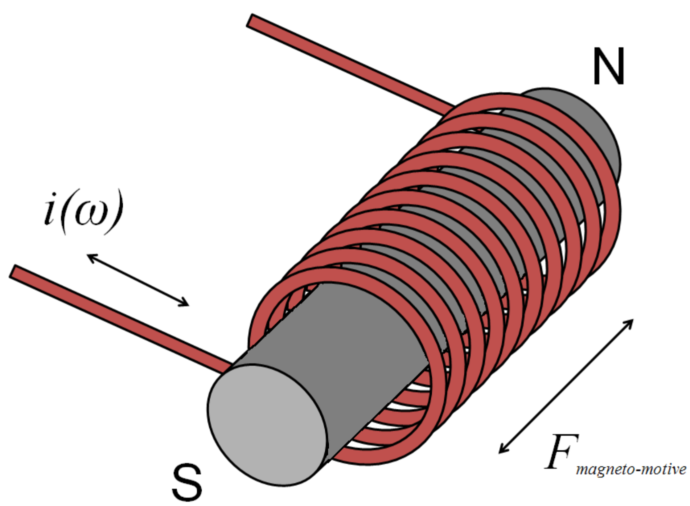

Figure 1.5. A basic electrodynamic transducer. The north (N) and south (S) poles of the magnet are labeled. The oscillating current (i) produces a magnetomotive force (F).

1.2.3.1 The moving-coil loudspeaker

Ernst Siemens patented the "magneto-electric apparatus" described above in 1874 [10]. While he listed his device as a motor, he would later realize its utility as an electroacoustic transducer after others adapted it for telegraphy. Expanding on his original design, Siemens went on to file patents in England and Germany describing many details of the modern loudspeaker [3].

1.2.3.2 The Fessenden Oscillator

The first effective use of electrodynamic transduction underwater was by Reginald Fessenden in 1914 [11]. "The Fessenden Oscillator", as it would later be known, was made up of a plate struck by a moving plunger, which was suspended inside wound coils. Fessenden designed it as a solution to the problem of generating low frequency sound on-board ships. It was known at the time that as the frequency of sound drops, the distance it can travel increases. For this reason, large bells and longitudinal bar vibrators were used as signal generators. The problems with each are detailed by Fessenden in his patent application. He explains that as bells become larger, and necessarily thicker, their vibration efficiency drops off, and that while bars remain efficient at large sizes, their lengths can become unwieldy.

Fessenden's solution was to use the mass of the plunger to drive the resonance frequency of a moving coil circuit down, targeting operation at frequencies less than 500 Hz. By doing this he was able to achieve a much more compact transducer than those which were in use at the time, which would allow the oscillator to be mounted on the hull of a ship. Its utility was proven the same year as his patent filing when an iceberg was detected approximately two miles from the transducer by the U.S. Coast Gaurd cutter *Miami* [12].

1.2.4 Magnetostrictive

Magnetostriction was first reported by J. P. Joule in 1842. He ran a series of experiments at the urging of a local machinist, F. D. Arstall, to determine if the application of alternating magnetic field could be used to produce motive power [13]. This led to the formal discovery that iron and steel elongated under the influence of a magnetic field[8]. Joule found that the elongation is proportional to the length of the sample and the square of the magnetic intensity.

1.2.4.1 Ferromagnatism and natural occurrence

Ferromagnetic materials are those that can be made into permanent magnets by the application of an external magnetic field. This is due to magnetic domains in the material, described above. All ferromagnetic materials exhibit magnetostriction to some extent, though it is often so small that it is of little use. The strain in iron measured by Joule was only 1.4 ppm[9]. This was due to both the limited magnetostriction coefficient of iron and the strength of the magnetic field that Joule could achieve.

Magnetostrictive materials demonstrate increased strain as the magnetic field strength is increased. In low fields, the strain is quadratic with increasing field. This tapers to a linear relationship before eventually leveling off at magnetic saturation. At this point, maximum domain

[8]This was another 'discovery' of a phenomenon that had been known at the time, but not yet studied to the point of understanding its fundamental relationship.

[9]In more traditional terms, 0.00014% strain

motion has been achieved and further increase in the magnetic field strength will not produce more strain. The converse of this is also true, and generation of a magnetic field through strain is called the Villari effect.

Over time, other elemental metals, such as nickel and cobalt, were found to have measurable magnetostriction. Nickel, in particular, was used as an underwater transduction material during World War II due to its superior strength compared to quartz, the best piezoelectric material at the time [14]. Throughout the years since, engineers have gone back and forth between magnetostrictive and piezoelectric materials when deciding if strength or output efficiency is more important. Several of the more recently developed magnetostrictive materials show promising strain and increased temperature stability.

1.2.4.2 TERFENOL-D

TERFENOL-D® is often referred to as a giant magnetostrictive material because of its relatively large strains compared to elemental metals. Its name is derived from the alloys that comprise it and the location where it was discovered: terbium (TER), iron (FE), the Naval Ordnance Laboratory[10] (NOL), and dysprosium (D) [15]. Terfenol-D[11] exhibits the largest strain of any known magnetostrictive material at 800-1200 ppm. Its large strain, good coupling (κ=0.75), and high mechanical impedance make it a useful material for underwater applications.

1.2.4.3 Galfenol

Galfenol[12] derives its name from its constituent elements in a similar way to Terfenol-D. An alloy of gallium and iron, it was developed at the Carderock Division of the Naval Surface Warfare Center in 1998. While it does not have the superior magnetostriction of Terfenol-D at 300 ppm strain, it offers increased temperature stability [16] and magnetic permeability compared to Terfenol-D. The room temperature relative magnetic permeability for Galfenol ($\mu_r = 60 - 70$) is approximately eight times the value for Terfenol-D ($\mu_r \approx 9$) [17]. In addition, Galfenol has superior strength and machinability. Recent studies of Galfenol seek to take advantage of these properties in the abusive high-drive applications where piezoelectrics may not be able to survive.

1.3 A slightly less brief history on piezoelectricity

1.3.1 Pyroelectricity

1.3.1.1 The direct effect

The attractive properties of certain crystals were known in the ancient world, though not understood. Due to an incomplete record of history (and the limited understanding of those observing these properties) the specific crystals in question are debatable [18], but many document

[10] The Naval Ordnance Laboratory is now known as the Carderock Division of the Naval Surface Warfare Center
[11] $Tb_{0.3}Dy_{0.7}Fe_{1.92}$
[12] $Fe_{1-x-y}Ga_xAl_y$ ($x + y < 0.3$)

the most well-known to be tourmaline [3, 19, 20]. When placed in a fire, it would attract ash for some period of time, at which point it would cease doing so and the ash would fall away.

This curiosity was noted by many throughout history, but the first formal study of it being electrical in nature is credited to Aepinus in 1756 . He found that when heated, opposite ends of a crystal would have opposite polarities. John Canton was the first to show that this electrical polarization is only present during a change in temperature, noting also that cooling would cause a similar effect of opposite polarity.

Lord Kelvin offered the first theory on the nature of pyroelectricity in 1860 [21], stating that there must be some form of permanent polarization in pyroelectric crystals. When Canton was performing his experiments, he found that by fracturing a pyroelectric crystal which had been electrically poled, two or more crystals were obtained that each had positive and negative poles. Kelvin argued for the idea of *bodily* polarization from these results, stopping short of the molecular polarization theories that would soon follow. This theory was of great interest to many physicists and crystal chemists of the time. One of the chemists was Charles Friedel, for whom Jacques Curie started working as an assistant in 1877 [20].

1.3.1.2 The electrocaloric effect

The converse pyroelectric effect, the *electrocaloric* effect, is the generation of heat in a pyroelectric crystal as it is moved in an electric field. This was theorized by Kelvin in 1877 [21], after further consideration of the pyroelectric phenomena. Gabriel Lippmann gave a theoretical analysis of this effect based off of conservation of charge in 1881 [20].

1.3.2 Piezoelectricity

1.3.2.1 Discovery

In 1880, the Curie brothers reported the development of polar electricity in crystals when pressure was applied along their hemihedral axes[13] [24]. Their original experiment was carried out on then well-known pyroelectric materials: blende, sodium chlorate, borax, tourmaline, quartz, calamine, topaz, right-handed tartaric acid, sugar, and Rochelle salt. When electroded samples were compressed in a vise, they observed that one of the electrodes became positively charged, and the other would become negatively charged. If the sample was then "decompressed" (i.e. put in tension), the relative charge on the electrodes flipped in sign. The term *piezoelectricity* was coined by the physicist W. G. Hankel shortly after the Curies published these results [25].

1.3.2.2 The converse effect

A natural progression of Lippmann's theoretical analysis of pyroelectricity led him to predict the converse piezoelectric effect in 1881. It was proven experimentally by the Curies shortly after

[13]Several terms from the field of crystal chemistry will be employed throughout this thesis. A thorough discussion of crystal systems is outside the scope of this work. The interested reader is referred to Jaffe [22] and the former IEEE Standard on Piezoelectricity [23].

this predicition [20]. Despite its myriad uses, the converse piezoelectric effect has not found a catchy shorthand similar to the electrocaloric effect.

1.3.3 Ferroelectricity

Kingery, et al. define ferroelectricity as "the spontaneous alignment of electric dipoles by their mutual interaction. This is a process parallel to the spontaneous alignment of magnetic dipoles observed in ferromagnetism and derives its name from its similarity and features analogous to that process" [26]. Crystals are considered *ferroelectric* if they have a spontaneous electric dipole that can be shifted in orientation by application of an electric field. The ability to change the orientation of these dipoles was first studied by Valasek in the early 1920's [27, 28]. His work was done with Rochelle salt, a naturally occurring piezoelectric material, and while showing the possibility of further alignment of piezo-crystal dipoles, it also opened the door for study of dipole alignment in materials that did not exhibit piezoelectricity.

In ceramics made from piezoelectric crystallites, these spontaneous dipoles would be randomly oriented upon firing, making them useless active materials as-fired. However, utilizing their ferroelectric properties, the dipoles can be aligned on a somewhat permanent basis by application of a strong electric field and under elevated temperature. Ferroelectric ceramics can then be made into useful piezoelectric materials by *poling* them in this way.

By the middle of World War II, ferroelectricity in barium titanate, $BaTiO_3$, was being studied independently in the United States, England, Russia, and Japan [29]. It was around this time that R. B. Gray discovered the ability to induce a permanent bias on $BaTiO_3$ by use of a strong electric poling field and application of mechanical stress while cooling the material through it's Curie temperature, T_c [30]. The significance of the Curie temperature will be dealt with shortly. For a complete and concise history of ferroelectric development, the reader is referred to Cross and Newnham [31].

1.3.4 An aside on electrostriction

There can be some confusion on the differences between electrostriction and piezoelectricity. Both involve induced strain in materials when an electric field is applied across them. W. G. Cady states succinctly: "*electrostriction* in dialectrics applies to any interaction between an electric field and the deformation of a dialectric in the field" [19]. Put in these terms it seems that any dielectric material can exhibit electrostriction, and piezoelectric materials would simply be a subset. However, Cady further explains that the accepted difference between the two is that in electrostrictors, (1) the direction of the strain is independent of the polarity of the applied field and (2) the strain is proportional to the square of the field. In piezoelectrics, the direction of the strain follows the polarity of the electric field (i.e. negative field gives negative strain and vice versa), and the relationship is linear. This is shown in Fig. 1.6.

While the distinction above would call for these two phenomena to be treated separately, electrostrictors can be made to behave as though they were piezoelectric. By applying a DC

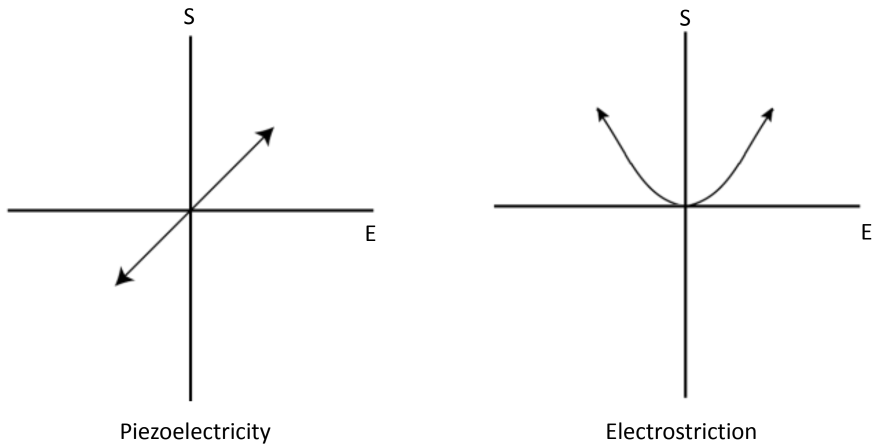

Figure 1.6. Strain (S) in piezoelectric and electrostrictive materials vs. applied electric field (E).

offset voltage, the material will move into the steeper portion of its strain vs. field curve. By then applying an AC signal, the material can be made to exhibit quasi-linear strain about this offset point. This is demonstrated in Fig. 1.7.

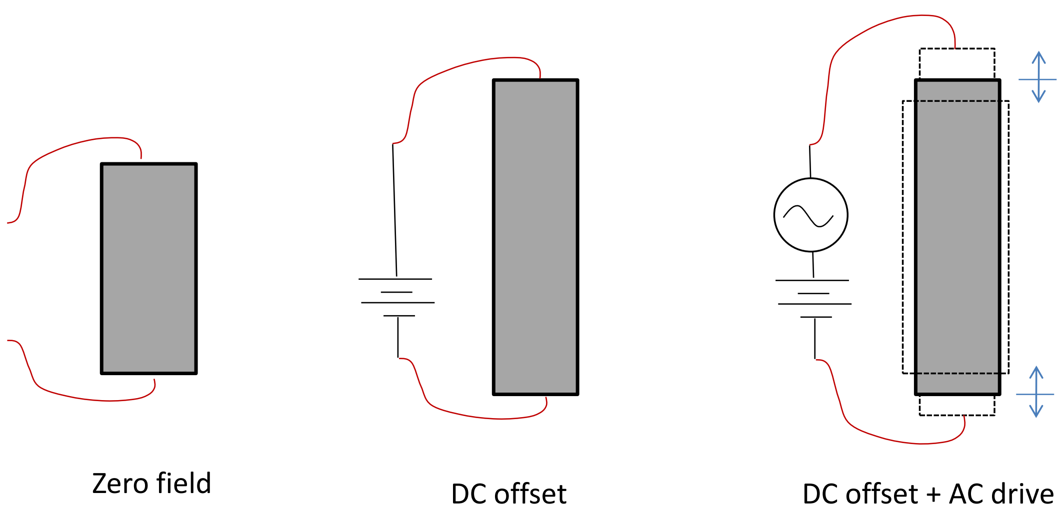

Figure 1.7. Operation of a electrostrictor with a DC offset.

1.3.5 PZT

$BaTiO_3$ dominated the field of ferroelectrics until the advent of lead zirconate titanate (PZT). In 1954 Bernard Jaffe, et al. detailed the piezoelectric properties of $Pb(Zr_{0.55}Ti_{0.45})O_3$, demonstrating a T_c of 350^{o}C [32]. To this day, the relatively high T_c (compared with $BaTiO_3$, at approx. 130^{o}C) proves to be PZT's greatest asset as an active material[14].

PZT is a solid solution crystal system with a perovskite unit cell. The Zr^{4+} or Ti^{4+} atoms sit at the center of the unit cell, surrounded by octahedral O^{2-} atoms on the faces and Pb^{2+} at each of the corners. This is shown in Fig. 1.8.

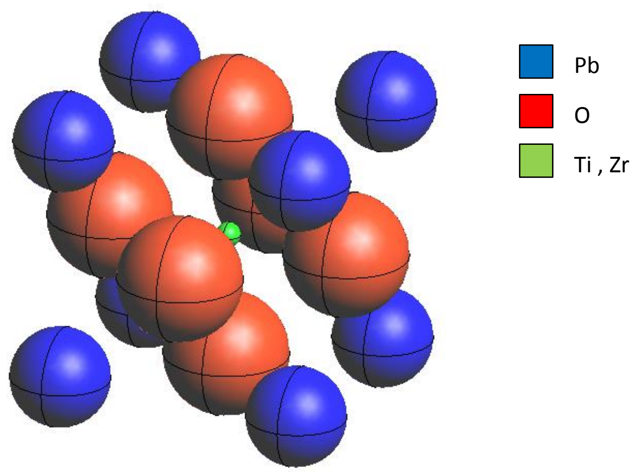

Figure 1.8. An example of the perovskite unit cell for PZT.

Above its T_c, PZT is cubic with no spontaneous polarization. Below its T_c, PZT is either tetragonal or rhombohedral depending on its relative zirconate/titanate content[15]. In either of these crystal classes, the distortion from cubic causes an asymmetry of the Zr^{4+} or Ti^{4+} atoms and oxygen lattice. This asymmetry is the basis of the spontaneous polarization of PZT. The composition boundary between two crystal states is called the *morphotropic phase boundary* (MPB). Near its MPB, at approximately 52% zirconate [33], PZT displays peaks in many piezoelectric properties, notably: permittivity, piezoelectric field coefficient (d), and coupling[16].

1.3.5.1 Hard vs. soft

Resistance to depoling, which is the electric field at which aligned dipoles of a poled material would begin to flip orientation, is often described by how *hard* or *soft* a material is. Harder materials are more resistant to depoling, have lower dielectric loss, lower piezoelectric response,

[14] T_c is a function of crystal composition. To obtain more stable and useful compositions of PZT the T_c often ends up lower than 350^{o}C.

[15] There is also the antiferroelectric orthorhombic phase at high or pure zirconate content. Discussion of this phase is not relevant to this work.

[16] For an explanation of the piezoelectric properties, the reader is referred to the theory section in Chapter 2.

lower electromechanical coupling and higher T_c. Softer materials are less resistant to depoling, have high dielectric loss, higher piezoelectric response, higher coupling, and lower T_c. These property changes can be brought about by donor or acceptor doping the material [34], or relative distance from the MPB [35].

With a large variety of compositions possible, it became important for the US Navy to standardize these properties for transducer design, which they did most recently in MIL-STD-1376B(SH) [36]. This standard was canceled in 1999, but has yet to be replaced at the time of this writing. It is still widely referenced for discussion of Navy Type ceramics. Under this standard, the PZT compositions from harder to softer are: Type III, Type I, and Type II. Under their more common names, adopted as a form of slang from their names under Vernitron, Inc. [37], these would be: PZT 8, PZT 4, and PZT 5. These names are now owned by Morgan Technical Ceramics, though they also refer to their materials by the more specific Navy types in their product literature [38].

1.3.5.2 Limitations

The most obvious limitation on ferroelectrics is the *coercive field*, E_c. The coercive field is defined as the electric field under which depoling results. When trying to drive a previously poled material with a high voltage AC signal, the amplitude of the signal cannot exceed the coercive field unless a DC offset is used. Further complicating matters, the coercive field is a function of temperature. Driving ferroelectrics hard leads to increased temperature, which leads to a decreased coercive field. In practice, the driving field would be reduced from E_c by a factor of safety for sustainable operation.

Piezoelectric ceramics can also suffer in application due to their brittleness. Designers often have to make concessions and modifications to bias the stress imposed on the active material. By placing a compressive stress bias on the material, tension can be avoided during the AC operation of the device. An added complication is that there is not a lot of good data on the failure strength of PZT. As a ceramic, strength would usually be determined by 4 point bending, but the electromechanical interaction of poled PZT can influence results [39].

Aging is another property of concern in poled ceramics. As the internal dipoles of each crystallite are aligned through domain motion, there are internal stresses built up. To a certain extent, these stresses will be relieved through time, mechanical stress, and electrical drive [37]. For this reason, there are standard methods of measuring aging rates of ceramics, so expected lifetime at a certain performance level can be estimated [36].

Finally, novel ceramic science has led to a wide variety of properties in PZT for its many applications. There is a limit, however, to how close ceramic poling can get to the ideal properties of a unit cell. Incomplete reorientation leads to limits of 83-91% of possible domain alignment depending upon the phase of the crystal [35]. In addition to polarization limits, there are also limits to the fraction of single crystal distortion that can be achieved [29] . These limitations led to the study of crystallographically engineered single crystal ferroelectrics.

1.3.6 Single crystal ferroelectrics

1.3.6.1 Relaxors

Traditional ferroelectrics exhibit a maximum in dielectric permittivity at their T_c with a sharp drop above this temperature. This is indicative of the phase change they undergo when passing through the Curie temperature. Relaxor ferroelectrics have a similar peak in permittivity at T_m, but do not show a dramatic drop off above. Instead they have a broad peak and slow drop in permittivity. The designation of T_m distinguishes this temperature of maximum permittivity in relaxors from T_c. T_m is also frequency dependent, causing dispersion in the permittivity curve [40].

Relaxors show hysteresis at low temperatures, as is expected in ferroelectrics. However, instead of a static drop in hysteresis above T_c, relaxors show a slow decay in hysteretic behavior as temperature is increased. This slow decay of hysteresis with temperature is also a defining characteristic of relaxors. Those interested in further study of relaxor materials are referred to Cross [40].

1.3.6.2 Discovery

These relaxor properties were first discovered by G. A. Smolensky, et al. in 1959. During the study of the dispersive permittivity curves in PMN[17], it was found that the material exhibited large electrostrictive strains as well [40].

The first work on single crystal growth of relaxors was carried out in the late 1960's by Nomura, et al. [41]. Though a formal definition of relaxor materials hadn't been determined at that point, Nomura was working with PZN-PT[18], which has a MPB in the range of 9-9.5% PT. Following up on this work, Kuwata, et al. confirmed the MPB and reported on the high piezoelectric and dielectric properties [42].

Similar to PZT and PZN-PT, PMN can be formed as a solid solution with lead titanate, and has a MPB. In Fig. 1.9 the phase diagram for the PZT and PMN-PT systems can be seen, with B_1 being Mg and B_2 being Nb in this case. $Pb(B_1B_2)O_3$ is a general chemical formula for lead based relaxors, and Yamashita lists many possible formulations [43].

The first reported growth of usable single crystals of PMN-PT was in 1990 by Shrout, et al. [44]. In this work, it was found that single crystals up to 1 cm on a side could be grown by the flux technique with a composition close to the MPB of the PMN-PT system. In 1997, Park and Shrout reported excellent strain capability and high piezoelectric coefficients ($d_{33} > 2500$ pC/N) in single crystal PMN-PT [45]. This was truly a breakthrough, as practical single crystal growth of PZT in hopes of achieving similar properties had been unsuccessful. In addition, this piezoelectric field coefficient was over twice what was reported for PZN-PT by Kuwata.

[17] Lead magnesium niobate, $PbMg_{1/3}Nb_{2/3}O_3$

[18] $Pb(Zn_{1/3}Nb_{2/3})O_3$-$PbTiO_3$

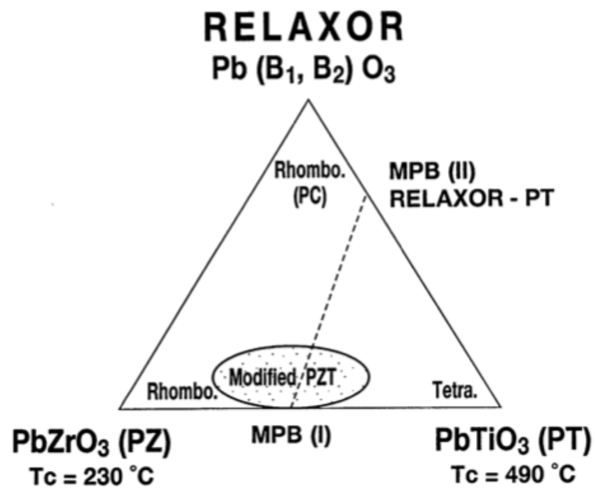

Figure 1.9. A morphatropic phase boundary diagram (MPB) of PZT and PMN-PT. From [43]

1.3.6.3 Orientation and poling

Crystal orientation is given as a vector representation of the unit cell. In the case of a cubic cell, the three basis vectors <100>, <010>, and <001> can be seen in Fig. 1.10 originating from the cube-centered atom and exiting three of the cube faces. The direction <111> is also seen originating at the center of the cube and traveling through the corner defined by the other three vectors.

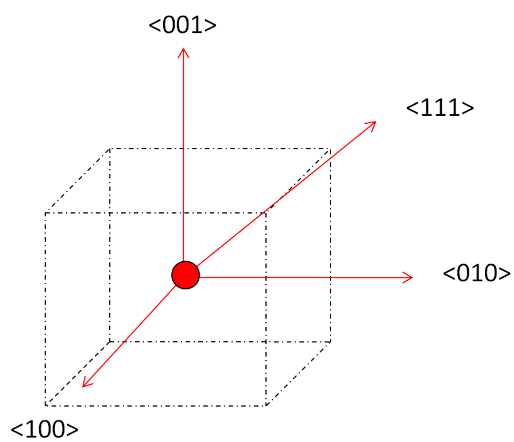

Figure 1.10. Poling orientation shown as vectors in a cubic unit cell.

In piezo- and ferroelectric crystals, there can be many possible domain polarizations depending on the phase. The poling vector is given to denote the overall or average polarization direction given the possible states. It is assumed that when a field is applied, the polarization vector will fall into the closest possible polarization direction, and that when averaged over the whole crystal the result will be in the direction of the poling field. For example, [001] poled single crystal PZN-PT is shown in Fig 1.11. The possible domain directions and the overall direction of <001> are shown with a given applied field. It is common practice to report crystal orientation within <> and poling direction within [ ].

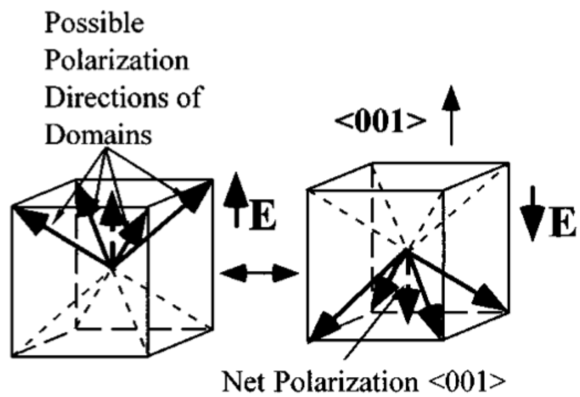

Figure 1.11. Possible domain states and overall poling direction in rhombohedral PZN-PT. From [45].

It is obvious from the above that all poling directions will not necessarily be equal, as the polarization directions that the crystal 'wants' to fall into are based off of its orientation and phase. Piezoelectric properties of the material thus depend on the material composition, the orientation of the crystal cut, and the poling direction. An excellent overview of possible polarization domains is given by Zhang [46]. In addition, the impact of poling on piezoelectric, dielectric, and loss properties of PMN-30PT and PMN-26PT is reported[19].

1.3.6.4 [011] poled PMN-PT

In 2000, Lu, et al. reported an extremely high negative d_{31} coefficient in [011] poled PMN-33PT [47]. Lu also reported a positive d_{32} coefficient, which differentiates the [011] poling from the [001] direction, where both transverse coefficients are negative. With differences in sign between the two transverse terms, distinction between d_{31} and d_{32} becomes necessary. Despite Lu's convention, the positive transverse term will be d_{31} and the negative will be d_{32} for the remainder of this work.

A complete set of elastic, dielectric and piezoelectric properties for [011] poled PMN-29PT was reported by Wang, et al. in 2007 [1]. Wang's work represented the first complete set of properties for [011] poled material. While both PZN-PT and PMN-PT exhibit large d_{32} coefficients when poled along [011], PMN-PT was chosen for this work because it is more stable and more easily grown.

[19] Zhang uses another convention in his paper, where PMN-30PT is written simply as PMNT30.

1.3.6.5 PIN-PMN-PT

Though excellent coupling and piezoelectric field coefficients can be achieved for PMN-PT near its MPB, the relatively low E_c is problematic. In light of this, several other crystal systems are under study to find one that is more stable and has comparable properties to PMN-PT. Three of the systems currently being studied are $Pb(Sc_{1/2}Nb_{1/2})O_3$-$PbTiO_3$ (PSN-PT), $Pb(In_{1/2}Nb_{1/2})O_3$-$PbTiO_3$ (PIN-PT), and $Pb(Yb_{1/2}Nb_{1/2})O_3$-$PbTiO_3$ (PYN-PT). PIN-PT became of further interest when it was found by Guo, et al. that large crystals could be grown through the Bridgman method when using PMN-PT seed crystal [48]. The result was PIN-PMN-PT[20] with $T_c > 200^oC$.

In 2008, Zhang, et al. at Penn State reported a complete set of material properties for PIN-PMN-PT [49]. With a slight reduction in piezoelectric activity, a higher coercive field ($E_c \approx 5.5$ kV/cm) can be obtained. This is a significant improvement over PMN-PT, with a coercive field of approximately 2 kV/cm. A more complete discussion on crystal growth and the PIN system can be found in this reference.

1.3.6.6 Limitations

The initial challenge in design of PMN-PT and PIN-PMN-PT transducers is the necessary DC bias voltage due to their low coercive field (E_c = 2-5.5 kV/cm for PMN-PT and PIN-PMN-PT vs. 15 kV/cm for PZT-8 [50]). This only complicates the transducer design slightly, but there can be a large impact on the energy storage requirements of the transducer. Still, the higher coupling (κ_{eff}) of single crystal materials over their ceramic counterparts ($\kappa_{33} > 0.9$ vs. $\kappa_{33} = 0.62$ for PZT-8 [51, 50]) offers the possibility of higher output, broader bandwidth devices. Moffett, et al. offer an overview of design of a broad bandwidth transducer and the benefits of using PMN-PT instead of PZT [52].

The same characteristics that make single-crystal attractive for broad bandwidth can also make it a poor choice for resonant transducers. The lower mechanical quality factor, Q_m, of PMN-PT can be either beneficial or detrimental depending upon the application. In resonant transducers, a high Q_m is beneficial. For this reason, study of new crystal systems is underway to optimize both Q_m, the mechanical loss, and d, the ideal measure of possible device output. Sherlock, et al. performed measurements on a number of these systems at both low (1 V) and high (0.2 kV/cm) drive level and reported dynamic strain and Q_m [53].

Similar to PZT and other ferroelectrics, single-crystal materials have a thermal limit. In the case of PMN-PT and PIN-PMN-PT, it is T_{R-T}. This is the temperature where there is a transition in crystal phase from rhombohedral to tetragonal. At this temperature, there is a drop in piezoelectric activity seen in both PMN-PT (T_{R-T}= 60-95^{o}C) and PIN-PMN-PT ($T_{R-T} \approx$ 125^{o}C) [49]. Zhang followed his work on PIN-PMN-PT with an investigation of these temperature effects in 2009, finding an additional intermediate pseudorhombohedral-orthorhombic and orthorhombic-tetragonal phase transition in [011] poled material from 116-129^{o}C [51]. Obviously more work must be done to determine the impact of these phase changes in high-drive condi-

[20] $x Pb(Mg_{1/3}Nb_{2/3})O_3$-$y Pb(In_{1/2}Nb_{1/2})O_3$-$(1-x-y)PbTiO_3$

tions.

The reason these temperature limits are so important is that the material self-heats under drive. The extent of self-heating is a function of both drive level and Q_m. A higher value of Q_m means that the transducer is more resonant (i.e. less lossy). This is why PZT 8 ($T_c \approx 325^o$C, $Q_m > 800$) can be driven harder than PZT 5 ($T_c \approx 350^o$C, $Q_m \approx 500$ [36]), despite the fact that it has a lower Curie temperature. Sherlock investigated the effect of loss on self-heating in the work referenced above [53]. By modifying PMN-PT to make it a lower loss system, the self heating was shown to be reduced.

Working at NUWC[21], Amin and others studied the stress dependence of these phase transitions [54]. The complicated electromechanical coupling of ferroelectric materials leads to a stress dependance of phase transitions, similar to their temperature dependence. Amin found that use of a DC bias could counteract these effects, allowing for an increased linear range of operation (Fig. 1.12). Of note in this work is the fact that the Young's modulus of both PZN-PT and PMN-PT double when they go from rhombohedral to tetragonal[22]. This could cause a significant shift in the resonance frequency of a transducer if the device were operated above its T_{R-T}.

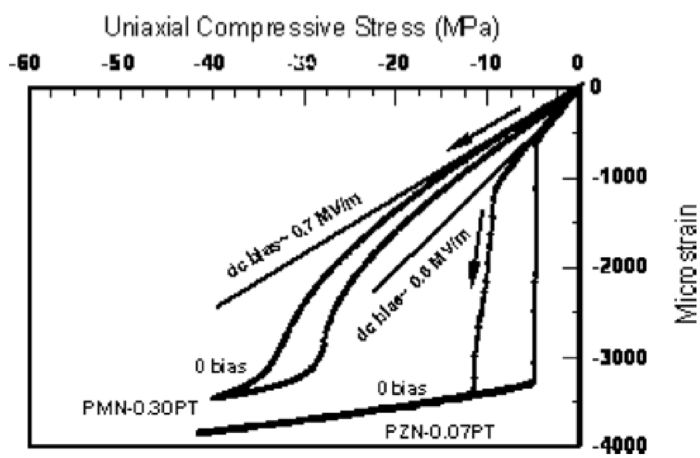

Figure 1.12. A demonstration of the effect of DC bias in stabilizing the phase transitions of PMN-PT and PZN-PT. Phase changes when no bias is applied can be seen in the sharp change of slope in the stress strain curves. Reproduced from [54].

[21] The Naval Underwater Warfare Center in Newport, RI.

[22] The intermediate phase that Zhang calls pseudorhombohedral is identified as monoclinic by Amin

1.4 Cymbal transducers

1.4.1 History

1.4.1.1 Flextensional transducers

The history of flextensional transducers traces back to the Anacostia Naval Research Laboratories where Harvey Hayes was researching methods of ship signaling in fog [55]. While Hayes patented his designs, and developed designs that became benchmarks for flextensional transducers, it seems that he never realized the potential underwater applications. This is interesting to note, as Hayes explicitly discusses the differences in impedance between air and water in his patent. It can only be assumed that in his drive towards a novel way to amplify displacement of high impedance magnetostrictive materials for impedance match with air, he rode straight past the intermediate step of water. This is what led to the eventual credit for the discovery of flextensional transducers being given to William J. Toulis.

Hayes initial designs were based on the idea of using a relatively flexible shell around a magnetostrictive drive section (Fig. 1.13). With the proper design, the shell could amplify the high impedance low displacement motion of the drive to a moderate impedance and displacement. This would allow for better impedance matching with the acoustic medium, and therefore better energy transfer.

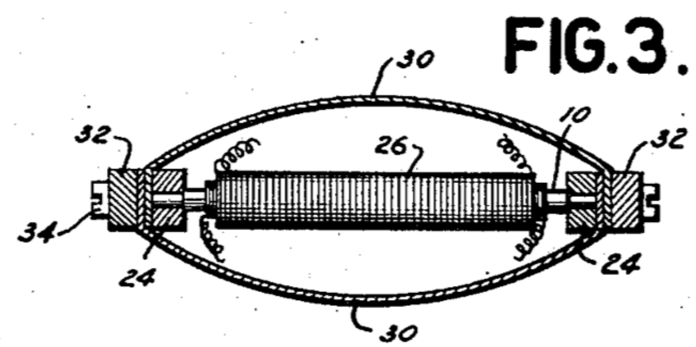

Figure 1.13. Flextensional shells around a magnetostrictive drive section. Reproduced from U.S. patent # 2,064,911 [56].

The name flextensional comes from the transformation of flexural motion from extensional motion, and vice versa. This type of displacement transformation led to a number of novel designs using a variety of drives and shell geometries. For a more thorough treatment of the designs not included in this thesis, the reader is referred to Sherman & Butler [14] and Rolt [55].

1.4.1.2 The moonie

The antecedent to the cymbal was a device designed to solve the problem of competing d_{31} and d_{33} coefficients in the active material. In 1990, Newnham, et al. designed a "transformed stress direction acoustic transducer" which operated under the principle that axial stress could be transformed to radial stress through end caps on a PZT disk [57]. The key to this design was two cavities machined into the end caps that resembled crescent or half moons (Fig.1.14). This led to the name *moonie*.

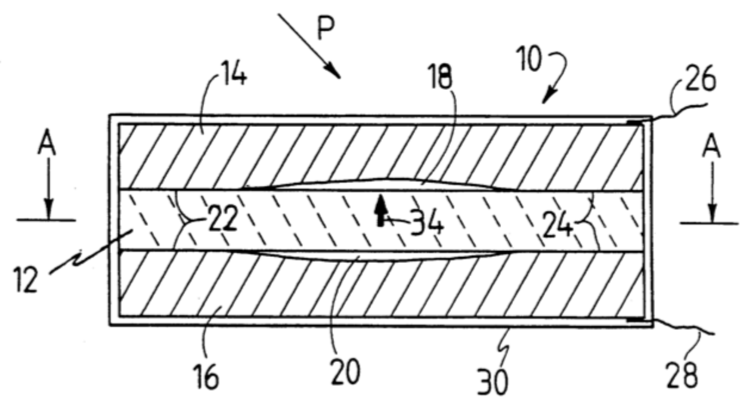

Figure 1.14. A moonie transducer. Reproduced from U.S. patent # 4,999,819 [57].

1.4.1.3 The cymbal

Shortly after the invention of the moonie, Newnham and Dogan improved their design with the *cymbal* in 1995 [2]. Its design came about as a solution to the problem of stress concentration in the moonie where the caps were bonded to the active material. FEA was performed on the moonie which showed this build-up of stress and one method of reducing it was to add a slot just above the bond joint to make the cap more compliant in this area [58]. It was noted that this increased cap displacement, but exacerbated the problem of stress concentration in the area of the groove. It was this improvement in displacement with a more compliant cap that led to the *cymbal* shaped design shown in Fig. 1.1.

The cymbal offers benefits over the moonie in addition to its increased displacement. Because the caps are made from uniform thickness material, they can be punched instead of machined. While there can be some trade-off in the accuracy of the punching process[23], the economy of punching is obvious. Also, the displacement profile of the cymbal is essentially uniform across its top rim, which is beneficial in precision actuator applications.

[23]Punching can achieve fine tolerances, but must properly account for spring back in the material. Machining offers both precision and accuracy.

1.4.2 Cymbal Advances

1.4.2.1 The double dipper

One of the cymbal's weaknesses is its susceptibility to permanent deformation under high hydrostatic pressure. In 1999 Newnham and Zhang developed a novel inverted cymbal cap design that significantly improved performance under high pressure [59]. The improved performance reported in their patent can be seen in Fig. 1.15. This configuration is often referred to as the *double dipper* due to the two areas where the cap dips back in towards the center of the transducer (Fig. 1.16). This is accomplished by using a ring of active material instead of the full disk used in the standard cymbal.

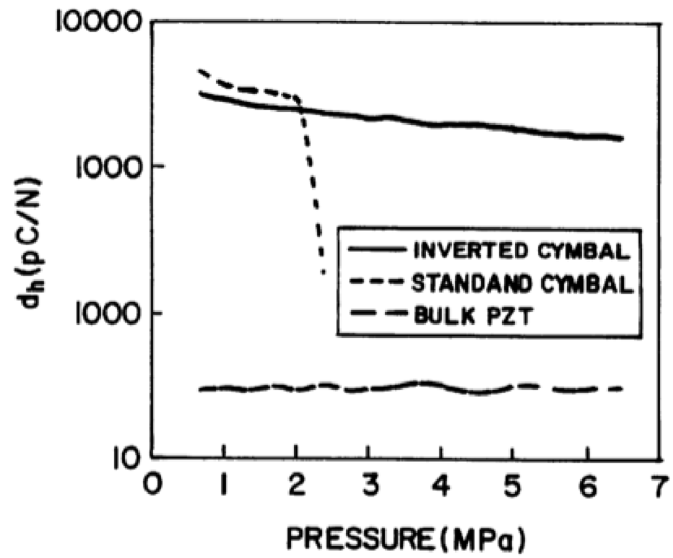

Figure 1.15. d_h vs. hydrostatic pressure for standard and inverted cymbals. Reproduced from U.S. patent # 6,232,702 [59].

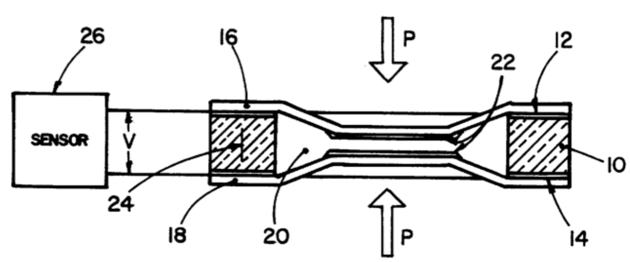

Figure 1.16. A double dipper cymbal transducer shown operating as a hydrophone. Reporduced from U.S. patent # 6,232,702.

1.4.2.2 The double driver

The double driver makes use of standard cymbal caps and two disks of active material. It was developed by Zhang and his colleagues at Penn State in 2000 [60]. The two disks are epoxied to each other with polarization vectors through the thickness pointing at each other. By driving in this manner the transducer achieves asymmetric directionality through operating in both flexural and bending modes simultaneously. When these modes of operation are properly tuned, a cardioid[24] polar pattern can be achieved.

1.4.2.3 Cap materials

During the earliest cymbal studies, the effects of the end cap material were known to be fairly dramatic. The stiffness of the cap had obvious effects on the resonance frequency, but also the spacing between the (0,1) and (0,2) modes of the cymbal. This spacing affects the usable frequency range of the transducer in either projector or hydrophone applications. A thorough study of candidate materials using finite element analysis (FEA) was performed by Dogan in 2003 [61]. The candidate materials were brass, tungsten, steel, titanium and molybdenum. The study showed that the highest coupling, tied to bandwidth, could be achieved using titanium caps.

Active materials have also been studied for use in cymbal caps. By using materials where the stiffness can be controlled (e.g. phase transformations in Nitrile or magnetostriction in Metglas^{TM}) it has been shown that the resonance frequency of cymbals can be tuned, and deformation due to pressure can be corrected [62].

1.4.2.4 Slotting caps

Just as the design of the moonie was improved to the cymbal by relief of stress, it was shown that the cymbal could be further improved by stress relief. In 2004 Ke, et al, used FEA models to study the build-up of tangential stress in traditional cymbal caps [63]. It was found that by slotting the cap radially tangential stress could be relieved (Fig. 1.17). This resulted in increased displacement and comparable generative force when compared to the traditional cymbal cap. The increased displacement is beneficial in actuator applications, and has implications to improved efficiency and output in projectors.

In 2008, a variation on this design called the *wagon wheel* flextensional transducer was introduced by Narayanan and Schwartz [64]. Similar to the slotted cymbal, the goal was to reduce the tangential stress during actuation. Experimental results showed increased displacement of approximately 35% for the new cap design. In addition, it was found that as the applied force was increased, displacement also increased. Though counterintuitive, Narayanan attributes this to increase in lateral stress in the device which allows for increased domain wall motion.

[24] The cardioid polar pattern gets its name from the heart shape it traces on a polar plot of sensitivity vs. angle.

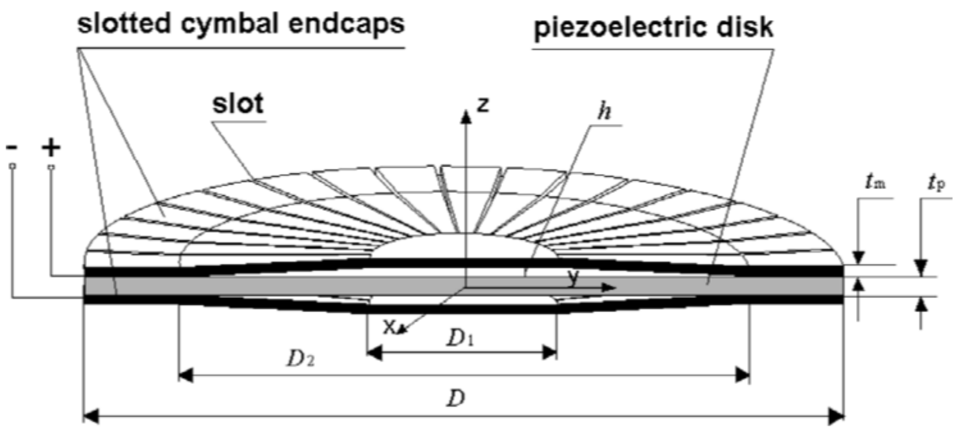

Figure 1.17. Cross section of a slotted cymbal developed by Ke, et al. Reproduced from [63]

1.4.2.5 Oriented active material

One of the primary benefits of thickness mode transducers is that they take advantage of the relatively high d coefficient along the polarization dimension (d_{33}). This is true for both traditional piezoelectric ceramics, and [001] poled single-crystal ferroelectrics mentioned before. In 2007 Luo, et al, at the Shanghai Institute of ceramics developed an open-ended rectangular cymbal cap for use with a rectangular slab of active material poled along its length [65]. By arranging the cap and active material in this way, the cymbal was amplifying the larger d_{33} coefficient of [001] poled material, rather than the traditional amplification of d_{31}.

In addition, Luo had earlier reported that in [110] poled PMNT the d_{31} coefficient is actually superior to d_{33} [66]. The same rectangular cymbal caps were then used to amplify this large d_{31} with good results. The [110] material showed improved displacement and effective coupling. This is the same implementation as using the d_{32} of [011] poled material, with a simple change of coordinate convention.

1.4.3 Cymbal Applications

1.4.3.1 Actuation

The use of cymbals as actuators traces back to one of the obvious applications of the active materials themselves. Because the converse piezoelectric effect causes a displacement of the active material, an obvious application for piezoelectric devices was use as actuators. The fact that this displacement was quite small compared to the size of the active material ($< 1\%$ strain) limited their utility, but they still found use as micro-positioners.

Just as the moonie offered increased displacement for a given strain over the bulk active material, the cymbal further improved displacement amplification. In addition, cymbals, just like moonies, could be stacked in series to further increase displacement (Fig. 1.18)

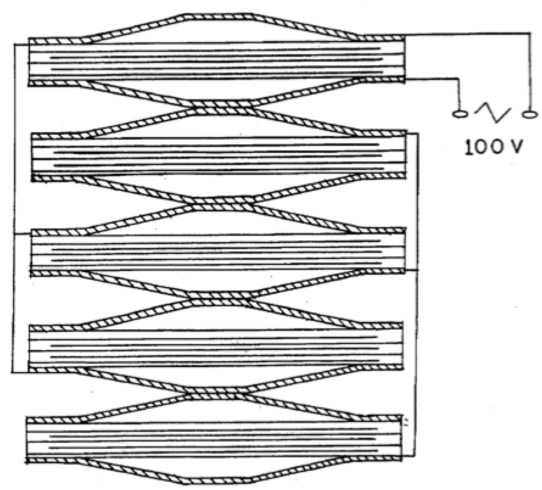

Figure 1.18. A stack of cymbal transducers in series. The wiring is parallel. Reproduced from U.S. patent #5,729,077 [2]

1.4.3.2 Medical ultrasonics

Recently cymbal arrays have been of interest in ultrasound mediated transdermal drug delivery. It has been shown that using a low intensity beam of low frequency ultrasound (20-40kHz) aides in the process of sonophoresis[25] [67, 68]. Cymbal arrays are excellent candidates for this treatment, as they can be efficient, light, and low-profile in the desired frequency band. These traits would allow for mobile treatment options that would provide a less invasive and less painful treatment for diseases such as diabetes. For a more thorough review of the biology of transdermal drug delivery, the reader is referred to Smith [69].

1.4.3.3 Energy harvesting

The efficiency with which cymbal transducers take advantage of piezoelectric activity has made them candidates for energy harvesting applications. The figure of merit (FOM) for energy harvesting is the product of the piezoelectric field constant, d, and the piezoelectric voltage constant, g. In 2004, Kim, et al. at Penn State showed that cymbals provide a good $g \cdot d$ product [70]. With PZT as the active material, they achieved power generation of 60 mW/cm^3 with a driving force of 7.8 N at 100 Hz.

Most recently, work done by Ren, et al. with single crystal PMN-PT cymbals shows that energy density of up to 188 mW/cm^3 can be achieved [71]. This three-fold increase in energy generation density was achieved through the higher piezoelectric activity of the single crystal and a rectangular cymbal cap design.

[25] sonophoresis is the process of transdermal delivery of semi-solids through the dermis via ultrasound

1.4.3.4 Low-profile projector arrays

Individual cymbal elements have a fairly high Q-factor (Q≈15) in water [62]. In the case of resonant transducers, like those used in energy harvesting and medical ultrasonics, this can be a desirable quality, however broad bandwidth is often required of underwater projectors. In order to reduce the Q, and increase output, cymbals can be fabricated into arrays. By placing the cymbals close together and potting them in a material such as polyurethane, the radiation resistance of the projector is increased. The result is a much broader bandwidth device, as can be seen in Fig. 1.19. Additionally, cymbal arrays have been made by sandwiching the individual elements between two stiff and light-weight cover plates. This method also increases radiation loading and reduces the overall resonance frequency. It will be discussed further in Chapter 3, where it has been adapted for this work.

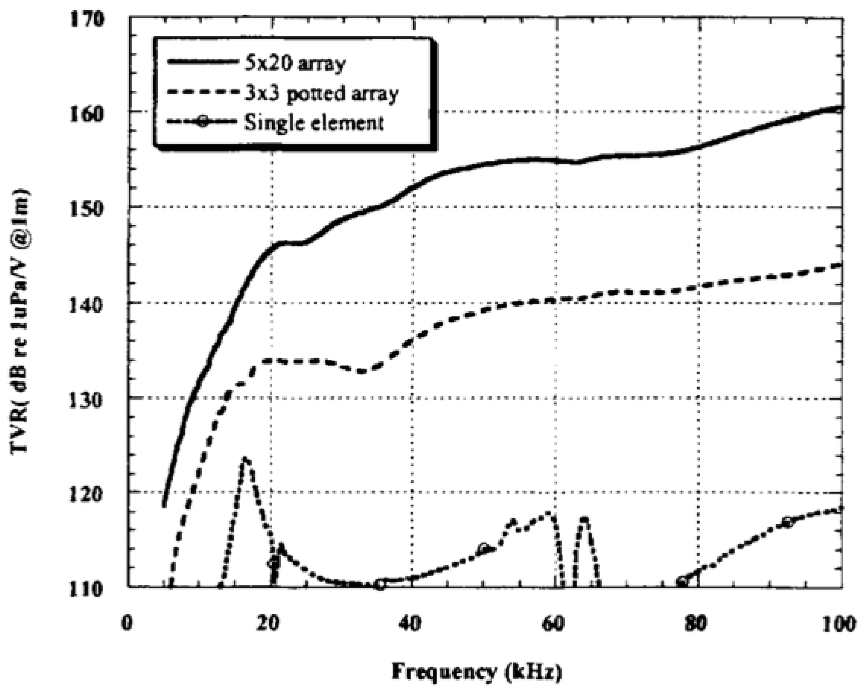

Figure 1.19. TVR of cymbal transducer arrays. From [62].

1.4.4 Cymbal competition in low-profile projectors

As the motivation for this work is to develop an improved low-profile low-frequency projector, several other low-frequency projector solutions must be considered.

1.4.4.1 Unimorphs

Unimorph actuators are created by bonding a piezoelectric material to an inactive material, usually a metal sheet. When an electric field is applied, the piezoelectric begins to deform. The difference in material properties between the two materials causes a non-uniform flexure of the device, amplifying the transverse displacement of the piezoelectric material.

RAINBOW[26] transducers are a type of unimorph created by reducing PZT against a carbon block at elevated temperature. By removing the oxygen from PZT, a non-piezoelectric layer of lead is left in its place. This creates a difference in thermal expansion coefficients between the two materials as well, and when cooled the device takes on the shape of a rainbow. Deflection can then be achieved about this deformed state through an applied field. THUNDER[27] transducers make use of a similar mismatch in coefficient of thermal expansion, but the metal layer is provided rather than reduced from the PZT (Fig. 1.20).

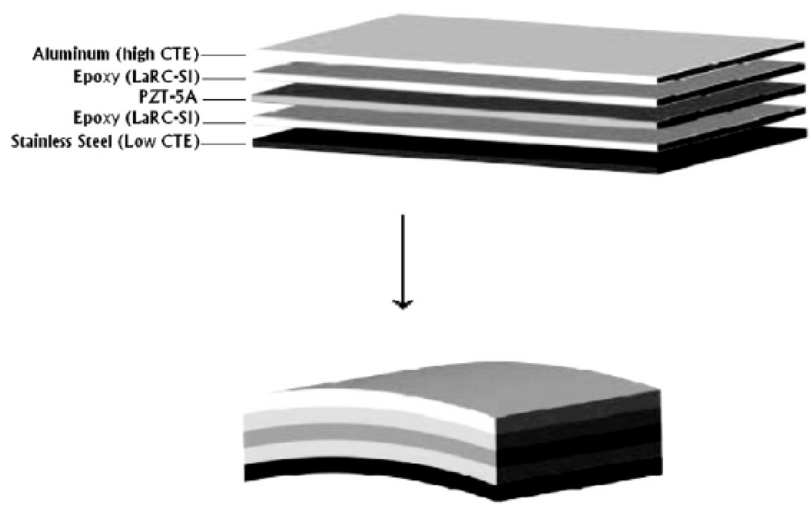

Figure 1.20. Schematic of a THUNDER transducer. From [72].

In 1997, Wise studied the optimal ceramic to metal thickness ratio for RAINBOW and THUNDER displacement actuators [73]. She found a fairly broad peak for RAINBOW transducers centered around 30% reduction, and a weaker relationship for THUNDER with a maximum anywhere from 15-35% aluminum depending upon the applied field. For both types, displacements of greater than 150 microns were obtained for 2.54 cm diameter disks driven at 1.5 kV/mm.

The large displacement characteristics of RAINBOW and THUNDER actuators make them appealing for low-profile drivers and actuators. This is tempered with the fact that the reduction in mechanical impedance from the bulk PZT is significant. Wise shows a plot of displacement vs. applied load for a PZT-5A THUNDER actuator (Fig. 1.21). Under a load of ≈ 4 N, the device has already lost $\approx 20\%$ of its displacement capability. This limits the utility of RAINBOW and

[26] Reduced (R) and (A) internally (IN) biased (B) oxide (O) wafer (W)
[27] Thin (TH) layer unimorph (UN) driver (DER) and sensor

THUNDER transducers in underwater applications where water-loading and hydrostatic pressure are unavoidable.

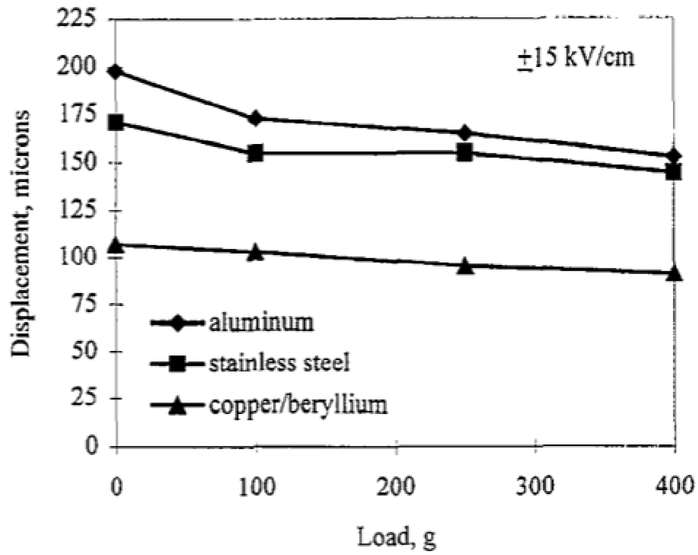

Fig. 4. Effect of the metal employed on the average displacement properties of PZT-5H THUNDER devices operated at ± 15 kV cm^{-1} under loads up to 400 g.

Figure 1.21. Displacement vs. applied load for a THUNDER transducer. From [73].

1.4.4.2 BB Transducer Arrays

Utilizing a novel method of creating microspheres of slurry material [74], hollow spheres of PZT may be made. Once hardened, they can be electroded and poled radially to operate in a breathing mode. Arrays of these miniature transducers can then be constructed to create a low-profile projector (Fig. 1.22). Fig. 1.23 shows the TVR vs. frequency for a 4x4 (16 element) array of 100μm wall thickness spheres of different radius. While the frequency range is impressive, the higher output portion of the curve is in the mid to high-frequency ultrasonic band. Comparing to Fig. 1.19, it can be seen that cymbals offer a better solution at lower frequencies.

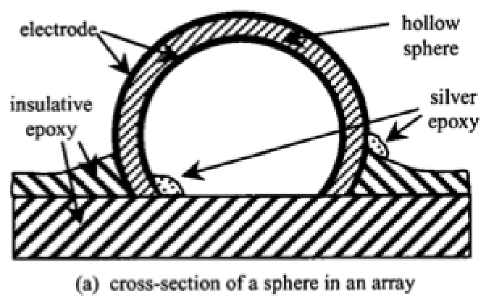

Figure 1.22. A BB transducer mounted to an array. From [75].

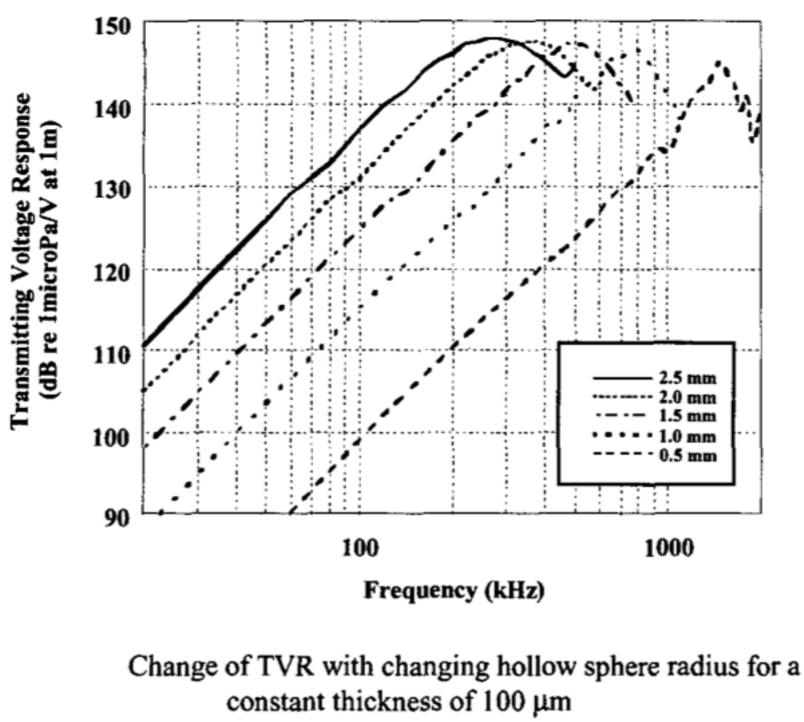

Figure 1.23. TVR of BB transducer arrays.. From [75].

1.4.5 Cymbal Limitations

1.4.5.1 Dimensional tolerances

Cymbal transducers are theoretically simple to fabricate, and punched caps allow the price to be reduced to the order of $5 per device. At first glance, this leads them to be the obvious choice over other low-profile piezo-transducers such as RAINBOW, THUNDER, and the moonie. However, their sensitivity to dimensional changes can lead to mode splitting and spurious resonances. Meyer, et al. used FEA models of cymbals to determine the nature of spurious resonances and how to improve low production yields ($\approx 20\%$) [76]. They found that the resonance frequency of cymbals is very sensitive to cavity depth, and to a lesser extent, epoxy layer thickness. With variation from one cap side to the other, asymmetric modes result due to a coupling with a flexural mode of the active material that would otherwise not be excited. This can decrease output and induce unwanted stress.

1.4.5.2 Temperature concerns

Another epoxy concern is the curing temperature. The joint between the caps and the active material sees some of the highest stresses in the device, and therefore needs to be as strong as possible. Epoxies with high cure temperatures cannot be used due to the Curie temperature of the material. Tressler reports a further complication when single-crystal is used, as the T_{R-T} becomes the curing limit due to the differences in stiffness and coefficient of thermal expansion that will induce high stress in the crystal and could produce cracking [77]. He gives a thorough description of the crystal properties through the bonding process, as well as the strength tests performed after curing. Of note is the fact that Tressler uses an electrically conductive adhesive film to bond his caps, which fixes the problem of epoxy thickness variation.

1.4.5.3 Electrical connectivity

Electrically conductive epoxies are desirable, so that electrical leads can be attached to the caps instead of the active material. But even with a conductive epoxy, electrical connection concerns exist. The temperature at which soldering is done must not exceed the temperature of the epoxy. Also, depending on the choice of cap material, soldering may not be robust. Meyer discusses these issues as well [76].

Chapter 2

Theory

The necessary theory for solution of the problem statement from the first chapter is laid out below. Development of the equations of piezoelectricity follows Sherman & Butler [14], with an explanation of stress and strain convention following Wilson [37]. Finite element analysis was carried out using ATILA, and the relevant theory below is adapted from a more complete treatment in the user guide [78]. Several fundamental concepts of acoustic sources are treated, and more complete explanations can be found in Pierce [79], Sherman & Butler, and Kinsler, Frey, Coppens, and Sanders [80]. Finally, analytical treatment of cymbal transducers will be discussed.

2.1 Piezoelectricity

2.1.1 T & S

Stress (T), is the force per unit area on a body. Elastic solids can support both axial (e.g. pulling on a beam along it's length) and shear stress (e.g. pushing or pulling on a beam in a direction perpendicular to its length). The basis vectors for our stress notation can be seen in Fig. 2.1. They are labeled 1, 2, and 3 instead of the common x, y, and z in order to stay consistent with the notation of piezoelectric theory that will be discussed later.

Tensor or vector notation can be used to report stress. In tensor notation, two subscripts follow the variable. The first is the face on which the force is applied, and the second is the direction in which the force is applied. If both subscripts are positive, or if both are negative, the stress is considered to be positive (e.g. T_{11} and T_{-1-1} are positive stresses). Faces are given the same label as their normal vector (Fig. 2.1). For axial stresses, the direction of the force and face to which it is applied have the same ordinal (e.g. T_{22}). For shear stresses the direction of the force is orthogonal to the normal vector of the face to which it is applied.

Tensor notation results in some redundancy (e.g. $T_{12} = T_{21}$), so a vector notation has been developed to simplify this. First, axial stresses are reported with just one subscript instead of

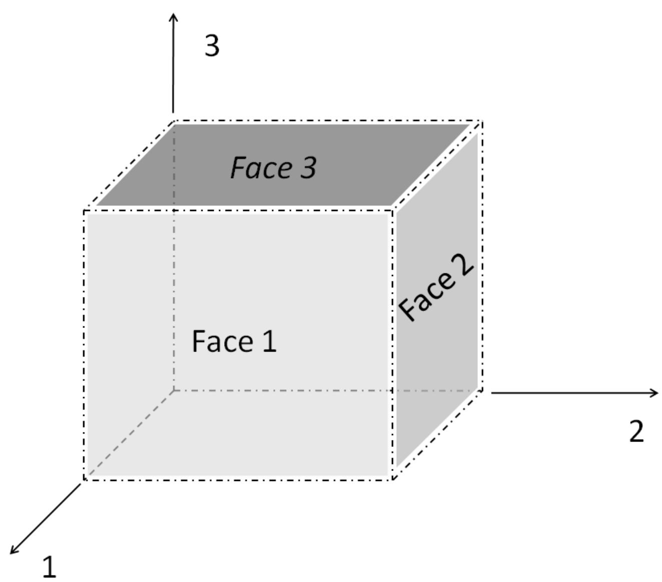

Figure 2.1. Faces of an elastic solid.

two (e.g. T_2 instead of T_{22}). Second, shear stresses produce change of shape that can be modeled as an apparent rotation of four faces about one of the basis axes. The ordinals 4, 5, and 6 are used to denote this apparent rotation about the 1, 2, and 3 axes respectively. In Fig. 2.2 the stress T_4 and the rotation about the 1-axis can be seen. The figures following (Fig. 2.3-2.5), show the relationship between the tensor and vector notation for T_4, T_5, and T_6. The convention used follows the development of Wilson [37], where $T_4 = 2T_{23} = 2T_{32}$.

Axial strains (S_1,S_2, and S_3) are the change in length of a solid over its original length. Axial strain is most often reported as a percentage, but will also be seen reported in parts per million (ppm). In the notation above, S_2 would denote a positive strain in the same direction as the 2-axis. An example of this is seen in Fig. 2.6. Deformation in the direction of the axial stress occurs, and transverse deformation to a lesser extent can occur as well. This phenomena is known as the *Poisson effect*, and the ratio of transverse deformation to axial deformation is known as *Poisson's ratio* (ν) in isotropic[1] solids. A straightforward derivation shows that unless *Poisson's ratio* is equal to 0.5, there is a change in volume of the material when it undergoes axial strain.

Shear strains (S_4,S_5, and S_6) are a measure of the change of shape of a solid about its axes. They are reported in radians. An example of shear deformation can be seen in Fig. 2.2, where a shear strain $S_4 = \gamma$ is developed as a result of shear stress T_4. For the materials relevant to this thesis, there is no coupling effect in shear strain (i.e. T_4 can only induce S_4, and not S_5 or S_6), unlike axial strain. Also unlike axial strain, shear strain only produces a change in shape of the solid and not a change in volume.

In piezoelectric materials, strain can be induced through stress or by piezoelectric coupling

[1]A material is isotropic if its properties are the same in all directions

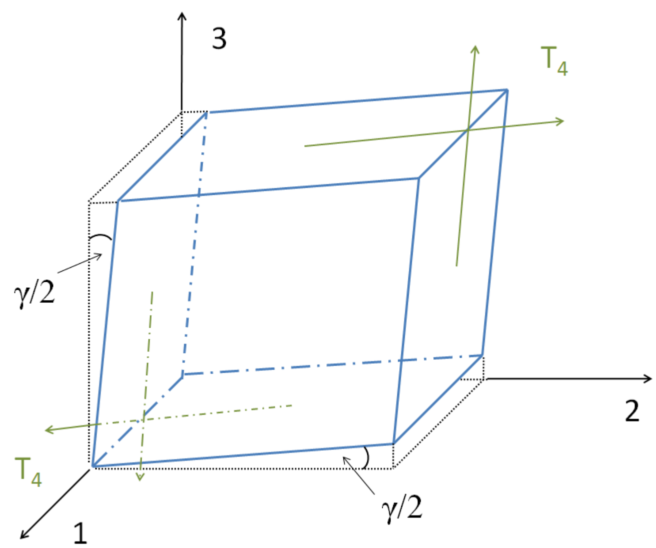

Figure 2.2. Deformation $S_4 = \gamma$ resulting from a shear stress T_4

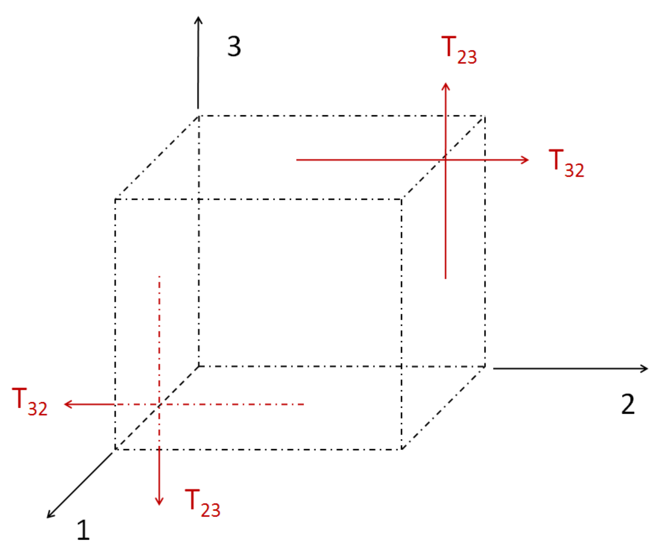

Figure 2.3. $T_4 = 2T_{23} = 2T_{32}$

with an electric field. It is for this reason that care must be taken when measuring material properties, such that the effects of this coupling do not influence the values measured.

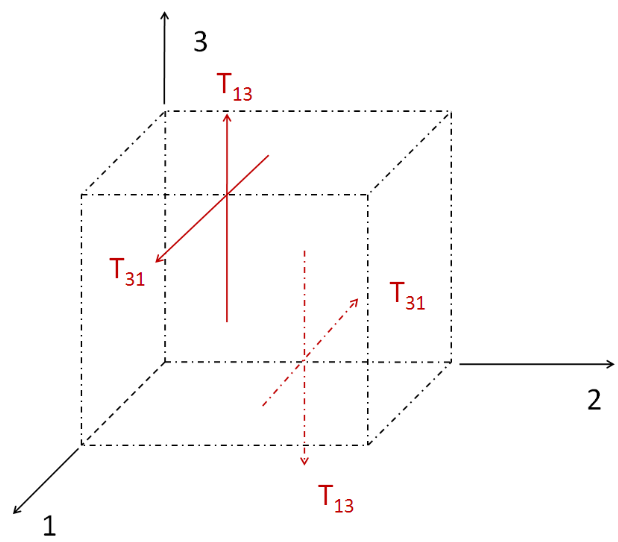

Figure 2.4. $T_5 = 2T_{31} = 2T_{13}$

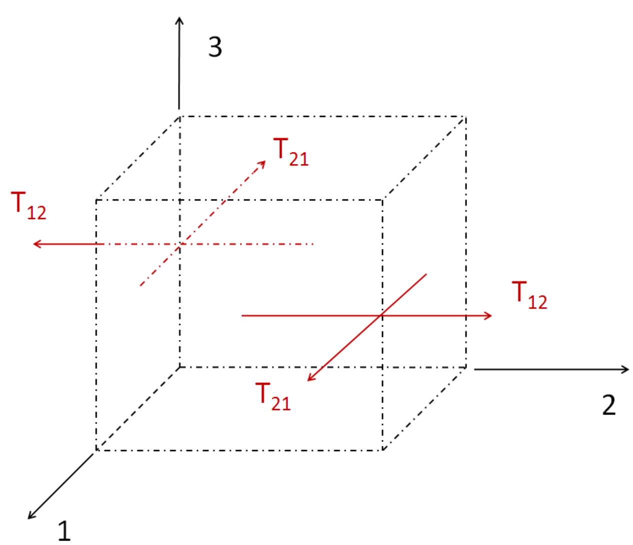

Figure 2.5. $T_6 = 2T_{12} = 2T_{21}$

2.1.2 E & D

Electric field (E) is the measure of an electric potential difference between two surfaces. It is reported in volts per unit length. In a piezoelectric transducer there are electroded surfaces for application of the signal. The voltage applied across these electrodes divided by the distance between them will give the electric field. The direction of the field is given in the same notation as applied stress. A field cannot be applied perpendicular to the face of the electrode, so only the

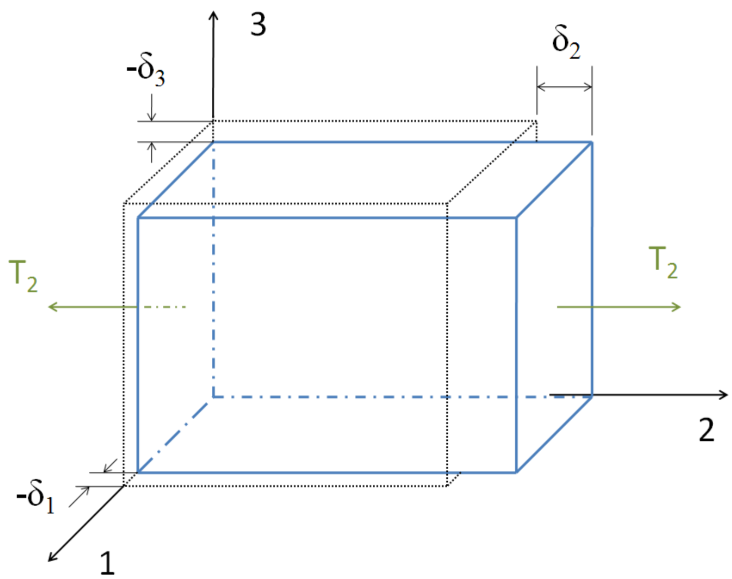

Figure 2.6. Deformations $S_1 = \delta_1, S_2 = \delta_2, S_3 = \delta_3$ resulting from an axial stress T_2

three basis directions are allowed (E_1, E_2 and E_3). The poling direction for the active material is defined to be the 3 direction for piezoelectric materials.

Electric displacement is a measure of charge per unit area. When a voltage is applied across the electrodes of a transducer, a charge will develop. The amount is dependent upon the permittivity of the material between the electrodes, as well as the coupled piezoelectric effect of stress. Similar to electric field, electric displacement is only reported in the basis directions (D_1, D_2 and D_3), because it is a report of charge per unit area on the basis faces (e.g. D_1 is a measure of charge per unit area on the 1 and -1 faces).

2.1.3 The equations of piezoelectricity

The phenomenological theory of piezoelectric ceramics combines dynamic structural mechanics with transduction factors that allow for the influence of linear active material effects (i.e. piezoelectricity). The constituent equations linearly relate stress (T), strain (S), electric field (E), and electric displacement (D) in the following way:

$$\begin{aligned} [S] &= [s^E][T] + [d]^t[E] \\ [D] &= [d][T] + [\epsilon^T][E] \end{aligned} \tag{2.1}$$

In this notation, superscripts indicate which independent variable is held constant[2] during measurement (e.g. $[s^E]$ is the elastic compliance matrix measured with constant electric field). The exception to this is lower case t, which denotes the matrix transpose operator.

The elastic compliance is a measure of how much the material will deform under load and is usually reported in $\left[\frac{m^2}{N}\right]$. The other material properties in Eq. (2.1) are the piezoelectric field coefficients, $[d]$, and the electrical permittivity matrix (measured at constant stress), $[\epsilon^T]$. Looking at the equations, it can be seen that the piezoelectric field coefficients give the strain per unit electric field or electric displacement per unit stress ($\left[\frac{unitless}{V/m}\right] = \left[\frac{m}{V}\right] = \left[\frac{C}{N}\right] = \left[\frac{C/m^2}{N/m^2}\right]$), and the permittivity gives the charge per unit area per unit electric field ($\left[\frac{q/m^2}{V/m}\right] = \left[\frac{F}{m}\right]$]). These quantities are generally reported in $\left[\frac{pC}{N}\right]$ and relative permittivity, $K_{mn} = \left[\frac{\epsilon_{mn}}{\epsilon_0}\right]$, where $\epsilon_0 = 8.85 \times 10^{-12} \frac{F}{m}$ is the permittivity of free space, and m and n are matrix indices.

$[S]$ is a 6×1 matrix and $[D]$ a 3×1 matrix. Both equations can be combined as follows:

$$\begin{bmatrix} S_1 \\ S_2 \\ S_3 \\ S_4 \\ S_5 \\ S_6 \\ D_1 \\ D_2 \\ D_3 \end{bmatrix} = \begin{bmatrix} s^E_{11} & s^E_{12} & s^E_{13} & s^E_{14} & s^E_{15} & s^E_{16} & d_{11} & d_{21} & d_{31} \\ s^E_{21} & s^E_{22} & s^E_{23} & s^E_{24} & s^E_{25} & s^E_{26} & d_{12} & d_{22} & d_{32} \\ s^E_{31} & s^E_{32} & s^E_{33} & s^E_{34} & s^E_{35} & s^E_{36} & d_{13} & d_{23} & d_{33} \\ s^E_{41} & s^E_{42} & s^E_{43} & s^E_{44} & s^E_{45} & s^E_{46} & d_{14} & d_{24} & d_{34} \\ s^E_{51} & s^E_{52} & s^E_{53} & s^E_{54} & s^E_{55} & s^E_{56} & d_{15} & d_{25} & d_{35} \\ s^E_{61} & s^E_{62} & s^E_{63} & s^E_{64} & s^E_{65} & s^E_{66} & d_{16} & d_{26} & d_{36} \\ d_{11} & d_{12} & d_{13} & d_{14} & d_{15} & d_{16} & \epsilon^T_{11} & \epsilon^T_{12} & \epsilon^T_{13} \\ d_{21} & d_{22} & d_{23} & d_{24} & d_{25} & d_{26} & \epsilon^T_{21} & \epsilon^T_{22} & \epsilon^T_{23} \\ d_{31} & d_{32} & d_{33} & d_{34} & d_{35} & d_{36} & \epsilon^T_{31} & \epsilon^T_{32} & \epsilon^T_{33} \end{bmatrix} \begin{bmatrix} T_1 \\ T_2 \\ T_3 \\ T_4 \\ T_5 \\ T_6 \\ E_1 \\ E_2 \\ E_3 \end{bmatrix} \tag{2.2}$$

The above formulation, Eq. (2.2), seems daunting at first, but due to crystal symmetry and notational redundancy (i.e. $d_{31} = d_{13}$), it can be simplified quite a bit. As an example, the full matrix for [011] poled PMN-29PT [1], assuming $4mm$ symmetry, is shown below:

$$\begin{bmatrix} S_1 \\ S_2 \\ S_3 \\ S_4 \\ S_5 \\ S_6 \\ D_1 \\ D_2 \\ D_3 \end{bmatrix} = \begin{bmatrix} s^E_{11} & s^E_{12} & s^E_{13} & & & & & & d_{31} \\ s^E_{12} & s^E_{22} & s^E_{23} & & & & & & d_{32} \\ s^E_{13} & s^E_{23} & s^E_{33} & & & & d_{31} & d_{32} & d_{33} \\ & & & s^E_{44} & & & & d_{24} & \\ & & & & s^E_{55} & & d_{15} & & \\ & & & & & s^E_{66} & & & \\ & & d_{31} & & d_{15} & & \epsilon^T_{11} & & \\ & & d_{32} & d_{24} & & & & \epsilon^T_{22} & \\ d_{31} & d_{32} & d_{33} & & & & & & \epsilon^T_{33} \end{bmatrix} \begin{bmatrix} T_1 \\ T_2 \\ T_3 \\ T_4 \\ T_5 \\ T_6 \\ E_1 \\ E_2 \\ E_3 \end{bmatrix} \tag{2.3}$$

[2]Usually, this superscript denotes the variable is equal to zero during measurement, but Sherman and Butler make the distinction that it simply be held constant, as the value can be derived from the partial derivative of the two variables being studied [14].

Eq. (2.3) shows only unique terms by eliminating redundancy. Also, terms equal to zero are shown as blank spaces for visual simplicity. It can be seen the the coefficient matrix is symmetric about the main diagonal. To better understand the subscript notation, let us consider one row:

$$S_2 = s_{12}^E T_1 + s_{22}^E T_2 + s_{23}^E T_3 + d_{32} E_3 \tag{2.4}$$

In Eq. (2.4), s_{12}^E couples S_2 and T_1, s_{23}^E couples S_2 and T_3, and d_{32} couples S_2 and E_3. No clear relationship can be drawn for which subscript denotes the independent variables (stress and electric field), and which denotes the dependent variable (strain). The first reason for this is the transposition of $[d]$, which inverts its subscripts. The second reason for this lack of relationship is that if two or more terms are equal (e.g. $s_{12}^E = s_{21}^E$), only one is used in the matrix. This confusion is not ideal, but for practical purposes the subscripts tell the relative directions involved between the dependent and independent variables, and axial and transverse coupling relationships can still be readily seen.

In addition to the above formulation, where stress and electric field are the independent variables, there are three other sets of equations:

$$\begin{aligned} [T] &= [c^E][S] - [e]^t[E] \\ [D] &= [e][S] + [\epsilon^S][E] \end{aligned} \tag{2.5}$$

$$\begin{aligned} [S] &= [s^D][T] + [g]^t[D] \\ [E] &= -[g][T] + [\beta^T][D] \end{aligned} \tag{2.6}$$

$$\begin{aligned} [T] &= [c^D][S] - [h]^t[D] \\ [E] &= -[h][S] + [\beta^S][D] \end{aligned} \tag{2.7}$$

Though these equations have different coefficient matrices, they are not unique. Their purpose is to allow for simplicity in measurement of material properties and in solution of equations where different independent variables are desired. For a more thorough discussion of Eqs. (2.5)-(2.7), the reader is referred to Sherman and Butler [14].

2.2 The acoustic model

2.2.1 ATILA

ATILA is a finite element analysis code developed at the Acoustics Laboratory of the *Institut Supérieur d'Electronique du Numérique* in Lille, France [78]. It was written for the purpose of modeling coupled fluid structure interaction for piezoelectric and magnetostrictive transducers. Multiple problem types can be solved in 1D to 3D structures: modal, static, harmonic, transient, and steady-state thermal. By taking advantage of any model symmetry, the problem can be modeled in $^1/_2$, $^1/_4$, or $^1/_8$ space or axisymmetrically to keep file sizes manageable.

2.2.1.1 General formulation and reduction

The most general treatment of magnetic, magnetostrictive, and piezoelectric structural interaction in ATILA is given as:

$$\begin{bmatrix} [K_{uu}]-\omega^2[M] & [K_{u\Phi}] & [K_{u\phi}] & [K_{uI}] & -[L] \\ [K_{u\Phi}]^T & [K_{\Phi\Phi}] & [0] & [0] & [0] \\ [K_{u\phi}]^T & [0] & [K_{\phi\phi}] & [K_{\phi I}] & [0] \\ [K_{uI}]^T & [0] & [K_{\phi I}]^T & [K_{II}] & [0] \\ -\rho^2c^2\omega^2[L]^T & [0] & [0] & [0] & [H]-\omega^2[M_1] \end{bmatrix} \begin{bmatrix} \underline{U} \\ \underline{\Phi} \\ \underline{\phi} \\ \underline{I} \\ \underline{P} \end{bmatrix} = \begin{bmatrix} \underline{F} \\ -\underline{q} \\ -\underline{f} \\ -\underline{f_b} \\ \rho^2c^2\underline{\Psi} \end{bmatrix} \tag{2.8}$$

Before explaining this formula term by term, let us first recognize that for piezoelectric problems the magnetic potential, $\underline{\phi}$, and the current for magnetic coils, $\underline{I}$, will be equal to zero. As such, we can remove the terms that couple them to the problem, and get the following simplification:

$$\begin{bmatrix} [K_{uu}]-\omega^2[M] & [K_{u\Phi}] & -[L] \\ [K_{u\Phi}]^T & [K_{\Phi\Phi}] & \\ [K_{u\phi}]^T & & \\ [K_{uI}]^T & & \\ -\rho^2c^2\omega^2[L]^T & & [H]-\omega^2[M_1] \end{bmatrix} \begin{bmatrix} \underline{U} \\ \underline{\Phi} \\ \underline{P} \end{bmatrix} = \begin{bmatrix} \underline{F} \\ -\underline{q} \\ -\underline{f} \\ -\underline{f_b} \\ \rho^2c^2\underline{\Psi} \end{bmatrix}$$

Furthermore, the reduced magnetic flux across the magnetic domain boundary, $\underline{f}$, and the reduced magnetic flux seen by the coils, $\underline{f_b}$, will also be equal to zero, since no magnetostrictive or magnetic materials are being used. This results in the version of the problem that is pertinent to piezoelectric transducers:

$$\begin{bmatrix} [K_{uu}]-\omega^2[M] & [K_{u\Phi}] & -[L] \\ [K_{u\Phi}]^T & [K_{\Phi\Phi}] & \\ -\rho^2c^2\omega^2[L]^T & & [H]-\omega^2[M_1] \end{bmatrix} \begin{bmatrix} \underline{U} \\ \underline{\Phi} \\ \underline{P} \end{bmatrix} = \begin{bmatrix} \underline{F} \\ -\underline{q} \\ \rho^2c^2\underline{\Psi} \end{bmatrix} \tag{2.9}$$

After carrying out the matrix multiplication, the first row is the equation of elasticity for the structure,

$$\Big([K_{uu}]-\omega^2[M]\Big)\underline{U}+[K_{u\Phi}]\underline{\Phi}-[L]\underline{P}=\underline{F}\ ,$$

where $[K_{uu}]$ is the stiffness matrix for the materials, ω is angular frequency, $[M]$ is the mass matrix, $\underline{U}$ is the displacement vector for the nodes, $[K_{u\Phi}]$ is the piezoelectric matrix, $\underline{\Phi}$ contains the nodal electric potentials, $[L]$ is the fluid-structure coupling matrix, $\underline{P}$ contains the nodal pressure values, and $\underline{F}$ contains the nodal forces. This gives a force balance at each node by summing the effects of an element's stiffness, acceleration, piezoelectric coupling, the pressure it is subject to by the fluid, and any applied forces. In ATILA, the convention is to denote a vector with an underline.

The second row of Eq. (2.9) is Poisson's equation for the piezoelectric material:

$$[K_{u\Phi}]^T \underline{U} + [K_{\Phi\Phi}]\underline{\Phi} = -\underline{q} \ ,$$

where $[K_{\Phi\Phi}]$ is the dielectric matrix, and $\underline{q}$ is the nodal charge. This equation enforces conservation of charge, accounting for both piezoelectric induced charge and the direct charge developed by the potential difference across the element.

The final row is Helmholtz's equation for the fluid domain:

$$-\rho^2 c^2 \omega^2 [L]^T \underline{U} + \Big([H] - \omega^2 [M_1]\Big)\underline{P} = \rho^2 c^2 \underline{\Psi} \ ,$$

where ρ is the fluid density, c is the fluid sound speed, $[H]$ is the fluid stiffness matrix, $[M_1]$ is the fluid mass matrix, and $\underline{\Psi}$ contains the nodal values of the "integrated normal derivative of the pressure on the surface boundary S" [78]. Solution of the homogeneous Helmholtz equation ($\underline{\Psi} = 0$) would allow for determination of the pressure field of the transducer. The added term $\underline{\Psi}$ is for imposing a boundary condition at the edge of the model.

The above surface S is the *radiating boundary* of the problem. By impedance matching at S,

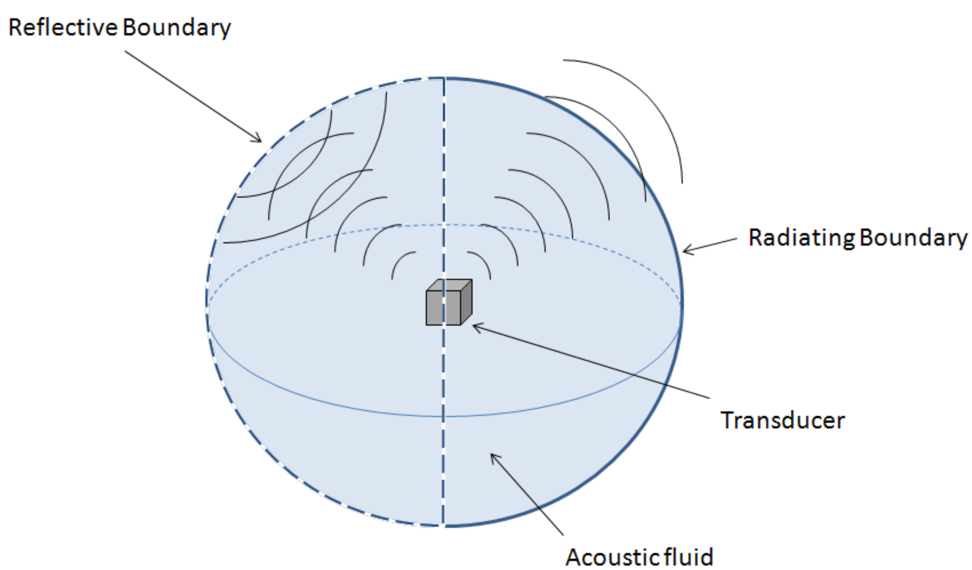

Figure 2.7. A modeled 3D domain with reflective and radiating boundaries.

the problem can be made to appear as though occurring in an infinite acoustic medium, rather than seeing reflections off of S (Fig. 2.7). In this radiating case, $\underline{\Psi}$ takes the following form[3]:

$$\underline{\Psi} = -\frac{1}{\rho c}\left(\frac{1}{r} + j\frac{\omega}{c}\right)[D]\underline{P} + \frac{1}{\rho c}\left(\frac{\frac{1}{r} - j\frac{\omega}{c}}{1 + \frac{\omega^2 r^2}{c^2}}\right)[D']\underline{P} \tag{2.10}$$

$[D]$ and $[D'$] are matrices assembled by putting damping elements on the radiating surface for the purpose of impedance[4] matching, r is the radius from the *acoustic center* of the model, and $j = \sqrt{-1}$. This equation can be better understood by looking at velocity field of a monopole (adapted from Pierce [79]):

$$\underline{v_r} = \frac{\underline{P}}{\rho c}\left(1 + \frac{j}{kr}\right)$$

In the above equation, k is the wavenumber, and v_r is the radial component of the particle velocity in the field. Using the relation $\omega = ck$ and rearranging terms gives:

$$v_r = -\frac{1}{\rho c}\left(\frac{1}{r} + j\frac{\omega}{c}\right)\frac{w}{c}\underline{P} \tag{2.11}$$

Eq. (2.11) takes a similar form to the first term of Eq. (2.10). Through a similar derivation and rearrangement, the velocity field of a dipole can be made to look like the second term of Eq. (2.10). By matching the surface velocity on S with that of the propagating wave, the surface no longer appears to be a boundary. Depending on whether the surface is in the far-field or near-field, ATILA uses monopolar or dipolar dampers to give the appearance of an infinite acoustic medium.

2.2.1.2 Harmonic analysis

The problem to be solved in this work is a harmonic analysis of a radiating piezoelectric structure. This is referred to as (HAR5) in the ATILA manual. In this analysis, the user defines excitations (displacements, rotations, pressures, electrical or magnetic potentials, temperatures, and magnetic excitation currents) or loads (forces, momentums, electric charge, current, magnetic charge, flux through magnetic coils, and voltage in the magnetic coils). With these excitations and loads, along with the radiating boundary condition, the user can apply the boundary conditions necessary for solution of the problem.

The user then selects the frequencies at which the problem will be solved. At this point, the matrices are populated and made symmetric. The general formulation matrix, Eq. (2.8), is then solved by Gaussian algorithms.

---

[3]This formulation is only accurate for a spherical surface. For a more general treatment, see the ATILA user guide [78].

[4]Impedance in this case is the ratio of pressure to particle velocity $\left(\frac{p}{v}\right)$ in the acoustic medium. This is not a true acoustic impedance, but rather *specific* acoustic impedance.

2.2.1.3 Modeling internal losses

ATILA allows for the modeling of internal losses through complex material properties. The following derivation explaining the basis for this loss model comes in part from Kinsler, et al. [80] and Maza [81].

Complex material property loss can be understood by considering the case of longitudinal vibrations in a bar. The wave speed for propagation is dependent upon the density of the material, ρ, and the Young's Modulus, Y:

$$c = \sqrt{\frac{Y}{\rho}}$$

Young's modulus is a material property that relates longitudinal stress (σ) to strain (ε) in an isotropic material in the following way:

$$\varepsilon(t) = |\varepsilon| cos\left(\omega t\right)$$

$$\sigma(t) = |Y||\varepsilon| cos\left(\omega t + \theta_Y\right)$$

Considering that stress and strain can be out of phase by an amount θ_Y, we can define the modulus to be complex to track this phase difference:

$$Y = Y' + jY''$$

$$\theta_Y = tan^{-1}\left(\frac{Y''}{Y'}\right)$$

$$\sigma(t) = Y'|\varepsilon| cos\left(\omega t\right) + jY''|\varepsilon| cos\left(\omega t\right)$$

In the above equations, $|\varepsilon|$ is the magnitude of the strain[5], Y' is the ratio of in-phase stress to strain, and Y'' is the ratio of out-of-phase stress to strain. The ratio of loss modulus (Y'') to storage modulus (Y') is called the loss factor:

$$\eta = \frac{Y''}{Y'}$$

For a propagating longitudinal wave in a bar, the general time harmonic solution can be shown to be:

$$\xi(x,t) = \left(Ae^{-jkx} + Be^{jkx}\right) e^{j\omega t}$$

[5] Magnitude of a complex number, $c = a + jb$, can be obtained by the following formula: $|c| = \sqrt{(a-jb)(a+jb)} = \sqrt{a^2+b^2}$.

In the above, ξ is the displacement, x is the direction of propagation, t is time, and A and B are amplitudes. The two complex exponentials provide orthogonal oscillatory functions to represent the wave motion.

Noting that the wave speed (c) is now complex, due to the complex modulus, it can be seen that the wave number k will also be complex due to the relationship $\omega = ck$. We can then define a complex wavenumber similar to the modulus:

$$k = k' + jk''$$

Substituting this into the general solution:

$$\xi(x,t) = \left(Ae^{-jk'x}e^{k''x} + Be^{jk'x}e^{-k''x}\right)e^{j\omega t}$$

This gives two real exponential terms, one that decays and one that is unbounded. Applying realistic boundary conditions will force that $A = 0$. Now there is a propagating wave with an exponential decay which governs the loss:

$$\xi(x,t) = Be^{jk'x}e^{-k''x}e^{j\omega t}$$

In a similar fashion to the above derivation, complex material properties for the compliance and permittivity can be implemented in ATILA. This allows for modeling of material losses.

2.3 Acoustical measures of transducers

2.3.1 The reasons for normalizing transducer response

Any figure of merit for transducer response needs to allow for normalizing the response to a standard. This allows for measurements to be made in a convenient fashion, and then scaled back to a standard for the purpose of clear A to B comparisons of competing designs. There are a number of considerations that must be made to normalize results.

2.3.1.1 The far-field ($^1/_r$)

If a transducer is sufficiently baffled[6], it can be considered to be a monopole when it is small compared to the acoustic wavelength[7] ($ka << 1$). The equation for the pressure field of a radially oscillating sphere is (adapted from Pierce [79]):

$$P(r) = \frac{-jka^2\rho c v_s}{r(1-jka)}e^{jk(r-a)} \tag{2.12}$$

[6] An ideal baffle would impose the condition that the back side of an oscillating transducer doesn't affect the pressure field on the front side. In this way, the transducer is a volume velocity source (like a monopole), instead of behaving as a force source (like a dipole)

[7] ka gives a dimensionless comparison of the transducer size to the frequency of the acoustic wave, where a is the practical radius and $k = \frac{2\pi}{\lambda}$.

In Eq. (2.12) v_s is the surface velocity of the radially oscillating sphere, and a is the radius of the sphere. When $r >> a$, the source is considered to be a monopole and this simplifies to:

$$P(r) = \frac{-jka^2 \rho c v_s}{r} e^{jk(r)}$$

The amplitude of the pressure falls off as $^1/_r$. If the pressure is measured at two different points, r_0 and r_m (Fig. 2.8), both much greater than a, then the following equality is true:

$$P_0 r_0 = P_m r_m \tag{2.13}$$

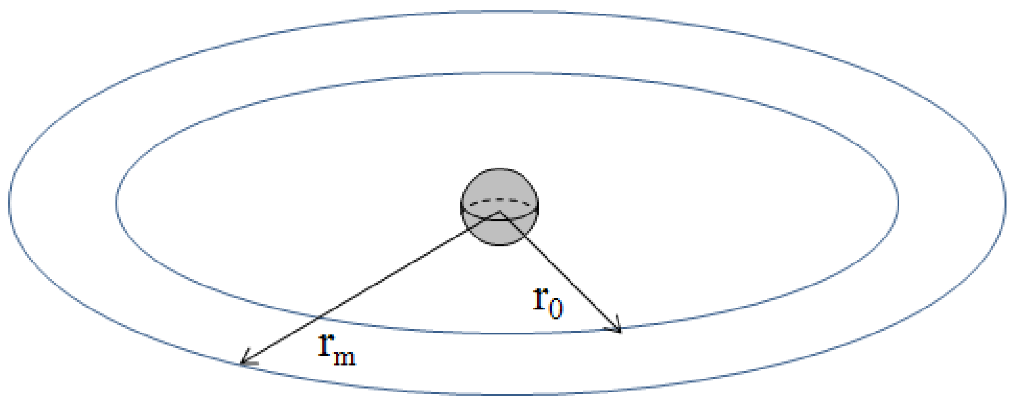

Figure 2.8. Sound waves at two different distances from a monopole. Note that the monopole size is greatly exaggerated so that it can be easily seen.

2.3.1.2 The near-field

When a transducer is comparable in size to a wavelength ($ka \approx 1$), complexities arise in the radiation pattern. They are the result of cancellation, and can be explained as the interference field that would result if one reconstructed the face of a transducer with a multitude of monopole sources. Phase differences between the monopoles cause complete cancellation when two sources are one half wavelength apart. Integrating over the face of the transducer, the complete interference pattern can be obtained. An example for a circular piston can be seen in Fig. 2.9.

As the distance from the transducer increases, these cancellation effects gradually become negligible. Once sufficiently outside of the near-field cancellation region, pressures can be related using $^1/_r$ decay. Any measurements that wish to use $^1/_r$ relationships must be measured sufficiently far away so that this assumption is valid. It can be seen in Fig. 2.9 that this will be geometry dependent. Those interested in on-axis calculation of the pressure field of specific face geometries are referred to Pierce [79].

In addition to on-axis cancellation effects, the directionality of the source also becomes more

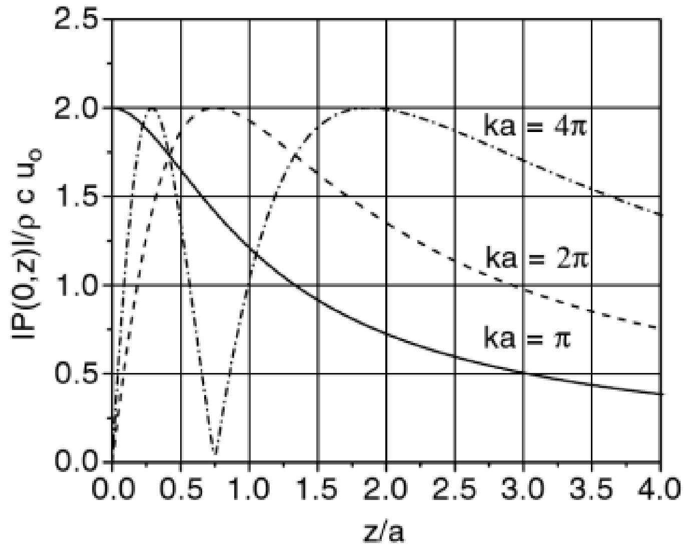

Figure 2.9. The near-field of a circular piston. The vertical axis is the pressure of the transducer on-axis, scaled by the characteristic acoustic impedance, ρc, and face velocity, u_0. The horizontal axis is the distance away from the transducer, z, normalized by the transducer face radius, a. Pressure is shown for several values of ka. Notice the pressure nulls that result at higher values of ka. From Sherman & Butler [14].

complex at higher frequencies. Angular nulls result from the same phase cancellation effects as on-axis nulls. These are also treated in Pierce.

2.3.1.3 Power requirements

Output or receive sensitivity of a transducer cannot be the sole measure of a device. Being part of a greater electrical network will place other demands on the design of the device. Coercive field of the active material may not be the limiting factor in drive level, as the power supply may not be able to exceed this limit. A successful design will be high output, but will also be designed to work with the amplifier and be efficient so that the power supply can kept to a reasonable size. For this reason, measures of transducer efficiency and output per unit power must be considered.

2.3.2 Measures of Transducers

2.3.2.1 Electrical impedance (Z_E)

The electrical impedance of a transducer is denoted as Z_E. It is defined as the ratio of complex voltage to complex current,

$$Z_E = \frac{V}{I} = \frac{V_{Re} + jV_{Im}}{I_{Re} + jI_{Im}} , \tag{2.14}$$

where V is the voltage, I is the current, and the subscripts Re and Im denote the real and imaginary parts of each. In this way, the phase relationship between the current and voltage can be maintained. Since phase is an arbitrary relationship, the phase of one quantity can be defined as the zero phase angle and the other can then be tracked off of it. In our case, consider current to be the baseline of zero phase. The relationships between current, voltage, and electrical impedance are then:

$$I = |I|cos(\omega t)$$

$$V = |Z||I|cos(\omega t + \theta_{Z_E})$$

$$\theta_{Z_E} = tan^{-1}\left(\frac{Z_{E,Im}}{Z_{E,Re}}\right)$$

In this work, the magnitude impedance will be used to identify the resonance and antiresonance frequencies of transducer modes. Notice the distinction of individual modes, as the spectrum of a transducer can have multiple impedance minima and maxima depending upon the frequency band considered. The electrical resonance frequency, f_r, is the frequency of minimum electrical impedance and the antiresonance frequency, f_a, is the frequency of maximum electrical impedance, as seen in Fig. 2.10:

2.3.2.2 Radiation resistance (R_r) and reactance (X_r)

Similar to an electrical impedance relating voltage to current, a mechanical impedance can be defined that relates force to particle velocity,

$$Z_A = \frac{F}{v} = R_r + jX_r \ , \tag{2.15}$$

where R_r is the radiation resistance, and X_r is the radiation reactance. Similar to electrical impedance, the radiation resistance and reactance can be used to track the phase between force and particle velocity.

The higher the radiation resistance of a transducer is, the more effective the transducer can be as a projector. The concept of a high resistance being good seems counter-intuitive, but the reason for this measure lies in the electrical circuit analogs to transducers. Resistors are elements that dissipate power, and a radiation resistance is the element that is used to model power dissipated acoustically[8]. Since this is the purpose of the transducer, a higher value of resistance is desirable. Radiation resistance trends up with increasing frequency[9], and an example of this effect for a circular piston can be seen in Fig. 2.11.

[8] In this case radiation resistances is mechanical power being dissipated acoustically. A transformation factor needs to be used to make sure the units match up.

[9] As noted before, ka is a non-dimensional measure of the size of a transducer to the wavelength of sound. Increasing ka is analogous to increasing frequency.

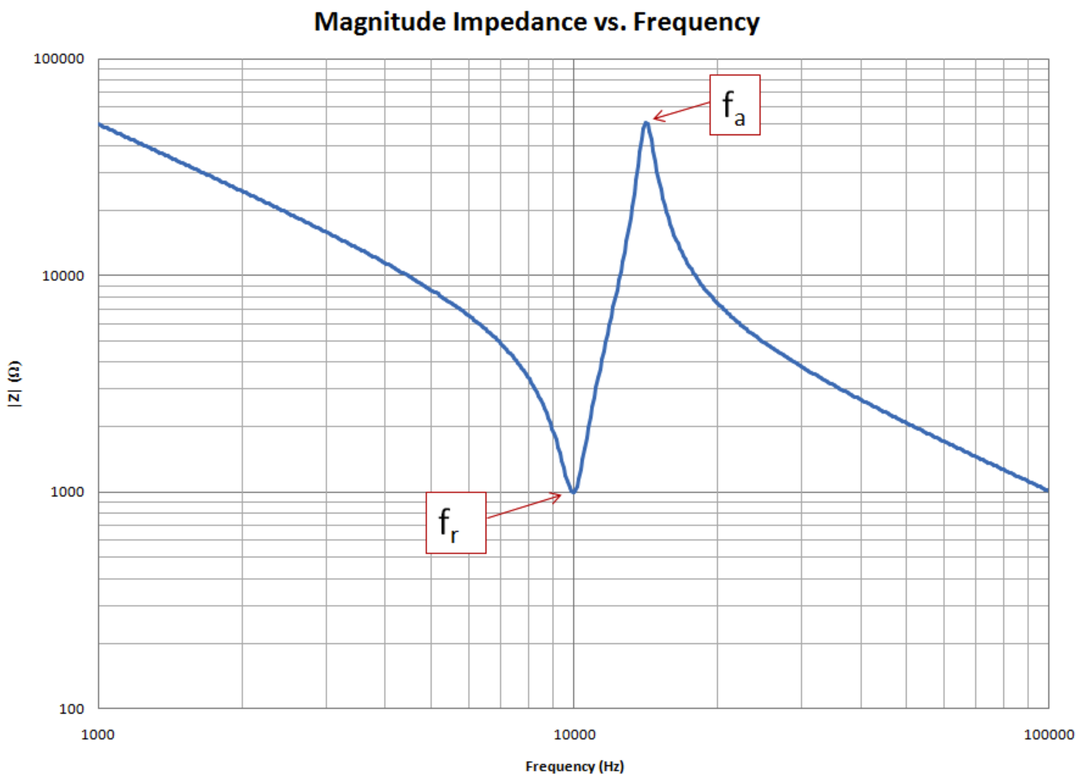

Figure 2.10. An impedance curve for the equivalent circuit in Fig. 2.12. The values of the components are: $C_0 = 10\,nF$, $C_{me,eq} = 10\,nF$, $R_{me,eq} = 1000\,\Omega$, and $L_{me,eq} = 1\,H$.

At frequencies where the transducer is smaller than a wavelength $(ka < 1)$ reactance dominates the acoustic impedance due to effects of *entrained mass*. In this lower frequency range, energy is transferred back and forth between the structure and the fluid as the transducer attempts to move the fluid out of the way. This results in an entrained mass that moves with the structure. This mass of fluid drives the resonance frequency of the transducer down, as there is more positive "mass-like" reactance to balance the negative "stiffness" reactance of the transducer. This definition of resonance frequency will be discussed later. An example of the radiation reactance of a circular piston can be seen in Fig. 2.11. As frequency increases the reactance diminishes in relation to the radiation resistance.

2.3.2.3 Transmit Voltage Response (TVR)

TVR, is a measure of a transducer's response that allows for normalization to a standard distance and drive level:

$$TVR = 20\,log\left(\frac{P_m r_m / V_m}{P_0 r_0 / V_0}\right) = 20\,log\left(10^6 \frac{[V]}{[Pa][m]}\frac{P_m r_m}{V_m}\right) \tag{2.16}$$

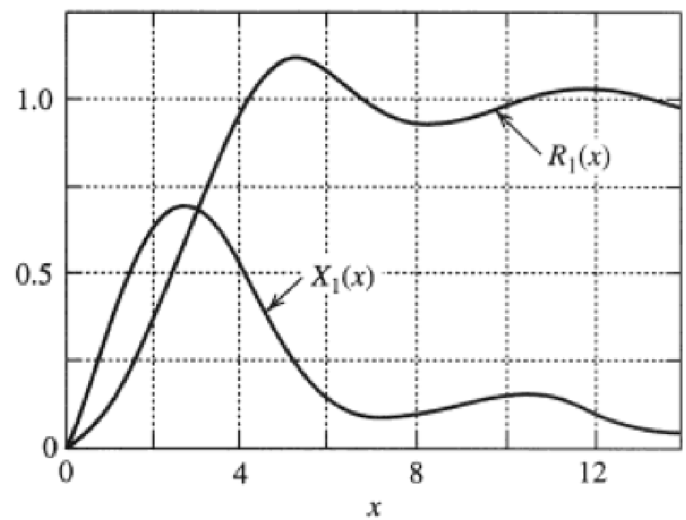

Figure 2.11. The radiation resistance, R_r, and reactance, X_r of a circular piston plotted vs. the ka product of the transducer. The horizontal axis has been normalized by $2ka$, meaning that $x = 1$ denotes $2ka$, x=2 denotes $4ka$, and so on. On the vertical axis $R_1 = R_r/(\rho_0 c_0 S)$ and $X_1 = X_r/(\rho_0 c_0 S)$ where ρ_0 is density of the acoustic fluid, c_0 is the speed of sound in the fluid, and S is the surface area of the radiating face. From Kinsler, et al. [80].

TVR is reported in dB with respect to an ideal source that produces 1 μPa (P_0) at a distance of 1 m (r_0) when driven with 1 V_{rms} (V_0). V_m, P_m and r_m are the measured or modeled values for the transducer[10]. Because power is proportional to pressure squared, and dB is a ratio of powers, the constant becomes 20 instead of the usual 10 in dB calculations. The 10^6 factor comes from the inverse of 1 μPa.

2.3.2.4 Source Level (SL)

TVR is not always a good metric for comparing different transducer designs. This is especially true when there are large differences in geometry or active material from one design to another. Stress, electric field, and power limits are not accounted for in TVR, and each can impact the maximum acoustic output of a transducer.

Source Level is a measure of the output of a transducer with a given voltage input:

$$SL = TVR + 20\,log\left(\frac{V_{drive}}{V_0}\right) \tag{2.17}$$

The reference voltage, V_0, is 1 Volt. In this way SL is a measure of the pressure attainable with a drive voltage, assuming that there is a linear relationship between the two. The maximum drive voltage can be limited by any of the factors listed above (stress, electric field, and power limits). Once the maximum drive voltage is determined, then the maximum source level can be

[10] This convention will be kept for the remainder of the work

calculated:

$$SL_{max} = TVR + 20\,log\left(\frac{V_{max}}{V_0}\right)$$

Maximum source level offers a fair comparison between transducers because it takes the inherent limits into account. However, by including these limits, the maximum source level can obscure the required drive field or power level. If the designer is more concerned with tracking response with respect to a specific limit, other measures can be defined.

2.3.2.5 Transmit Field Response (TFR)

If the concern of the designer is the electric field (E_m) that the device is being driven at, then TFR offers a good measure of performance:

$$TFR = 20\,log\left(\frac{{}^{P_m r_m}/_{E_m}}{{}^{P_0 r_0}/_{E_0}}\right) = 20\,log\left(10^6 \frac{\left[\frac{V}{mm}\right]}{[Pa][m]} \frac{P_m r_m}{E_m}\right) \tag{2.18}$$

If several transducers are being compared with the same coercive field, then TFR will show which has the greatest output for a given field. This allows for consideration of output without concern for the maximum drive voltage that can be generated.

2.3.2.6 Transmit Volt-Amp Response ($TVAR$)

Finally, $TVAR$ offers a good measure when power concerns are of greatest importance. The volt-amp product is calculated by first obtaining the current in the device though the following equation:

$$I = \frac{V}{|Z|}$$

Once the current is known, the magnitude of the current can be multiplied by the magnitude of the voltage to obtain the volt-amp product. This is then used as the measure of the drive for the transducer, and it is compared to a standard of 1 volt-amp of power in the $TVAR$:

$$TVAR = 10\,log\left(\frac{{}^{(P_m r_m)^2}/_{V_m I_m}}{{}^{(P_0 r_0)^2}/_{V_0 I_0}}\right) = 10\,log\left(\frac{{}^{(P_m r_m)^2|Z_m|}/_{V_m^2}}{{}^{(P_0 r_0)^2}/_{V_0 I_0}}\right) \tag{2.19}$$

$$TVAR = 10\,log\left(10^{12} \frac{[VA]}{[Pa]^2[m]^2} \frac{(P_m r_m)^2\,|Z_m|}{V_m^2}\right)$$

Note that the pressure quantity in the equation is now squared. This is due to the fact that the volt-amp product is proportional to drive voltage squared. If linearity holds, and output pressure is proportional to drive field, then the volt-amp product must be proportional to pressure squared. Because both pressure squared and the volt-amp product are power quantities, the logarithm is multiplied by 10 instead of the usual 20 for pressure.

Because $TVAR$ scales output pressure by energy consumption, it is an efficiency of sorts. This allows for easy comparison of multiple transducers showing maximum output per unit power required. However, due to the fact that directionality is not explicitly dealt with, this is not a true efficiency. For this, we will need another definition. Section 2.3.2.8 will cover a definition of electroacoustic efficiency.

2.3.2.7 The electromechanical coupling coefficient (κ^2)

The electromechanical coupling coefficient cannot be understood without first introducing a simple equivalent circuit model of a transducer. The derivation based off of this model follows that of Wilson [37].

Because mechanical impedances have analogs with electrical circuit components, they are often represented this way. Electrical impedances of a resistor, inductor, and capacitor can be calculated by the following:

$$Z_{resistor} = R$$

$$Z_{inductor} = j\omega L$$

$$Z_{capacitor} = \frac{1}{j\omega C}$$

Similarly the mechanical impedance definition and resultant impedances of a dashpot, mass, and capacitor are:

$$Z_{mech} = \frac{Force}{velocity}$$

$$Z_{dashpot} = R_{me}$$

$$Z_{mass} = j\omega m_{me}$$

$$Z_{compliance} = \frac{1}{j\omega C_{me}}$$

Using these similarities, equivalent electrical circuits of mechanical systems can be drawn. This allows for coupling electrical and mechanical systems in one circuit diagram, a useful concept for transducer designers. An example of an equivalent circuit can be seen in Fig. 2.12.

In the above figure $R_{me,eq}$, $C_{me,eq}$, and $L_{me,eq}$ are the electrical equivalents of the mechanical (or *motional*) impedance of a dashpot (R_{me}), compliance (C_{me}), and mass (m_{me}). Their mechanical values can be related to their electrical values by a coefficient that is transducer-specific.

The word motional is emphasized, because there is also a shunt capacitor, C_0. This represents

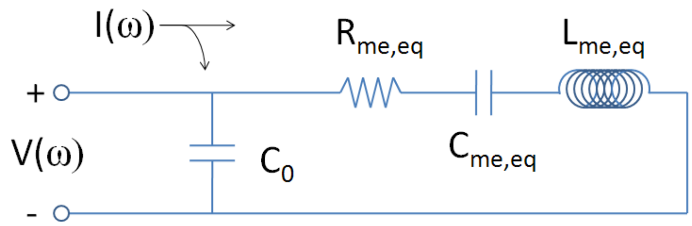

Figure 2.12. A basic equivalent circuit model of a transducer.

the capacitance that would be measured if the transducer wasn't allowed to move. C_0 is also known as the *blocked* capacitance.

A coupling coefficient can then be defined that gives a ratio of the useful energy in the device to the total energy in the circuit:

$$\kappa^2 = \frac{Motional\ energy}{Total\ Energy}$$

Assuming that the circuit is analyzed at low-frequency, where the capacitive impedances will dominate, the energies and coupling can be calculated as:

$$Motional\ Energy = \frac{C_{me,eq}V^2}{2}$$

$$Total\ Energy = \frac{(C_{me,eq} + C_0)\, V^2}{2}$$

$$\kappa^2 = \frac{C_{me,eq}}{C_{me,eq} + C_0}$$

This can be put in terms of the series (minimum impedance) and parallel (maximum impedance) resonance frequencies of the circuit through the following relations:

$$f_s = \frac{1}{2\pi}\sqrt{\frac{1}{L_{me,eq}C_{me,eq}}}$$

$$f_p = \frac{1}{2\pi}\sqrt{\frac{1}{L_{me}}\frac{C_0 + C_{me,eq}}{C_0 C_{me,eq}}}$$

$$\kappa^2 = 1 - \frac{f_s^2}{f_p^2}$$

The series resonance results from the positive reactance of the mass canceling the effect of the negative reactance of the compliance. This is a common definition for resonance frequency of a mechanical transducer.

The frequencies f_s and f_p would be the measured electrical resonance and antiresonance frequencies of this simplified circuit, however this would not be the case for a real transducer where measurable losses and other inductances and capacitances are present. Despite the fact that these frequencies are not exactly equal, the measured electrical resonance and antiresonance frequencies of an actual transducer, f_r and f_a, are often used to calculate the coupling coefficient:

$$\kappa^2 = 1 - \frac{f_r^2}{f_a^2} \tag{2.20}$$

The measurement of the coupling coefficient is also often reported as effective coupling, κ_{eff}, which is the square root of the coupling coefficient:

$$\kappa_{eff} = \sqrt{1 - \frac{f_r^2}{f_a^2}} \tag{2.21}$$

Effective coupling is most often denoted, k_{eff}. This notation will not be used here, however, as k has already been used for the wavenumber of the acoustic wave.

The effective coupling is a useful measure of bandwidth, as the relative spread in resonance and antiresonance frequencies will give an idea of the sharpness of a resonance peak. The further apart resonance and antiresonance are, the closer κ_{eff} is to one.

κ^2 can be considered to be a ratio of amplitudes, comparing the ideal electrical equivalent amplitude of the output to the voltage input [82]. However, despite the fact that this looks like an efficiency and the fact that coupling was derived as a ratio of energies, it is not recommended that it be used to measure efficiency of a transducer. This is because it is derived as a low-frequency approximation where losses are assumed to be overridden by capacitance. In-water measurement of transducers is a very different scenario than the one used to derive this measure. As such, an electroacoustic efficiency for a transducer must be defined.

2.3.2.8 Electroacoustic efficiency (η_{EA})

Fundamentally, an efficiency compares useful power that a system can produce with the power that was put in to produce it. For an electroacoustic transducer, this quantity is a combination of the electrical to mechanical efficiency, η_{EM}, and the mechanical to acoustical efficiency, η_{MA}:

$$\eta_{EA} = \eta_{EM}\eta_{MA} = \frac{W_{acoustic}}{W_{electrical}} \tag{2.22}$$

For ideal transducers, equivalent circuit models can be solved to determine mechanical and acoustical output power for a given power input. This will allow for prediction of the efficiency if good models of the losses, radiation resistance, and directivity can be made.

In the case of actual transducers, the electroacoustic efficiency can be calculated by measuring the input power, the output pressure or intensity, and the directivity of the transducer. First, the maximum acoustic intensity, I_m, is measured or calculated from the pressure[11]:

$$I_m = \frac{P_m^2}{\rho c}$$

Next, the directivity factor, D_f is defined as the ratio of the maximum acoustic intensity to the average acoustic intensity over all directions [14]:

$$D_f = \frac{I_{m,max}}{I_{m,avg}}$$

The directivity factor can be measured or calculated analytically depending upon transducer geometry. If the directivity factor has been obtained, the average intensity can be found and the total acoustic power of the source can then be calculated:

$$W_{acoustic} = 4\pi r_m^2 \frac{I_{m,max}}{D_f}$$

At this point the electroacoustic efficiency may be calculated using Eq. 2.22. This measure of transducer efficiency is much more practical than equivalent circuit models, as their inherent assumptions are removed.

2.4 Cymbal Transducers

2.4.1 Displacement Amplification

A basic model for displacement amplification of a cymbal transducer was developed by Fernandez, et al. in 1997 [83]. The model assumes that for low Young's modulus cap materials, measured at low frequency, the cap can be modeled as a mechanical linkage with a pin joint at the four inflection points as seen below (Fig. 2.13):

Using this linkage model, it can be shown that the displacement of the transducer is:

$$d_c + \Delta d_c = \sqrt{l^2 - \left[\frac{d_2 + \Delta d_2 - d_1}{2}\right]^2} \tag{2.23}$$

$$\text{where } \Delta d_2 = d_{31} E d_2$$

The operator Δ stands for the change of a variable, d_1, d_2, and d_c can be referenced in Fig. 2.13, d_{31} is the transverse piezoelectric field coefficient, and E is the applied electric field. Note that d_{31} should not be confused with d_1 and d_2, which are both diameters, or d_c which is the depth of the cap. It can be seen that displacement amplification can be increased if cavity depth (d_c) is decreased.

[11] This equation is only valid far from a source, where the pressure and velocity can be assumed to be in-phase. For more detail, see Kinsler, et al. [80]

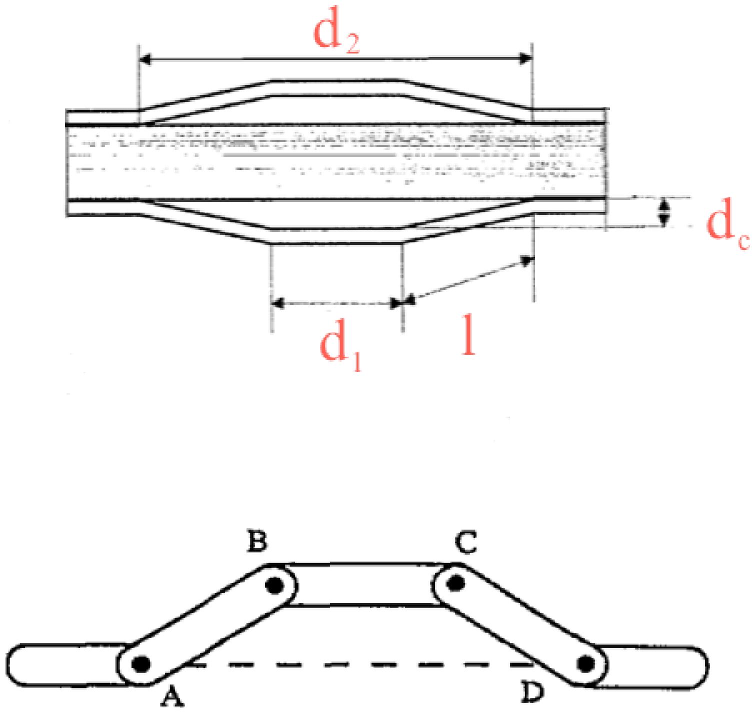

Figure 2.13. A cymbal transducer, with the relevant dimensions highlighted (top) and a basic model for a low-modulus cymbal cap (bottom). Adapted from [83] with re-notated dimensions in red.

Taking the above derivation one step further, we can relate l to d_2 and d_1 and we obtain:

$$l^2 = \left(\frac{d_2 - d_1}{2}\right)^2 + d_c^2$$

$$d_c + \Delta d_c = \sqrt{\left(\frac{d_2 - d_1}{2}\right)^2 + d_c^2 - \left[\frac{d_2 + \Delta d_2 - d_1}{2}\right]^2}$$

$$d_c + \Delta d_c = \sqrt{\frac{d_2^2 - 2d_2d_1 + d_1^2}{4} + d_c^2 - \frac{d_2^2 + 2d_2\Delta d_2 - 2d_2d_1 + \Delta d_2^2 - 2\Delta d_2 d_1 + d_1^2}{4}}$$

$$d_c + \Delta d_c = \sqrt{\frac{2\Delta d_2 d_1 - 2\Delta d_2 d_1 - \Delta d_2^2 + 4d_c^2}{4}}$$

Plugging in the equation for Δd_2 from Eq. 2.23 and simplifying:

$$\Delta d_c = \sqrt{\frac{4d_c^2 + d_{31}Ed_2\left[2d_1 - (2 + d_{31})\,d_2\right]}{4}} - d_c \tag{2.24}$$

It can now be seen that with d_{31} being both small (relative to 2) and negative, that it is desirable to have the cavity diameter (d_2) to be as large as possible and the apex diameter (d_1) be as small as possible for large displacements (Δd_c). Also, a larger percent change will be seen if d_c is small compared to the other quantities in Eq. (2.24).

The derivation was not taken as far as Eq. (2.24) in the paper by Fernandez, but similar qualitative trends were predicted. The displacements they predicted with Eq. (2.23) were found to be quite accurate in lower Young's modulus materials, and the prediction of the pin joint model breaking down at higher moduli was confirmed [83]. In addition, a similar derivation (though not exact) was carried out by Sun, et al. which also included the increase in thickness of the active disk due to d_{33} axial elongation [84].

2.4.2 Resonance frequency

In 2002, Newnham, et al. reported a proportionality for the resonance frequency of cymbals based on shallow shell theory [85]:

$$f_r \propto \sqrt{\frac{Y}{\rho_c}\left[\frac{1}{d_2^2\left(1-\nu^2\right)}+\frac{1}{R^2}\right]} \tag{2.25}$$

In the above equation ρ_c is the density of the end cap, ν is the Poisson's ratio, and R is the radius of the device. This proportionality shows the relative strength of the cavity radius (d_2) and device radius in determining the resonance frequency of the cymbal transducer. In addition, similar to most structural acoustics problems, it can be seen that when choosing a cap material, both the stiffness and the density must be considered.

Chapter 3

Methods & Modeling

3.1 Design concept

3.1.1 Benchmark design & model

A known low-profile array design was selected as a promising candidate for [011] poled PMN-29PT active material substitution. The benchmark array consists of 25 cymbal transducers made of [001] poled PMN-30PT, poled through the thickness dimension of the disk. These individual cymbals are then attached to two stiff and lightweight cover plates for the purpose of making a projector that is lower frequency and higher output.

3.1.1.1 Individual cymbal

The individual cymbals are similar to the traditional cymbal design discussed in Chapter 1. The primary difference is that two titanium studs are attached to each cymbal cap. This design was patented by Howarth, et al. in 2004 [86]. The studs are for attaching the cymbals to a cover plate, which lowers the resonance frequency and increases the radiation resistance, as discussed in Chapter 2. Both the cap and the stud are made of titanium.

An individual cymbal half cross section is shown in Fig. 3.1. The corresponding normalized dimensions, including the stud, can be found below in Table 3.1. All normalized dimensions reported will be with respect to (w.r.t.) the diameter of this individual benchmark cymbal, ϕ.

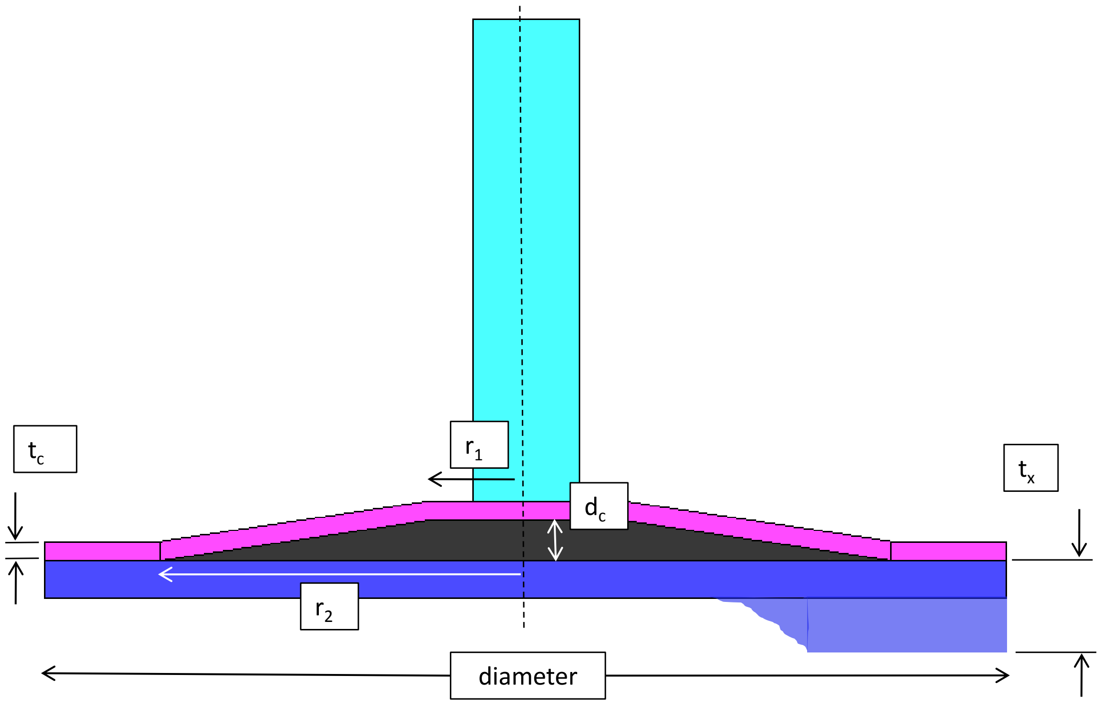

Figure 3.1. A half cross section of an individual benchmark cymbal w/ normalized dimensions. There is symmetry about the mid-plane, as implied by the t_x dimension.

diameter	ϕ
d_c	0.040 ϕ
r_1	0.100 ϕ
r_2	0.380 ϕ
t_c	0.020 ϕ
t_x	0.079 ϕ
stud length	0.500 ϕ
stud diameter	0.110 ϕ

Table 3.1. Normalized dimensions for the cymbal in Fig. 3.1.

3.1.1.2 Array

The benchmark array is made up of 25 cymbals attached to an epoxy composite plate as shown below in Fig. 3.2. This figure shows the symmetry that can be used to build the FEA model. It also shows the nuts and washers that would be used to attach the cymbal to the plate. For reasons of model simplicity, these were eventually removed. This is discussed further in the section on model simplifications. The normalized dimensions for the benchmark array are listed in Table 3.2.

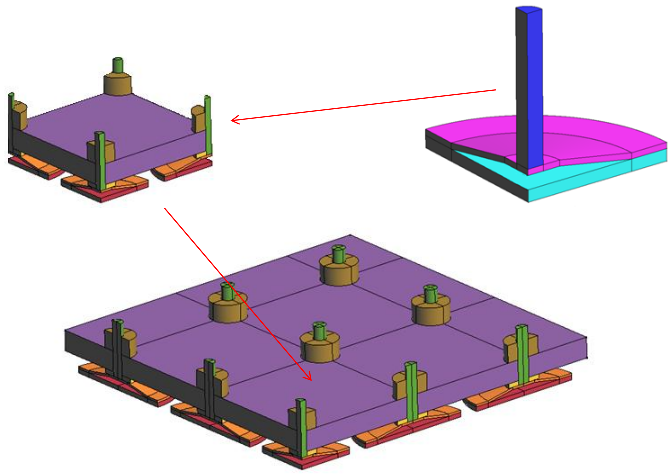

Figure 3.2. An early FEA model of the benchmark cymbal, cover plate building block, and array. The array and cymbal are shown as $^1/_8$ models indicative of 3-fold symmetry about the coordinate system.

plate thickness	0.18 ϕ
length	6.00 ϕ
width	6.00 ϕ
washer thickness	0.08 ϕ

Table 3.2. Normalized dimensions for the array in Fig. 3.2.

3.1.2 Motivating material properties

The targeted material property in the [011] poled material is the high d_{32} coefficient, but several other material properties are relevant to the problem. In the [001] poled material, the d_{31} coefficient and the d_{32} are approximately equal[1], which lends this design to a traditional axisymmetric cymbal cap. For the models of the benchmark array, the [001] crystal was defined with tetragonal $4mm$ symmetry, which means that $d_{32} = d_{31}$.

This is not true of the [011] material, where there are distinct d_{31} and d_{32} coefficients with $mm2$ symmetry indicative of an orthorhombic crystal. Additionally, the d_{31} coefficient is of opposite sign to the d_{32} coefficient. These two sets of coefficients can be seen in Table 3.3. A d_{32} coefficient of [001] crystal isn't given due to the 4mm symmetry mentioned above.

In addition to an excellent d_{32} coefficient, the [011] poled material has excellent coupling for this mode of operation. This is also compared to the [001] material in Table 3.3. It was predicted that with increased piezoelectric coefficients and coupling that a higher-output and broader bandwidth array could be designed.

[1] They are not exactly equal, but the difference was assumed to be small enough to use 4mm symmetry

Crystal	$d_{31}\left[\frac{pC}{N}\right]$	$d_{32}\left[\frac{pC}{N}\right]$	$d_{33}\left[\frac{pC}{N}\right]$	κ_{31}	κ_{32}	κ_{33}
[001] PMN-30PT	-921	N/A	1981	0.49	N/A	0.92
[011] PMN-29PT	610	-1883	1020	0.76	0.94	0.78

Table 3.3. A comparison of targeted properties between [001] poled PMN-30PT and [011] poled PMN-29PT. The properties for [001] poled PMN-30PT are from Zhang, et al. [87] and [011] poled PMN-29PT are from Wang, et al. [1].

3.1.3 Open capped cymbal

To understand the need for an open capped cymbal, first consider the deformation of a traditional cymbal transducer under an applied field (Fig. 3.3). As the field is applied across the device, it expands along its thickness dimension, and contracts in towards the axis of symmetry. This contraction causes the cymbal cap to rotate away from the active material and bulge out, producing the displacement amplification. An exaggerated example of the asymmetry caused by variations in transverse coefficient of the [001] poled single crystal about its axis can be seen in the top right view.

For the [011] poled material being considered, the opposite sign d_{31} and d_{32} coefficients would cause the cap to work against itself if it were sealed all the way around the device. To alleviate this problem, the cap is left open on two of the four ends, and the device operates as shown in Fig. 3.4.

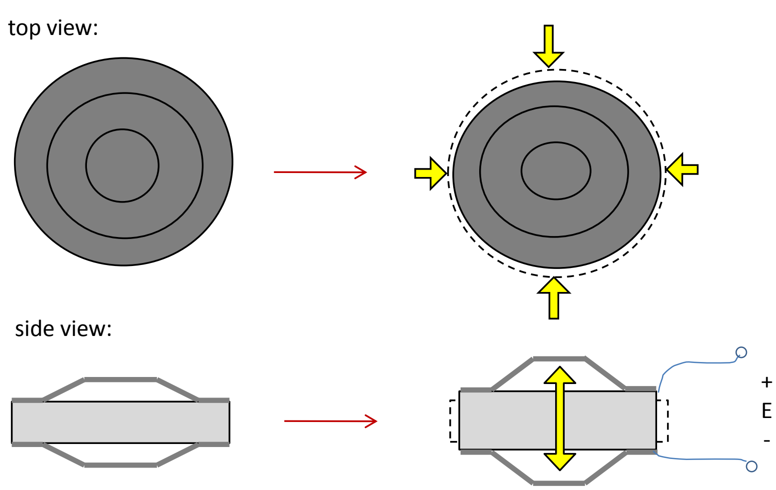

Figure 3.3. A traditional cymbal transducer deforming under an applied electric field. The side view is an axisymmetric cross section, but is shown without depth shading for clarity.

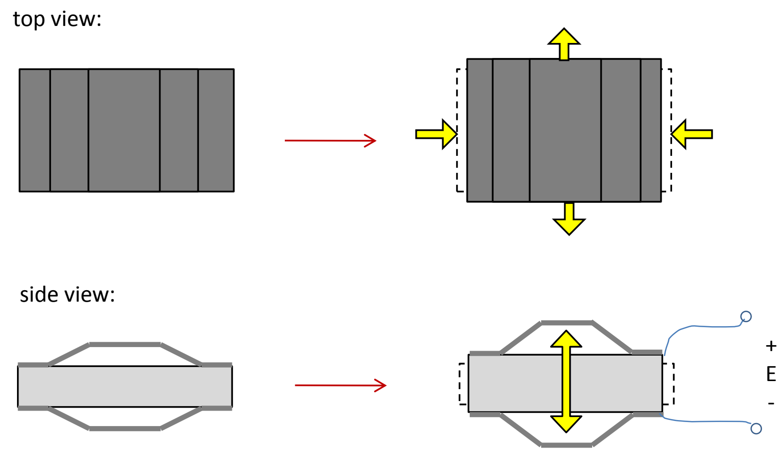

Figure 3.4. A rectangular cymbal transducer deforming under an applied electric field. The side view of the cap is accurate in this case, as the cap is open into and out of the page.

3.2 FEA model

3.2.1 GiD

GiD is a front-end program for use with FEA codes [88]. It allows for pre- and post-processing of the finite element models, as well as creating the finite element mesh. The software is integrated so closely with the FEA solver that all analysis can be done from within GiD, which calls the solver (ATILA in this case) as necessary. GiD 9.0.2 was used in the construction and analysis of all models in this work.

3.2.1.1 Preprocessing

The GiD pre-processor allows for creation of model geometry and meshing. In a 3D model, there are 4 levels of geometry: points, lines, surfaces, and volumes. Each level is defined by multiple elements at a lower level (e.g. A rectangular prism is a volume made up of six or more surfaces as shown in Fig. 3.5). Using these building blocks, complex geometries can be defined.

The construction of the model in the pre-processing environment must be done carefully. Volumes that share surfaces will be rigidly connected across those surfaces. Volumes that do not share surfaces will not be connected, and can pass through each other during deformation of the mesh. In the GiD/ATILA package, pin joints, rolling surfaces, no-slip boundary conditions and the like are not possible. All connections must be rigid or the surfaces must be separate entities. In the model shown in Fig 3.6, the cymbals share surfaces with the single-crystal disks and the studs share surfaces with the epoxy cover plate in the areas that are seen in contact. This enforces that these surfaces see the same displacements during operation.

Boundary conditions are also defined in the pre-processor environment. These will be treated in the section on required ATILA inputs.

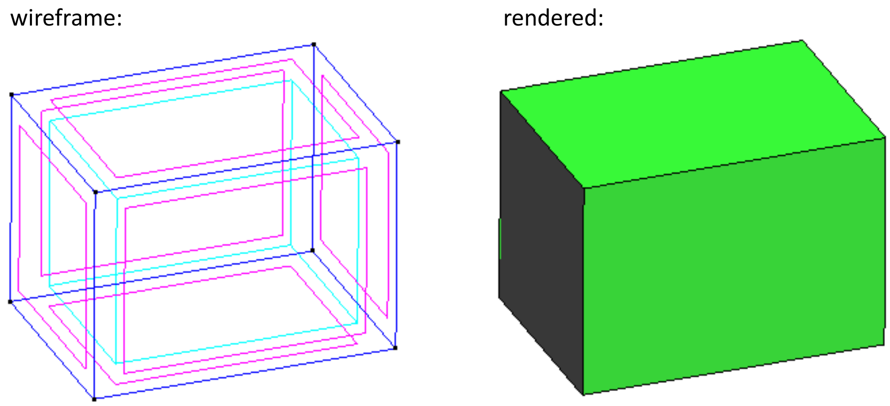

Figure 3.5. A rectangular prism modeled in GiD. On the left the geometric elements can be seen in wire frame mode. The volume element (light blue) is defined by six surfaces (pink), which are in turn defined by lines (dark blue), which are defined by points (black). In render mode the prism appears as it does on the right.

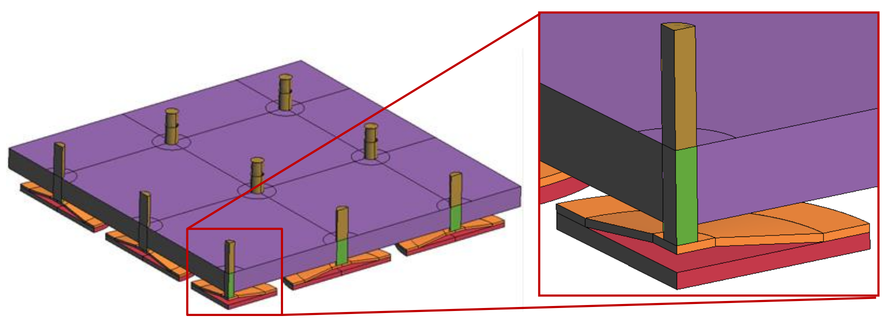

Figure 3.6. The finalized geometry of the benchmark array. The surfaces between the stud and cover plate, stud and cymbal cap, and between the cap and single-crystal disk are shared. Though the washer has been removed, the spacing it provides was kept the same.

3.2.1.2 Meshing

Meshing of volumes is technically part of the pre-processing environment in GiD. It is covered separately here to highlight several important choices that must be made. For this model tetrahedral elements were chosen to mesh the geometry. This was done primarily because of the many curved surfaces (spherical water boundary, circular cymbals, etc.) that don't lend themselves to definition by block elements.

Second, quadratic elements were used. During early trials with the program it was found that a minimum criteria of 5 quadratic elements per acoustic wavelength gave sufficient convergence of the solution. A detailed convergence study will be presented in the results.

Automatic meshing was used on these models. GiD allows for mesh size criteria to be set on any geometry (point, line, surface or volume), which is helpful if the automatic mesh generator has trouble finding a solution. Drastic changes in geometry may require that the user specifies a smaller mesh size in small or complex locations so that the mesh generation will have a better chance of success. However, this was not necessary for the models in this work.

Finally, the mesh was smoothed prior to solving. This was done to avoid distorted elements with a high aspect ratio. It is a common problem in FEA codes that relatively long and narrow elements can cause problems with matrix solution, and ATILA is no exception. GiD's built-in smoothing function allows for the mesh to be fixed in this regard prior to solution. A view of the final meshed geometry for the benchmark array can be seen in Fig. 3.7.

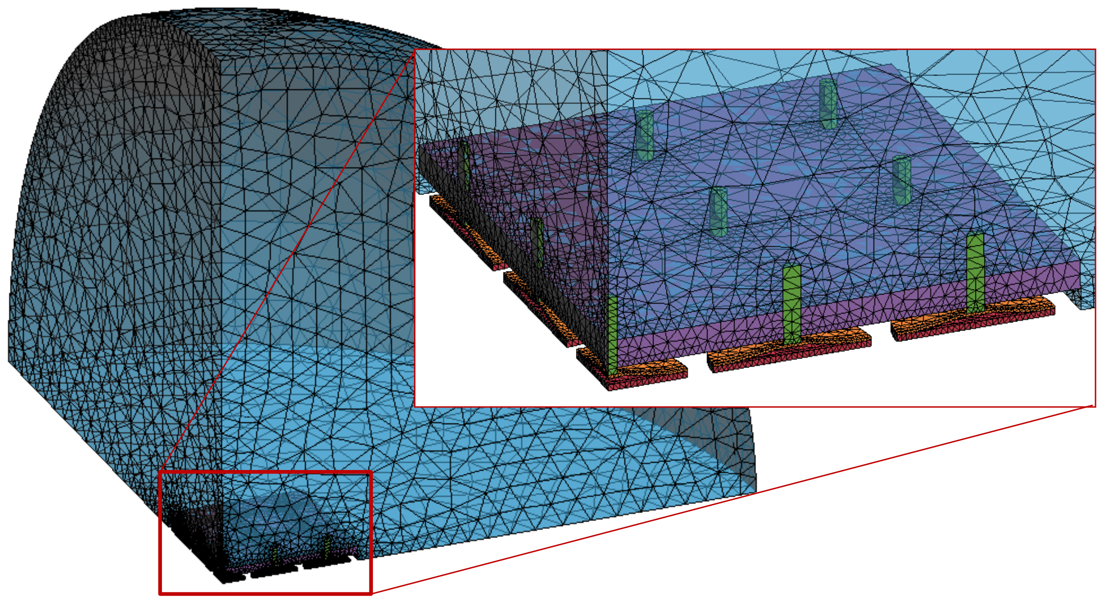

Figure 3.7. The meshed geometry for the benchmark array with a translucent water volume.

3.2.1.3 Postprocessing

After solution of a model, GiD loads the output file to aid in results analysis. Depending upon the solution parameters chosen by the user many outputs can be viewed, including but not limited to: stresses, electric field, displacements, pressures, and deformation (strains). The visual interface of GiD allows for quick identification and selection of nodes where these outputs are desired, as well as interpolated color plots showing the spatial variation of these outputs. Values at selected nodes can then be plotted against frequency, distance or time. The possible outputs depend upon the type of solution run (harmonic, transient, modal, etc.) and the selections in the ATILA Problem Data window. Magnitude, real or imaginary values can be obtained for complex values.

For the results that follow in the next chapter, two quantities were pulled from the output file. In the case of individual cymbals, the magnitude displacement versus frequency was output for the tip of the stud. This was done because the stud doesn't exhibit modal behavior in this frequency range and should give a good representation of the usable displacement of the transducer.

For the array model in-water results, the magnitude pressure on-axis versus frequency was output. This, along with the dimension of the water boundary, allowed for calculation of the model TFR and $TVAR$ as laid out in Chapter 2. Additionally, the magnitude pressure versus distance away from the transducer face was output to study the near-field effects of the transducer.

Animations of deformation can be created from the output file. These allow for the user to check that the transducer is behaving in a reasonable manner (i.e. volumes that are supposed to be connected actually are), and to visualize the modal behavior of the structure. They are often useful in iteration of models, as they can help quickly identify the cause of spurious modes and dips in transducer response.

3.2.2 ATILA

In order to solve the model, ATILA needs a number of inputs. The following sections cover the relevant inputs for the solution of the problem statement of this work. Additional information on problem inputs can be found in the ATILA user guide [78]. ATILA version 3.0.17 was used in the solution of all models.

3.2.2.1 Problem Data

The Problem Data window in the GiD/ATILA package consists of a number of basic solution options. In the window there are four tabs: Problem Data, Mesh Units, Symmetries, and Tools. In Problem Data tab, analysis was set to harmonic and 'Include losses' was checked so that dynamic material properties were used in the solution of the model. This tab is where the user can specify that stresses be written to the output file. In this case stresses were not written, as it significantly increases output load times.

Under the Mesh Units tab, the default units of measure can be selected for the model. An appropriate unit was selected for the geometry to be modeled.

The Symmetries tab allows for the selection of xy, yz, and xz planar symmetry conditions for both displacement and electric field. Both the individual cymbal and array have 3-fold symmetry, so displacement symmetries were selected for all planes with the exception of the individual rectangular cymbal[2]. Electric field symmetries were not enforced, as this can be done with the electrical potential boundary conditions, as will be seen later. In both cases the planar symmetries are denoted by the plane normal vector (e.g. x-symmetry denotes use of the yz symmetry plane).

The tools tab allows for writing of the far field pressure on the radiating boundary. This gives an easy visualization of the radiation pattern in post-process, but adds to the output file size.

[2]As laid out later, the individual rectangular cymbal was modeled with z-symmetry only as this made for easier incorporation into the array model.

3.2.2.2 Polarization

The polarization vector for the active material must be defined in terms of the coordinate system of the model. This makes it possible to define the transducer geometry in a separate coordinate system from the active material.

Multiple polarization vectors can be defined, depending upon needs. For the sake of this model only one was needed. Once the vector was defined, it was assigned as a body polarization on all volumes that would be piezoelectric. An example of this is shown in Fig. 3.8, where an individual cymbal is shown with polarization of the single-crystal disk. It was important that the correct polarization axis alignment was used for the [011] poled material. Because the d_{31} and d_{32} coefficients are different, they must be correctly aligned with the x- and y-axis respectively.

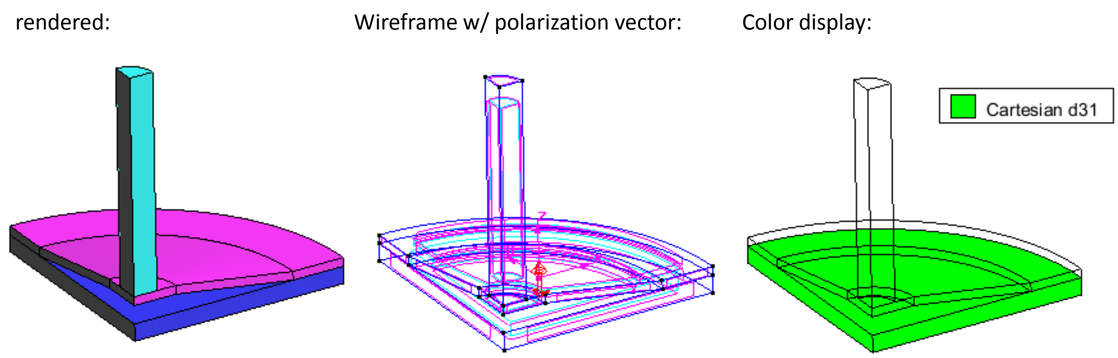

Figure 3.8. An example of the polarization vector in an individual cymbal. Views of the rendered $^1/_8$ model, wire-frame model with polarization vector (red), and color display of polarization are shown.

3.2.2.3 Electric Field

The electrodes of the transducer are defined as electrical potentials on surfaces of the model. By making two parallel surfaces of different potentials, an electric field constraint is enforced for the device. For this work a field of 1 $\left[\frac{V}{mm}\right]$ was used for all models. The electrical potential boundary condition for an individual cymbal can be seen in Fig. 3.9.

The field is created by using half of the potential (0.5 $\left[\frac{V}{mm}\right]$ times the thickness in millimeters) on the top electrode, and enforcing an electrical ground condition on the mid-plane. This will provide the correct drive conditions, but the electrical impedance of the model will have to be adjusted to match the measured device

The equation for capacitance of a dielectric material is:

$$C = \epsilon_r \epsilon_0 \frac{A}{t}$$

where ϵ_r is the relative permittivity, ϵ_0 is the permittivity of free space, A is the surface area of the electrode, and t is the distance between the electrodes. An electrical impedance proportionality can then be drawn from the following restatement of the theory in Chapter 2:

$$Z_E = \frac{1}{j\omega C}$$

$$Z_E \propto \frac{t}{A}$$

If the model values are taken as subscript m, and the actual values as subscript a, the following can be seen about the relationship between the one eighth model and the transducer as designed:

$$Z_{E,a} \propto \frac{t_a}{A_a} = \frac{2t_m}{4A_m} \propto \frac{2}{4} Z_{E,m}$$

$$\therefore\ Z_{E,a} = \frac{Z_{E,m}}{2} \tag{3.1}$$

As such, electrical impedance of all models was divided by two. The only exception to this was for individual rectangular cymbals. For reasons of easier implementation into the array, these cymbals were modeled with just one symmetry plane, the z (thickness) symmetry. Their impedance was therefore multiplied by two, as their area term was unchanged from actual to model. This is another reminder that symmetry conditions can make the models solve much faster, but the implications must always be understood when analyzing results.

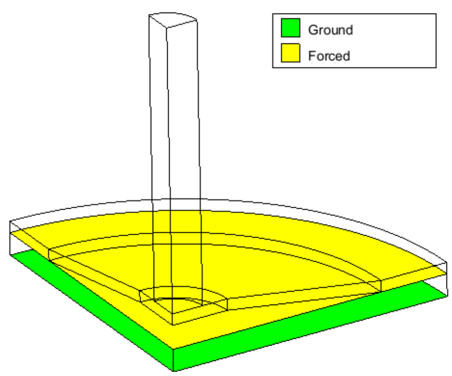

Figure 3.9. An example of the electrical potential surfaces on an individual cymbal. The symmetric mid-plane is grounded.

3.2.2.4 Radiating boundary

The radiating boundary described in Chapter 2 is used to allow for waves to propagate away from the transducer. Due to the 3-fold symmetry of the devices modeled, the radiating boundary is an eighth of a sphere. The radiating boundary for all in-water arrays was modeled at just under 12 benchmark diameters (ϕ). An example can be seen in Fig. 3.10.

The minimum distance of the water boundary was governed by the near-field effects of the transducer, as discussed in Chapter 2. The pressure field of the transducer can be visualized as a color plot in post-process. This allowed for a simple visual check that interference effects were completely within the water boundary and $^1/_r$ decay had begun. Additionally, the pressure vs. distance along the axis of operation was plotted for several different frequencies to verify this. An example of both checks will be presented in the results.

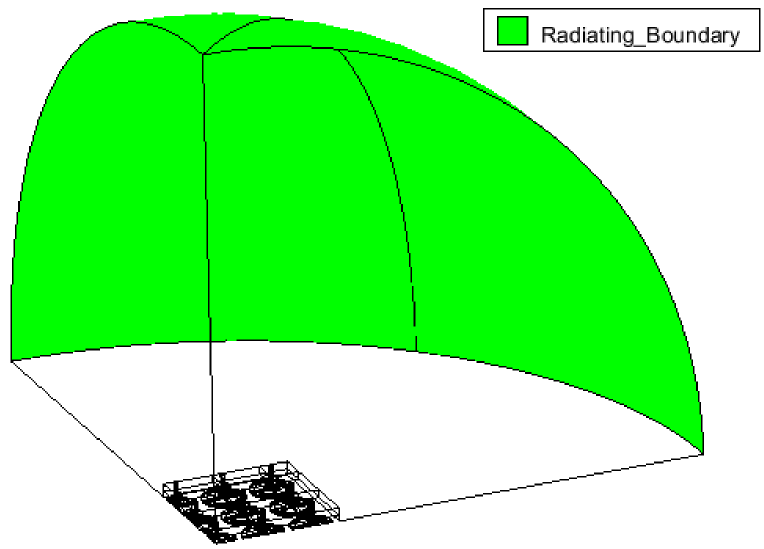

Figure 3.10. An example of the radiating boundary on an array.

3.2.2.5 Acoustic Center

In order to enforce the radiating boundary condition, ATILA requires an acoustic center. The user selects an acoustic center and then enters the distance of the radiating boundary. This allows for the model to check the quality of the radiating surface by comparing the measured distance with the user defined acoustic center distance. This is the reason that two surfaces were used to define the radiating boundary for the benchmark array, as seen in Fig. 3.10. One surface would not mesh within the tolerance required for the radiating condition, so it was split into two with a line down the center that anchored the surfaces.

For these models, the acoustic center was defined as a point at the origin, the center of all symmetry. It can be seen for the benchmark array in Fig. 3.11.

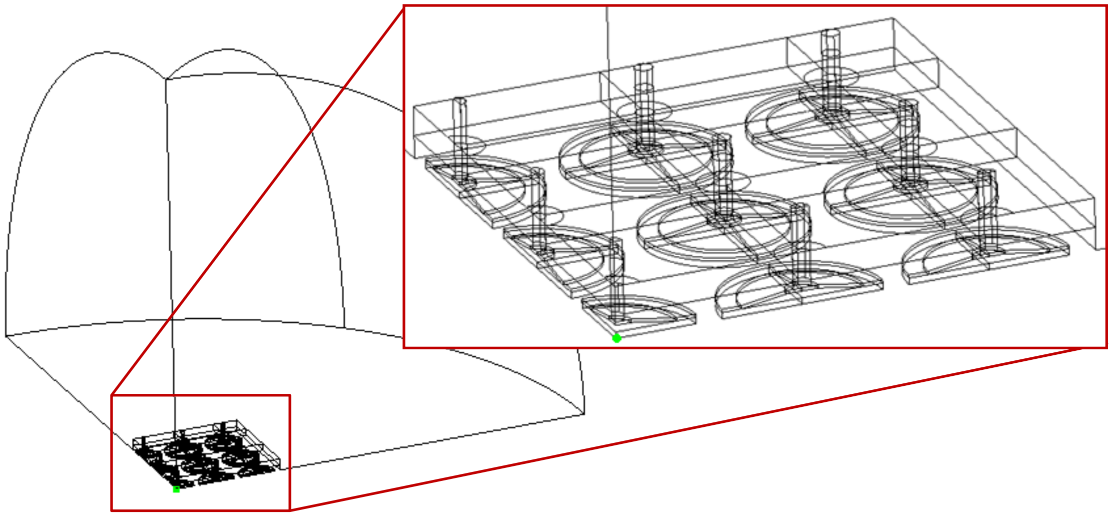

Figure 3.11. An example of the acoustic center for a radiating boundary.

3.2.2.6 Material properties

With a defined geometry and boundary conditions, the only thing that remains is definition of the volume material properties. Several standard materials are provided in ATILA. Of these, titanium and water were used for these models. The remaining materials needed to be defined as custom: [001] poled PMN-30PT, [011] poled PMN-29PT, a graphite/epoxy composite, and a high-density washer/nut/stud substitution material to be discussed in section 3.3.3.2. Custom materials were input through the GiD interface and then assigned to the model. The color-coded materials display of the benchmark array model can be seen in Fig. 3.12. Copies of the material data files for both the benchmark cymbal array and the prototype rectangular cymbal array are in Appendix A.

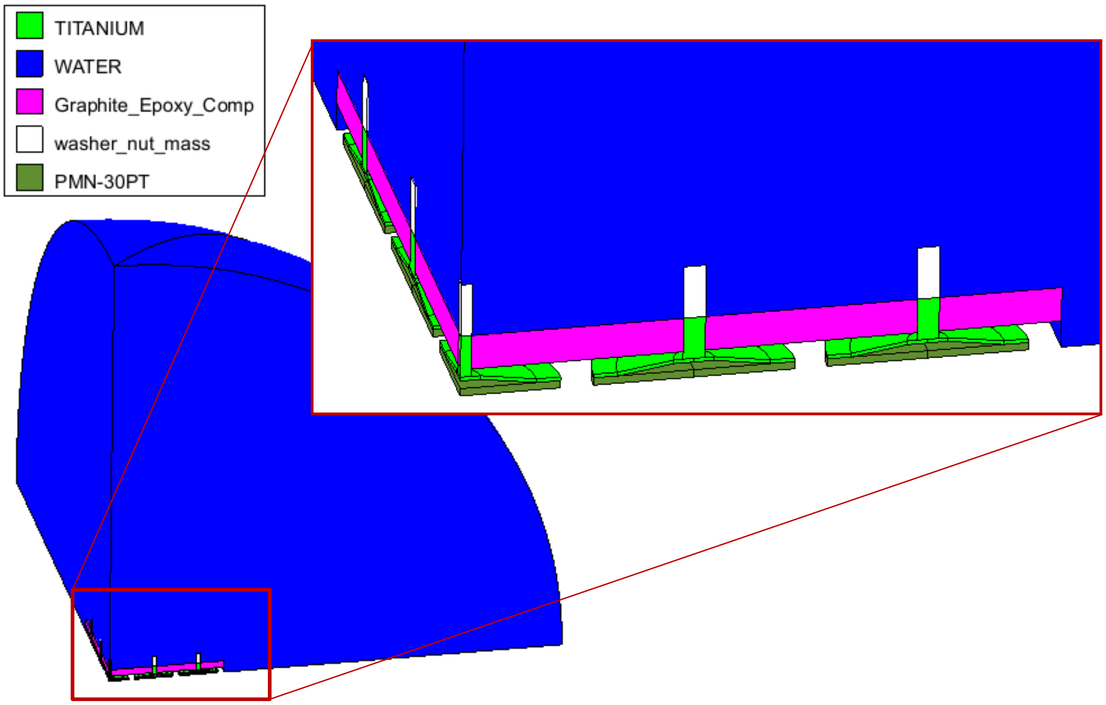

Figure 3.12. A color-coded display of benchmark array materials.

3.3 Defining the design space

The stated goal of this work is to create a design that allows for active material substitution and to conduct a variable study on that design to understand the impact of different transducer dimensions. In order to properly do this, a design space was defined.

The first consideration was that whatever model was decided upon, it must be able to accurately model the output of the benchmark cymbal array. Since the output of this array has been previously measured, then an agreement with the modeled results gave confidence in the model.

Secondly, the extent to which the new design can vary was defined. In order to provide a good A to B comparison of the transducers at the end of the modeling experiment, the following constraints were imposed:

1. The same crystal thickness was used for both the new design and the benchmark. This allowed for a fair comparison of TFR, knowing that the required drive voltage would not be significantly different between the two designs. The exception to this was a study of the rectangular cymbal crystal thickness (t_x). This was done to see how the output would scale with an increase of active material volume.

2. The same cover plate dimensions were used. The radiation resistance of the transducer (and therefore output power) at a given frequency is closely tied to the size of radiating face. By

requiring the size of the face not change, any improvement (or reduction) in the output can be properly attributed to the superiority (or inferiority) of the [011] poled material.

3. The same hardware (cover plate, washers, nuts, and studs) and hardware material properties were used.

It is of note that the overall thickness of the array is not a constraint on this list. This was eliminated after preliminary work showed that the stiffness of the individual cymbals has a strong influence on the output of the array. By allowing for the overall thickness of the array to increase, the open capped cymbals could be stiffened as necessary to improve performance. Increase over the benchmark array thickness is reported and discussed.

3.3.1 Cymbal size determination

With the design space defined, the ideal size for the rectangular cymbal within it needed to be determined. The rectangular nature of the design allows for great freedom in the number of cymbals that will fit under the panel, as their aspect ratio could vary substantially. The benchmark array has 25 circular cymbals in a 5 row $\times$ 5 column layout. Starting from this point, aspect ratios for 5, 4, and 3 rows of rectangular cymbals were tested to determine an appropriate baseline.

While the overall goal of this project was to increase output, there is also the practical goal of easing cymbal fabrication as much as possible. It was determined that if output wasn't significantly greater for a certain aspect ratio ($> 1\ dB$), then the ratio that reduced the total number of cymbals would be selected. This process, the results of which are detailed in Chapter 4, ultimately led to selection of a 4 row $\times$ 6 column matrix of rectangular cymbals.

3.3.2 Prototype rectangular cymbal

Taking the aspect ratio that the 4 cymbal $\times$ 6 cymbal array gives, an initial study of dimensional effects on output was undertaken. This led to the decision on the prototypical dimensions of the rectangular cymbal. These dimensions can be seen in Fig. 3.13 and their normalized values found in Table 3.4.

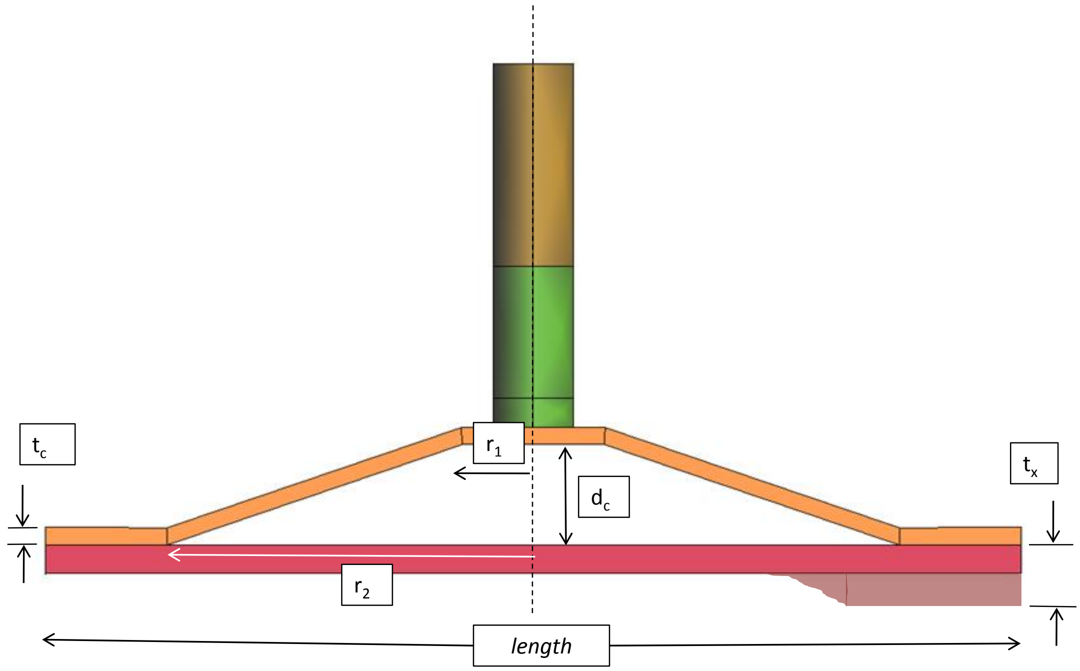

Figure 3.13. A half cross section of an individual prototype rectangular cymbal w/ normalized dimensions. There is symmetry about the mid-plane, as implied by the t_x dimension. The width of the cymbal is into the page and not shown.

$length$	1.340 ϕ
$width$	0.866 ϕ
d_c	0.098 ϕ
r_1	0.098 ϕ
r_2	0.500 ϕ
t_c	0.024 ϕ
t_x	0.079 ϕ

Table 3.4. Normalized dimensions for the rectangular cymbal in Fig. 3.13. All dimensions are normalized by the diameter of the benchmark cymbal in Fig. 3.1.

3.3.3 Model simplifications

In order to quickly iterate the designs, the models needed to solve as quickly as possible while maintaining an acceptable match to experimental results. This can be facilitated by making a number of concessions when designing the model.

3.3.3.1 Epoxy

The epoxy bonding layer between the cymbal cap and the single-crystal disk was not modeled. This was done to keep the required computational memory reasonable, as a thin epoxy layer would require finite elements at least an order of magnitude smaller than the other cymbal dimensions. While this type of element spreading is possible, it was not practical in the array models, as anything over 900,000 degrees of freedom required virtual memory to solve[3].

The result of not modeling the epoxy is that the model now has a stiff connection between the titanium cap and the active material. Normally the epoxy would add compliance and loss to the model in this joint. This stiff joint was conceded for three reasons. First, preliminary work showed that the epoxy did not significantly change the resonance frequency (i.e. the additional compliance was small). Secondly, the possibility of better loss modeling with the epoxy layer was outweighed by the fact that accurate loss data for other material properties was hard to obtain. Knowing that the loss would already be inaccurate due to other materials, the incremental gain in accuracy was deemed not to be worth the computational time. Finally, the dominant loss in the system was due to water loading. This can be seen when looking at the impedance in-vacuum versus in-water, which is presented in the results.

3.3.3.2 Nut, washer, & stud attachment

The joint attaching the stud to the cover plate is hard to model in ATILA. In reality there is a clamping of the cover plate in the thickness direction and a non-zero frictional force that would stiffen it in the transverse directions due to the interaction between the washers and the cover plate. Also, the stud is only in tension due to an axial force imposed by the nut, and there would only be minor interaction with the cover plate directly.

Early attempts at reconstructing this reality by modeling volumes for the washers and nut were met with questionable results. The joint appeared to stiffen the model more than it does in reality, increasing the resonance frequency of the array from what was expected. To alleviate this, the modeled volumes of the washers and nut were removed, and a more dense portion of the stud was put in their place. This mass substitution proved to be an acceptable model of known experimental results. The final model with this altered geometry is shown in Fig. 3.6, with the substitution material shown in brown. Since this mass was added to an existing portion of the titanium stud, the stiffness was not changed from the value for titanium.

3.3.3.3 Ramp thickness correction

The ramp of the cymbal is the material that connects the apex of the cymbal, the flat area on top, to the flange of the cymbal, the area where it is epoxied to the active material. There are many ways that this geometry could have been constructed in GiD, but it was determined that the easiest for quick iteration was to first model the correct thickness of apex and flange, and then to connect their edges directly and create a volume from these connections. This method is inherently flawed if no correction is made for the angle of the ramp (α), as can be seen in Fig. 3.14. No correction would need to be made at an angle of zero, but in the extreme case of an angle of 90^o the thickness would go to zero. Therefore, an angle based correction needed to be

[3] Anyone who has attempted to use virtual memory to solve a problem numerically has experienced the painful order of magnitude increase in solution time.

made based off of the dimensions of the cymbal.

Using the dimensions of Fig. 3.13, the following relationships can be drawn:

$$\alpha = tan^{-1}\left(\frac{d_c}{r_2 - r_1}\right)$$

$$\text{correction} = t_c\left(\frac{1 - cos(\alpha)}{sin(\alpha)}\right)$$

Where the correction is the horizontal distance between the points that define the boundaries of the apex and flange, which is shown in Fig. 3.15, and α is the angle of the ramp. This allowed for simple modeling, while maintaining the thickness of the ramp within 1% of the desired material thickness.

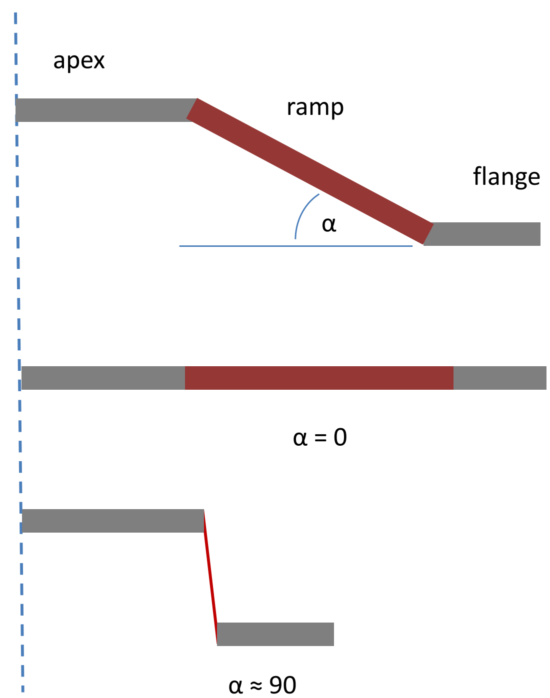

Figure 3.14. Extremes of direct connection ramp modeling. The terminology and angle are shown (top), followed by the low angle extreme (middle) and high angle extreme (bottom).

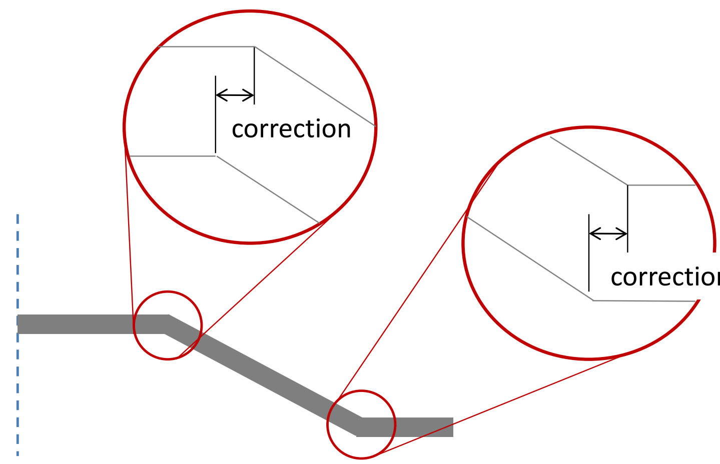

Figure 3.15. Ramp thickness correction for the apex and flange.

3.3.3.4 Potting

Underwater transducers are often potted in a flexible material such as polyurethane before being mounted to a larger structure. This serves the purpose of waterproofing the assembly, as well as decoupling the vibrations of the transducer from the structure. Additionally, the potting material can be used to create a better impedance match between the transducer and water, which allows for better power transfer between the two.

In the case of the transducers modeled, this potting layer was left out. The water volume defined in the model allows for propagation of acoustic waves, but does not flow, making waterproofing unnecessary. Mounting constraints are unnecessary as well, because the displacement symmetry conditions allow for free-field analysis of the transducer.

The assumption in leaving this layer out is that any improvement or reduction in performance would be comparable for the [001] poled crystal benchmark design and the [011] poled crystal rectangular cymbal arrays because they share the same cover plate material and geometry.

3.4 Variable study

Once the model had been designed, the benchmark [001] poled crystal array verified, and a prototype rectangular cymbal designed, the complete variable study could be performed. The variables studied are shown in Fig. 3.13 (d_c, r_1, r_2, t_c, and t_x). The cymbal length and width were not varied. An array of 4 cymbals $\times$ 6 cymbals was laid out for various changes in each of these dimensions off of the prototypical dimensions laid out in Table 3.4. As stated above, the same hardware and cover plate designs were used. Additionally, the same water boundary was used for these models and the benchmark array.

Because the relative strength of each variable wasn't known before beginning the study, guesses needed to be made for how much each should be varied. As such, there are large differences in the extent to which each dimension was varied. The motivating goal was to determine the variable strength with regards to output and coupling, while still keeping the array response in a similar region to the benchmark array.

3.4.1 TFR and $TVAR$ normalization

Using the magnitude pressure output, and the equations defined in Chapter 2, the TFR and $TVAR$ for each array were calculated. These numbers were then normalized to the TFR and $TVAR$ of the [001] poled PMN-30PT benchmark array at its first electrical resonance frequency. This means that the output of the benchmark array at f_r is reported as 0 dB for both, and all frequency response is shown relative to these baselines.

3.4.2 Effective coupling calculation

The distribution of frequencies was determined from the modal behavior of the structure, but was limited by output file size. Truly accurate values for the coupling would require increased frequency resolution in the neighborhood of electrical resonance and antiresonance. This was done for initial comparisons of the [001] poled benchmark array and the [011] poled prototype array so that their relationship was well-defined.

For the variable study models, the frequency spacing ended up larger because the models were not run twice to increase resolution in these areas. In order to calculate the effective coupling, the resonance and antiresonance peaks were determined by using a quadratic fit of the three points closest to the minima or maxima near resonance. This method was deemed accurate enough to predict trends in coupling response for each variable studied.

Chapter 4

Results

4.1 Individual cymbal

4.1.1 Benchmark cymbal

The benchmark cymbal model detailed in Chapter 3 is shown Fig. 4.1. It can be seen that the model is one eighth symmetry.

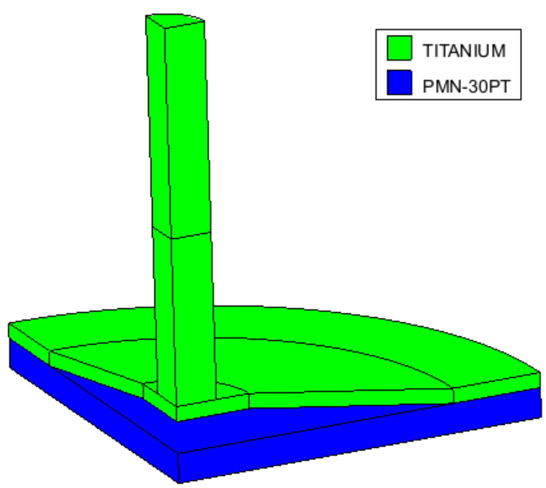

Figure 4.1. Individual benchmark cymbal model. The view mode in GiD is material colors.

4.1.1.1 Convergence study

To determine if the predicted mesh size was appropriate, a convergence study testing various sizes was performed. A normalized plot of displacement versus frequency in-air is shown below in Fig. 4.2. In the legend the mesh size, the automatic mesh element lengths normalized to the benchmark cymbal diameter (ϕ), and the number of degrees of freedom (D.O.F.) for each model are listed.

A view of all 5 models in the neighborhood of resonance is shown in Fig. 4.3. It can be seen that all frequencies are normalized to the f_r of the 0.8 ϕ mesh cymbal[1]. Also, it is noted that both displacement and resonance frequency do not change drastically with significant increase in mesh density. From approximately 5000 D.O.F. to over 100,000 D.O.F. there is a reduction in resonance frequency of less than 7% and a increase in displacement of less than 2%. For this reason, the 0.8 ϕ mesh was determined to be sufficient for modeling the cymbal.

Finally, it can be seen that the automatic meshing in GiD can use elements smaller than the user input mesh length. This is seen in the fact that the 0.4 ϕ mesh produced the same number of D.O.F. as the 0.8 ϕ mesh did.

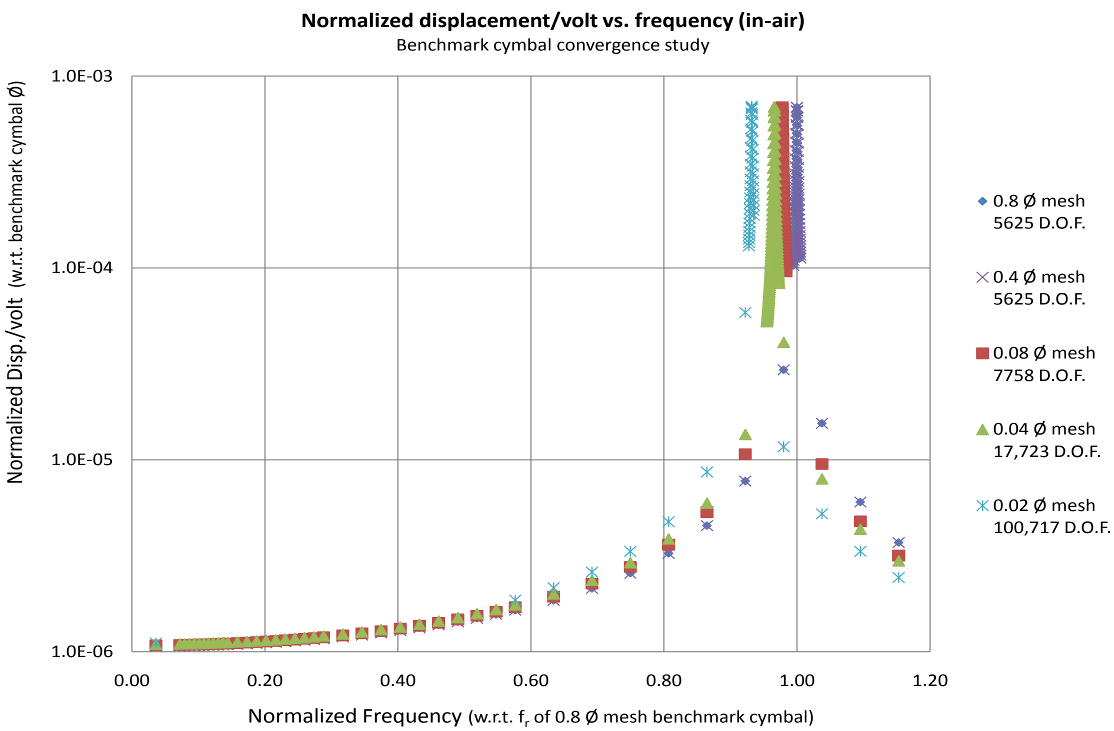

Figure 4.2. Benchmark cymbal convergence study: displacement vs. frequency

[1]For the individual cymbals, the frequency of minimum electrical impedance (f_r) matched up with the frequency of maximum displacement (f_s). This is attributed to the fact that individual cymbals are low-loss transducers. This was not necessarily true of array models, where f_r differed noticeably from the frequency of maximum output, due to the additional system losses.

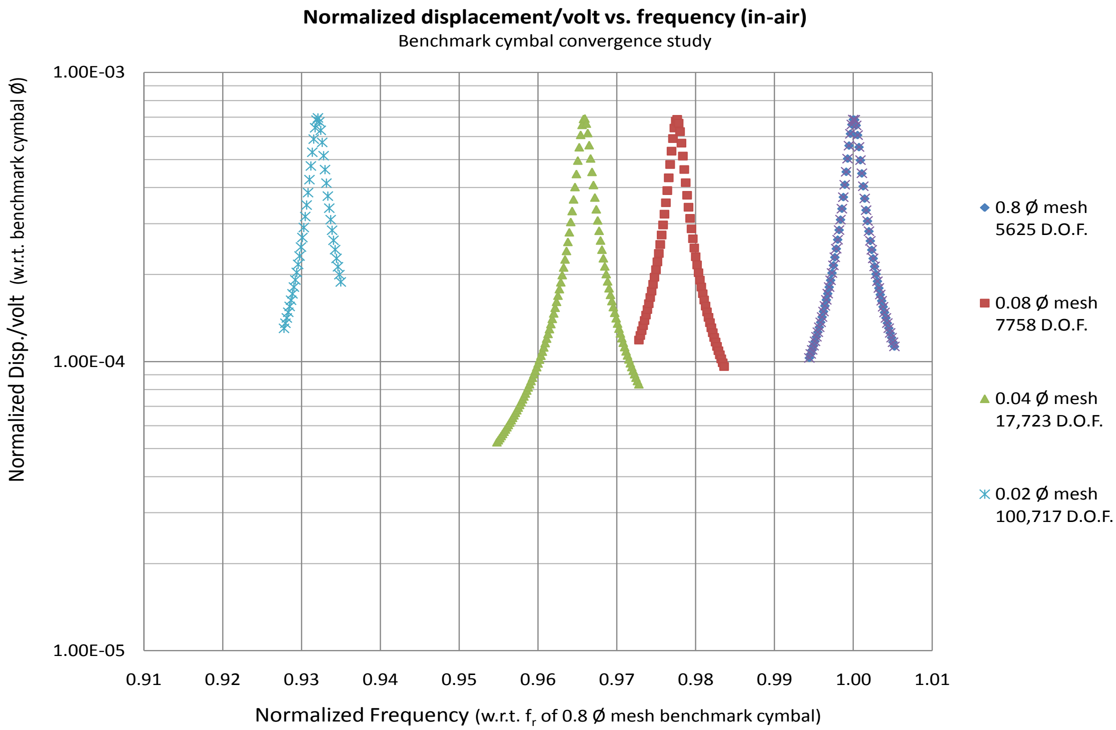

Figure 4.3. Benchmark cymbal convergence study: displacement vs. frequency

4.1.1.2 Displacement

A zoomed-in view of the normalized plot of displacement versus frequency in-air can be seen in Fig. 4.4. This shows the envelope of the displacement spectrum is well-defined, and that there is sufficient frequency resolution to accurately define the maximum displacement.

This displacement curve is not meant to be representative of a real cymbal transducer. Without the epoxy losses, the model is significantly more resonant than an actual cymbal would be. This is detailed further in Appendix B, where experimental measurements of cymbals are presented and compared to the model. The purpose of presenting a more resonant displacement spectrum here is for comparison to the individual rectangular cymbal.

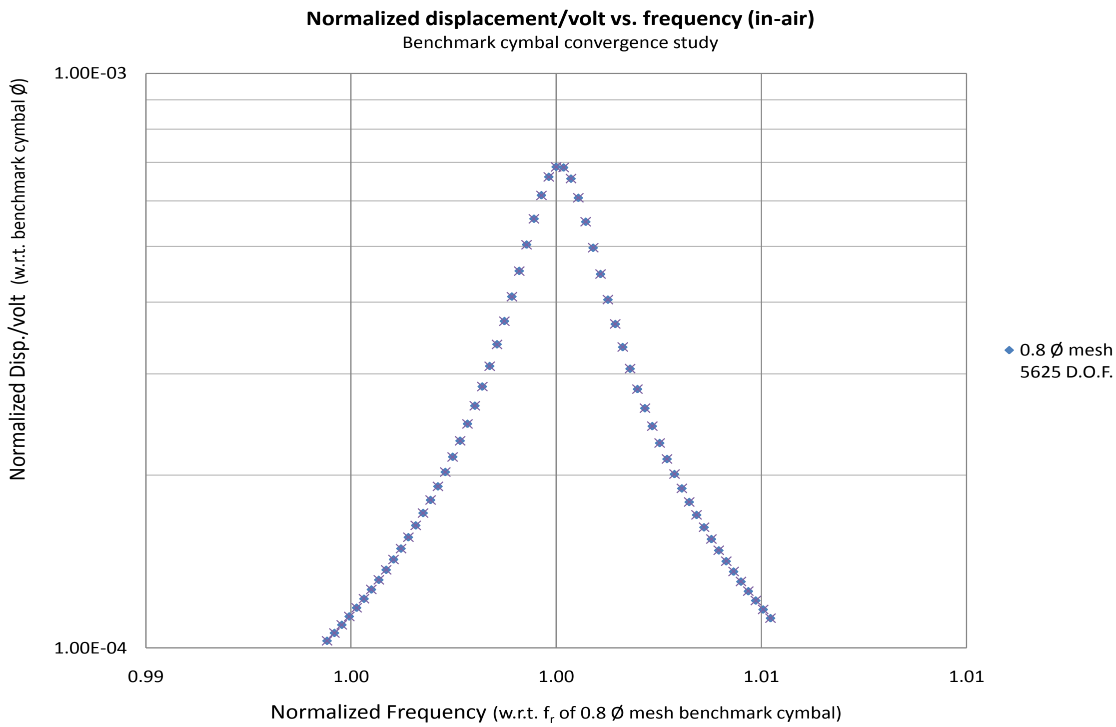

Figure 4.4. Benchmark cymbal: displacement vs. frequency

4.1.1.3 $|Z_E|$ & κ_{eff}

The normalized in-air impedance spectrum of the benchmark cymbal is shown in Fig. 4.5. Both smoothed and un-smoothed meshes are shown, and both are normalized by the magnitude impedance ($|Z_E|$) of the smoothed mesh at f_r. This shows that as the convergence study predicts, that different meshes can have slightly different resonance frequencies. In this case the difference was approximately 5%. For this reason, it was made sure that all models were smoothed prior to solution, so that a consistent process of generating the mesh was used. This was done in hopes of removing the variability of differences between a smoothed and an un-smoothed mesh.

A mesh is smoothed to reduce the aspect ratio of the mesh elements. High aspect ratio elements can cause issues in the matrix calculation, so the program identifies these areas and reconstructs the mesh to create more robust elements. The specifics of this high-aspect ratio element problem are left for texts on FEA theory.

Once the impedance curves were obtained, the effective coupling (κ_{eff}) could be calculated. The increased frequency resolution at the resonance and antiresonance is shown in Fig. 4.6. This was done to allow for reduced error in calculation of κ_{eff}. Both the smoothed and un-smoothed mesh cymbals had a value of $\kappa_{eff} = 0.38$.

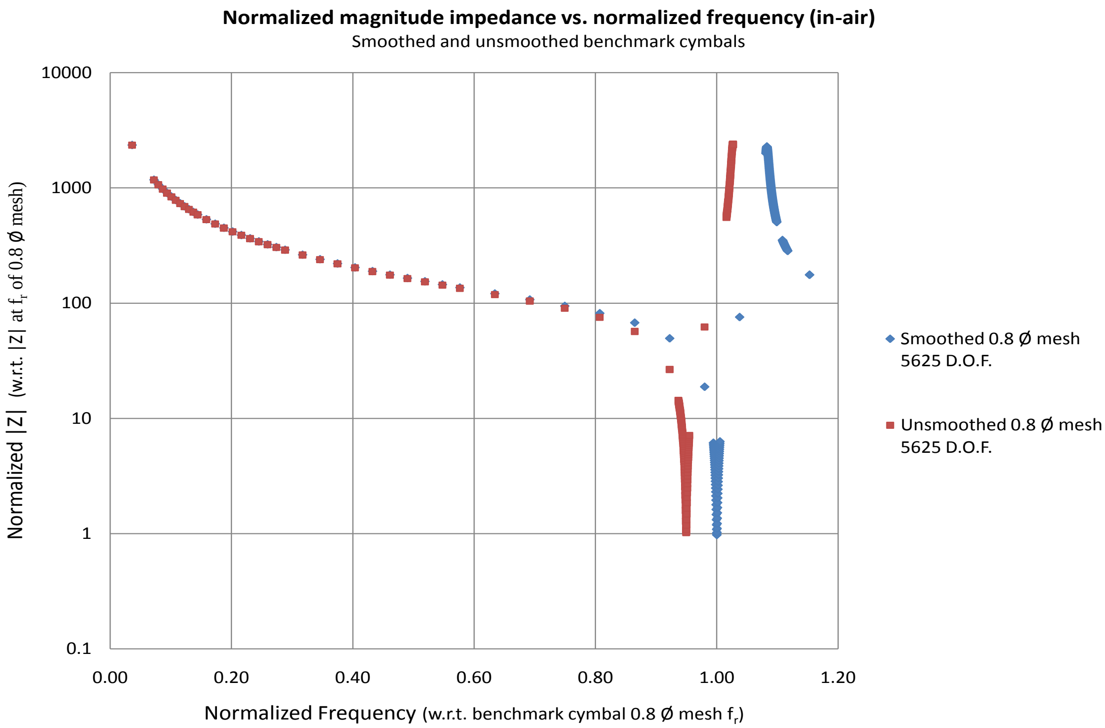

Figure 4.5. A spectrum of smoothed and un-smoothed mesh benchmark cymbals.

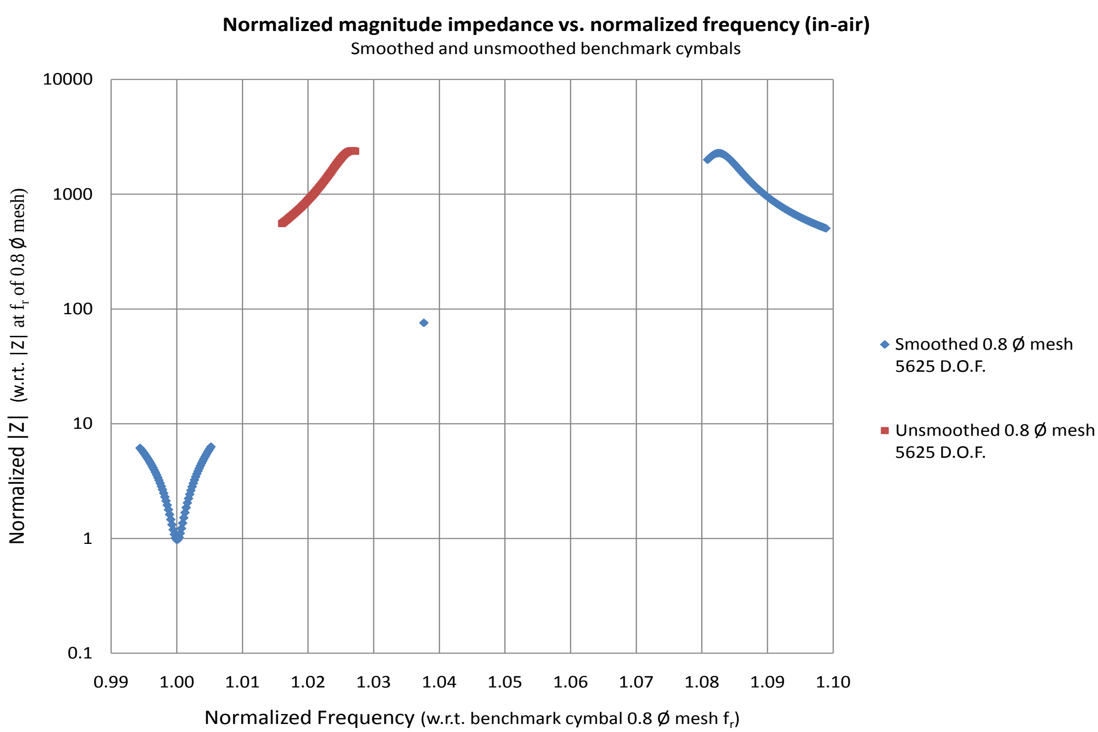

Figure 4.6. A closer view of impedance vs. frequency for the smoothed mesh benchmark cymbal.

4.1.2 Prototype rectangular cymbal

The prototype rectangular cymbal model is shown below in Fig. 4.7. It can be seen that instead of an eighth model, it is a half symmetry model through the thickness direction. For this reason the impedance was corrected by a factor of 2 instead of $^1/_2$ as laid out in Chapter 3.

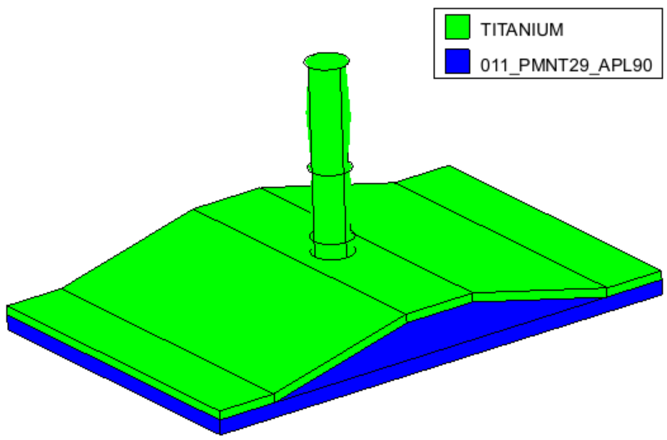

Figure 4.7. Individual prototype rectangular cymbal model. The view mode in GiD is material colors.

4.1.2.1 Convergence study

A convergence study similar to Section 4.1.1.1 was performed due to the new, more compliant, [011] poled PMN-29PT. A normalized plot of displacement versus frequency in-air can be seen in Fig. 4.8. The displacement and mesh size are normalized by the benchmark (circular) cymbal diameter, and the frequency is normalized by the benchmark cymbal f_r.

The zoomed-in view of Fig. 4.9 shows results similar to the benchmark cymbal convergence study. From 17,000 D.O.F. to 68,000 D.O.F. the resonance frequency drops by less than 4% and the displacement increases by less than 2%. Again, the 0.8 ϕ mesh criteria was decided to be sufficient for this model.

4.1.2.2 Displacement

The normalized displacement in-air of the prototype rectangular cymbal can be seen in Fig. 4.9. Its resonance frequency and displacement are compared to the benchmark cymbal in Table 4.1.

Design	Normalized displacement	Normalized f_r
Benchmark cymbal	6.88×10^{-4}	1.00
Prototype rectangular cymbal	4.34×10^{-4}	0.51

Table 4.1. Benchmark and prototype rectangular individual cymbal displacement comparison.

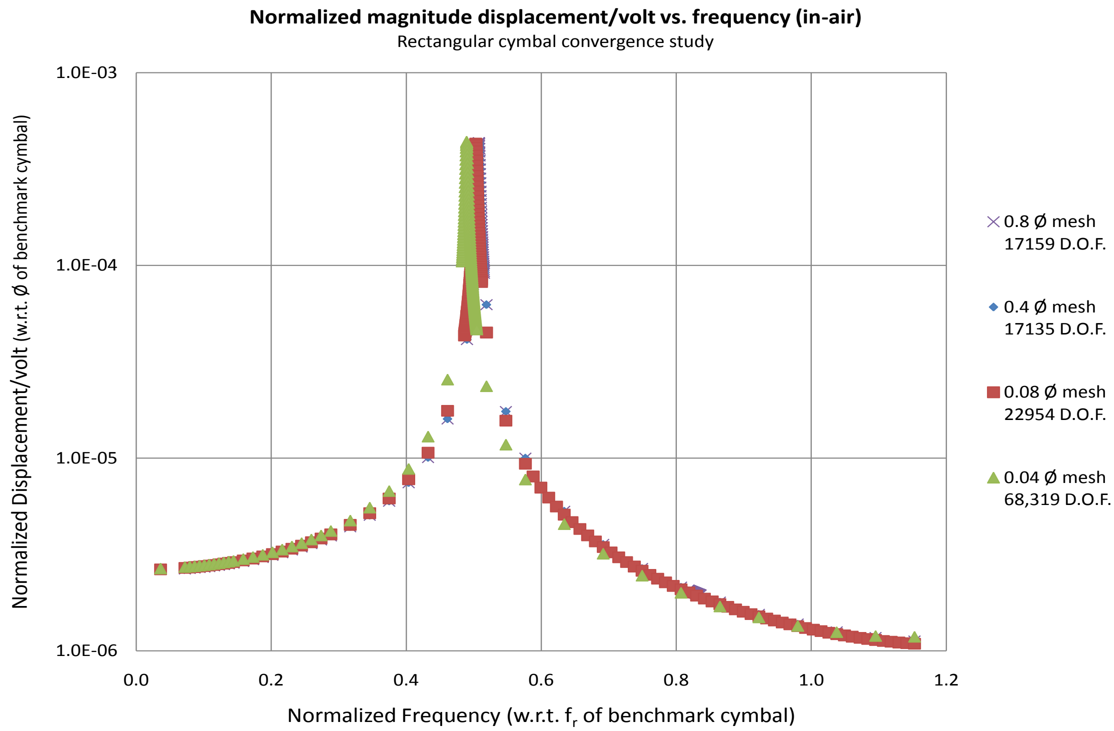

Figure 4.8. Rectangular prototype cymbal: displacement vs. frequency

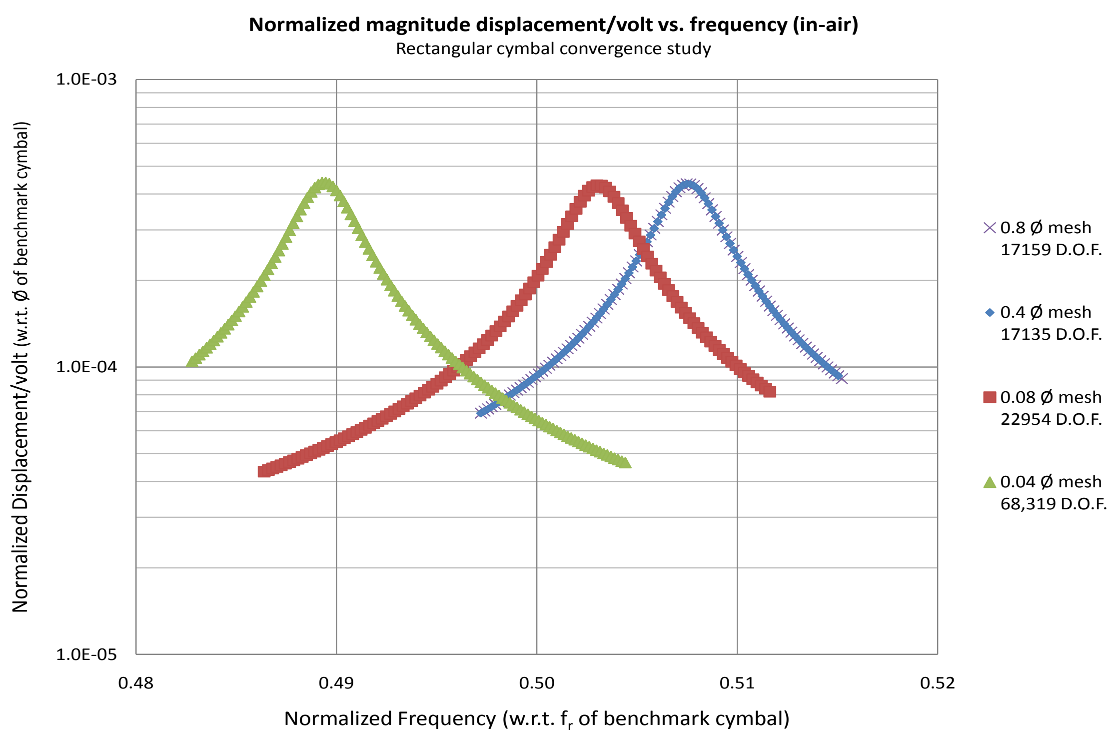

Figure 4.9. Rectangular prototype cymbal: displacement vs. frequency

4.1.2.3 $|Z_E|$ & κ_{eff}

The in-air impedance spectrum of the prototype rectangular cymbal is shown in Fig. 4.10. Again, the frequency resolution was increased near f_r and f_a. From this, κ_{eff} was calculated and then compared to the benchmark cymbal in Table 4.9.

Design	κ_{eff}
Benchmark cymbal	0.38
Prototype rectangular cymbal	0.79

Table 4.2. Benchmark and prototype rectangular individual cymbal κ_{eff} comparison.

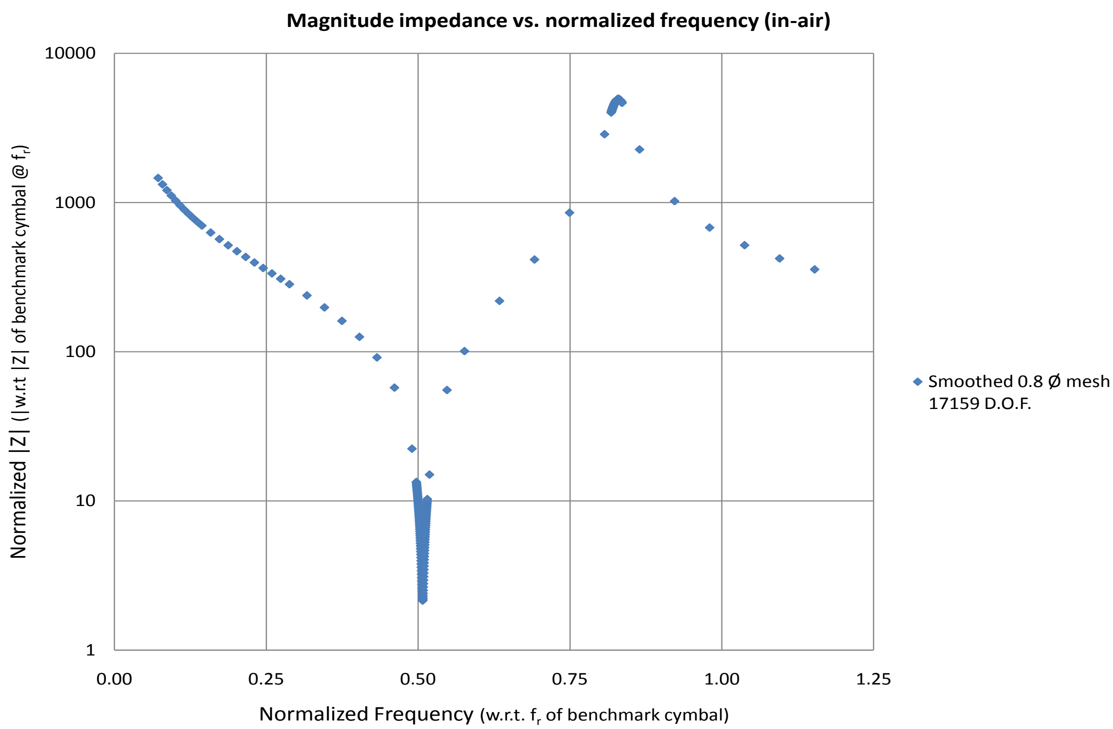

Figure 4.10. Impedance spectrum of the rectangular prototype cymbal.

4.1.2.4 Cap depth (d_c) effects

To better study the relationship between individual cymbal trends and array trends, a variable study was performed on cap depth effects in the rectangular benchmark cymbal. A normalized plot of displacement versus frequency in-air for several different cap depths can be seen in Fig. 4.11. Cap depth is varied off of the prototypical dimension. It is interesting to note another mode of the transducer that can be seen in lower depth models at higher frequency. This will be discussed in the next chapter.

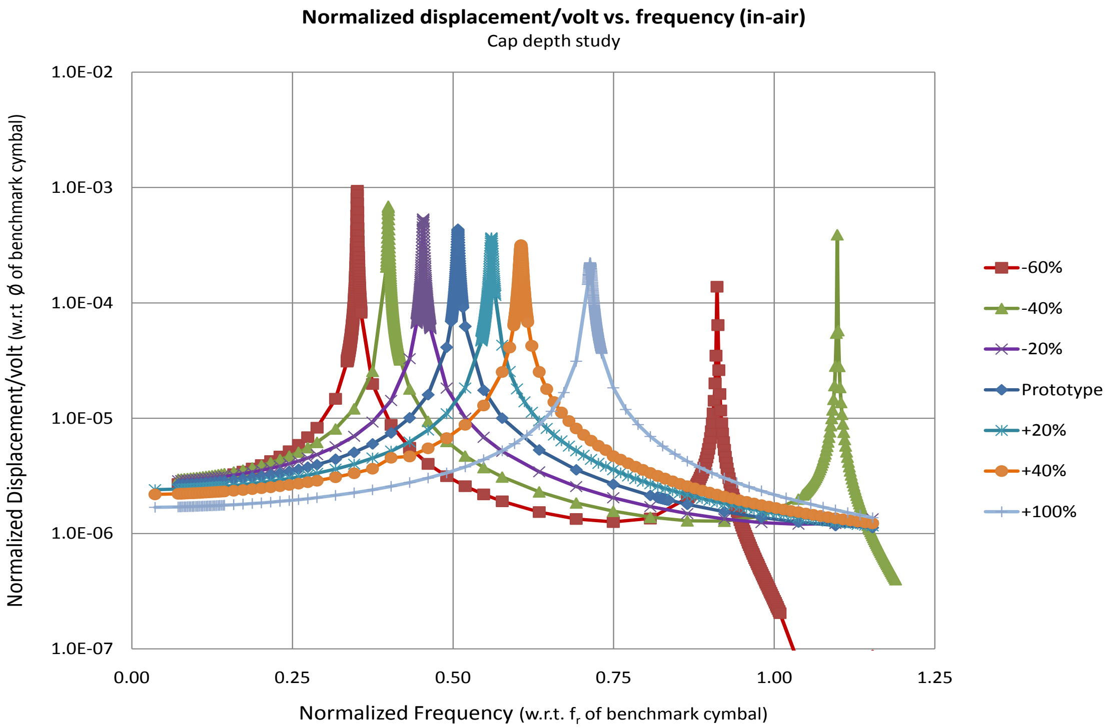

Figure 4.11. Displacement spectrum for several different values of d_c

4.2 Arrays

The array results are presented below. Unless otherwise specified, all models used a mesh criteria of 0.6 ϕ. This was done for two reasons. Most importantly, this number falls under the value of 0.8 ϕ determined in the convergence study below. Secondarily, it allowed for a good balance of spatial resolution (better than 0.8 ϕ) with reasonable solution time (quicker than 0.4 ϕ).

4.2.1 Benchmark Array

The [001] poled PMN-30PT cymbal array (benchmark array) model is shown below in Fig. 4.12. It was constructed as a one eighth model using the individual benchmark cymbal as a building block.

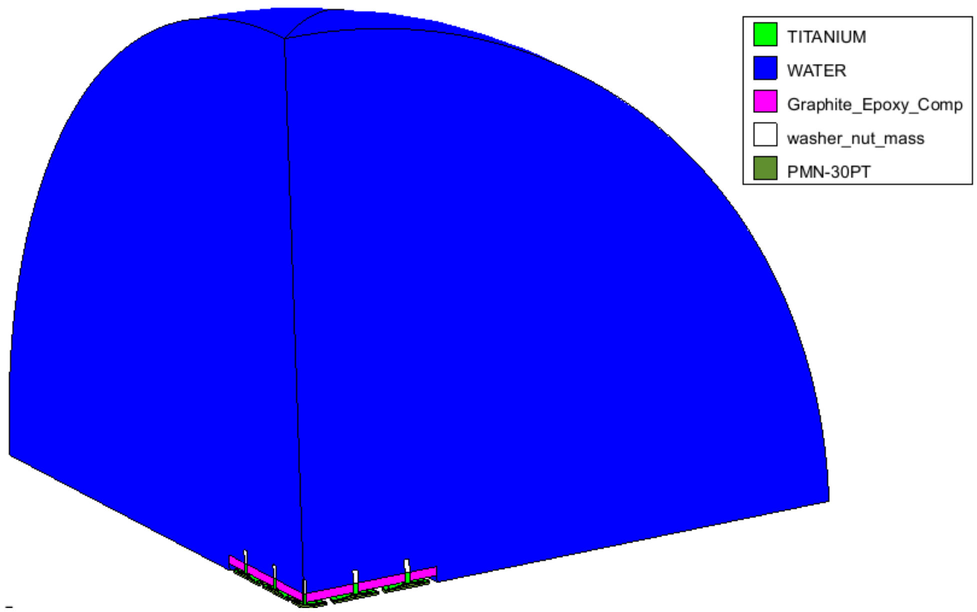

Figure 4.12. The benchmark array model. The view mode in GiD is material colors.

4.2.1.1 Convergence study

To determine that the mesh criteria of 0.8 ϕ was appropriate for the array model, a convergence study was performed. Magnitude pressure and frequency data were obtained at the on-axis extreme of the water boundary and used to calculate TFR. This was then normalized by the electrical resonance (f_r) value of TFR for the 0.8 ϕ mesh. A normalized plot of TFR versus frequency can be seen in Fig. 4.13.

Looking at the results of the convergence study, it was decided that 0.8 ϕ mesh was sufficient. There was little variation in the TFR curve even at the highest frequencies, and no perceptible shift in resonance frequency.

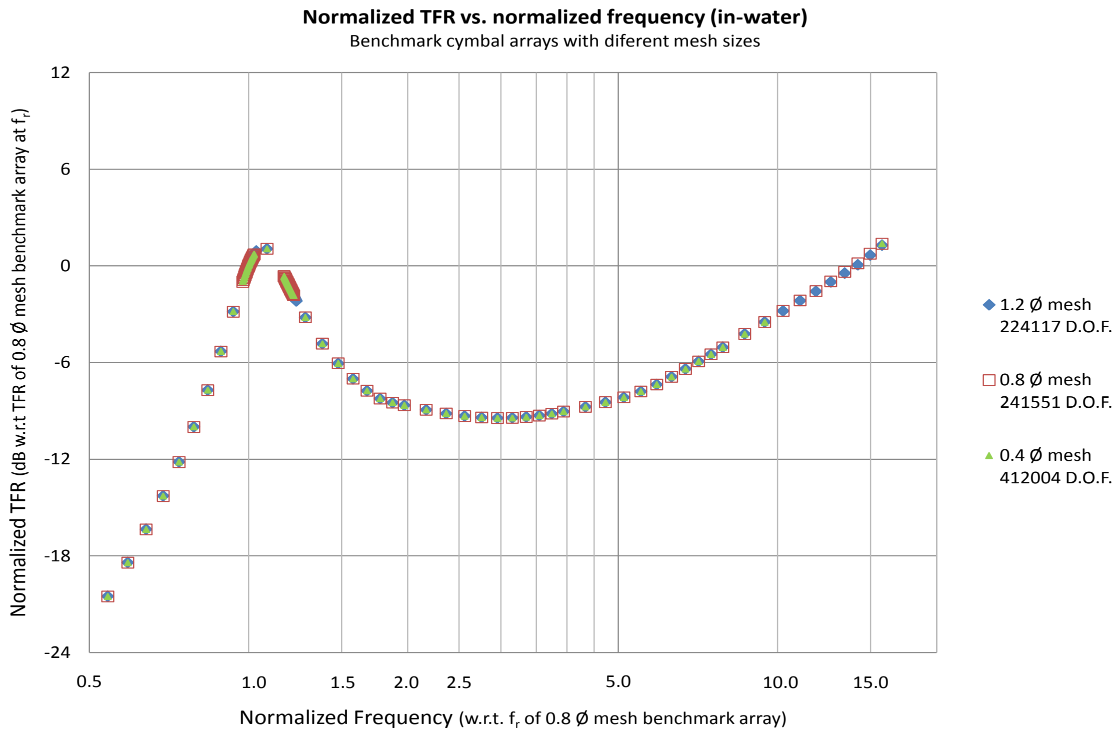

Figure 4.13. Benchmark array TFR vs. frequency for different mesh sizes.

4.2.1.2 TFR & $TVAR$

The TFR versus frequency for a 0.6 ϕ mesh benchmark array is shown in Fig. 4.14, and the $TVAR$ versus frequency is shown in Fig. 4.15. Note that these curves are shown in black, as they will be reference curves on all future plots of TFR and $TVAR$. TFR is normalized as in the convergence study, and the frequency by the fundamental electrical resonance frequency, f_r.

It can be seen that there is an expected bump in output at f_r, followed by a flat region. Finally, at higher frequencies, the curve trends higher for two reasons. The first is the increased directionality of the array at higher values of ka, and the second is that there will be another resonance peak further out for the (0,2) mode of the cymbal cap[2] which contributes in this band.

[2]The (0,2) mode terminology is referring to displacement node lines. For a circular cymbal cap, the first mode will be (0,1) which means there are no azimuthal nodes (i.e. the displacement doesn't depend upon angle) and 1 circular node in the radial direction flange of the cap. The (0,2) mode would then have an additional circular node line.

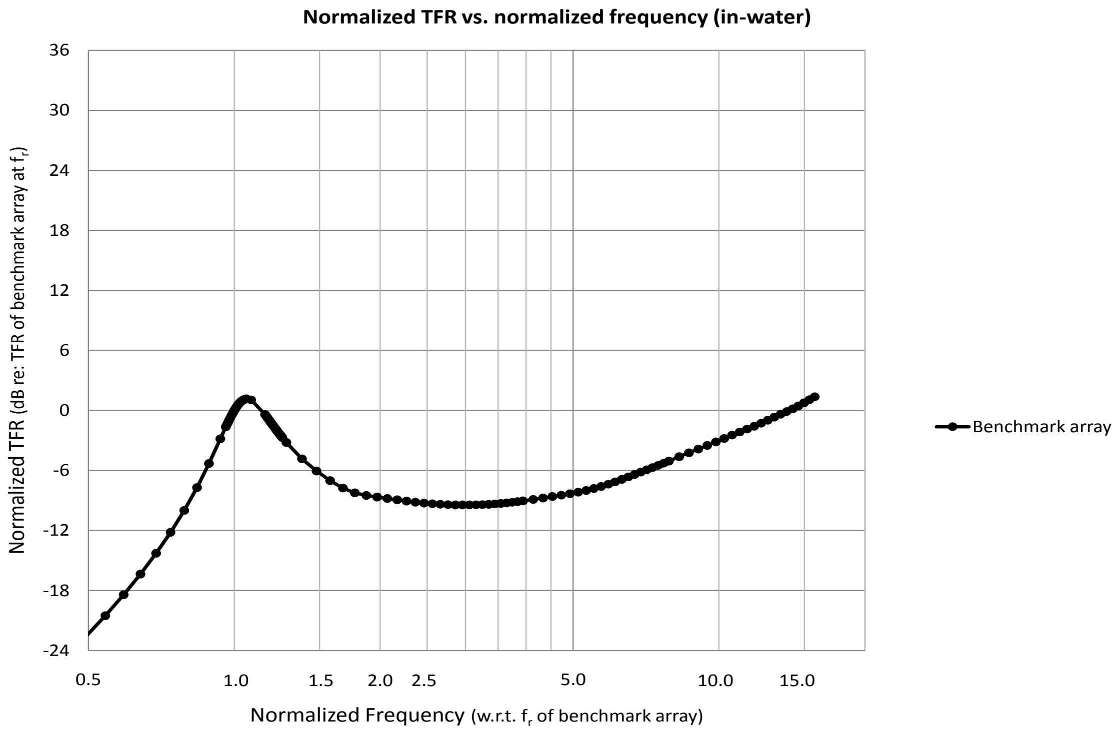

Figure 4.14. TFR vs. frequency for 0.6 ϕ mesh benchmark array.

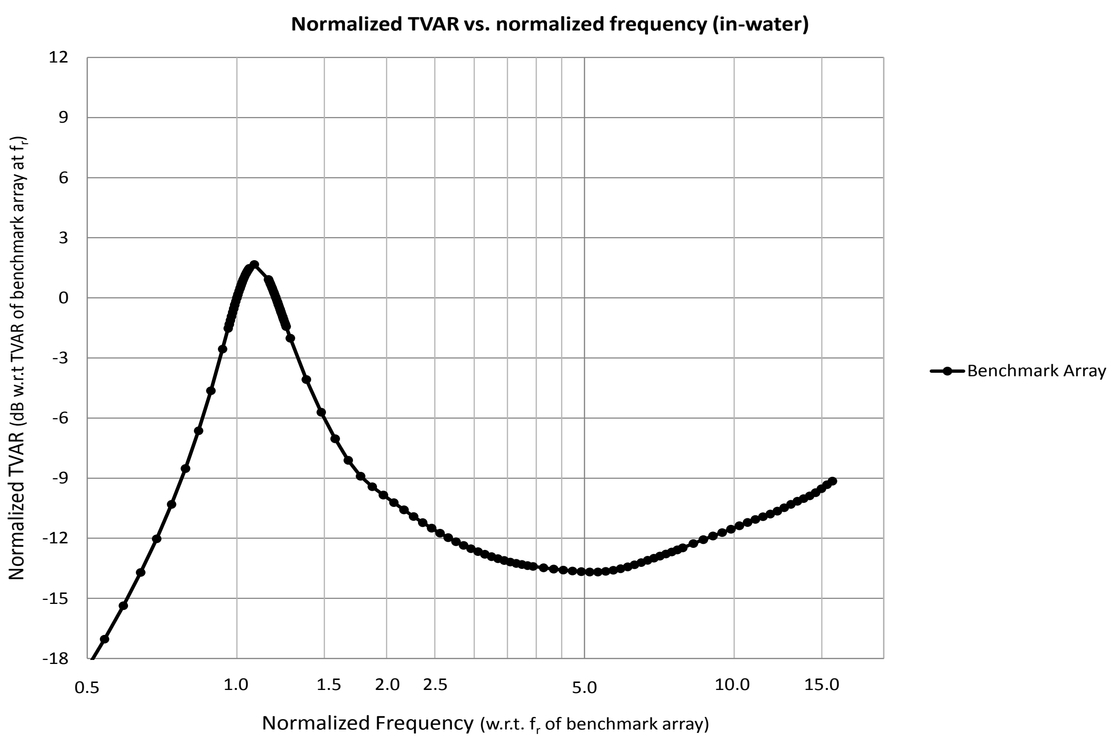

Figure 4.15. $TVAR$ vs. frequency for 0.6 ϕ mesh benchmark array.

4.2.1.3 $|Z_E|$ & κ_{eff}

A normalized plot of magnitude electrical impedance versus frequency for the benchmark array is seen in Fig. 4.16. The impedance is normalized by the magnitude impedance at its fundamental resonance frequency (i.e. $|Z_E|$ at f_r). Like the previous two benchmark plots, the curve is in black as a reference for future impedance plots. From this curve, κ_{eff} was calculated to be 0.55.

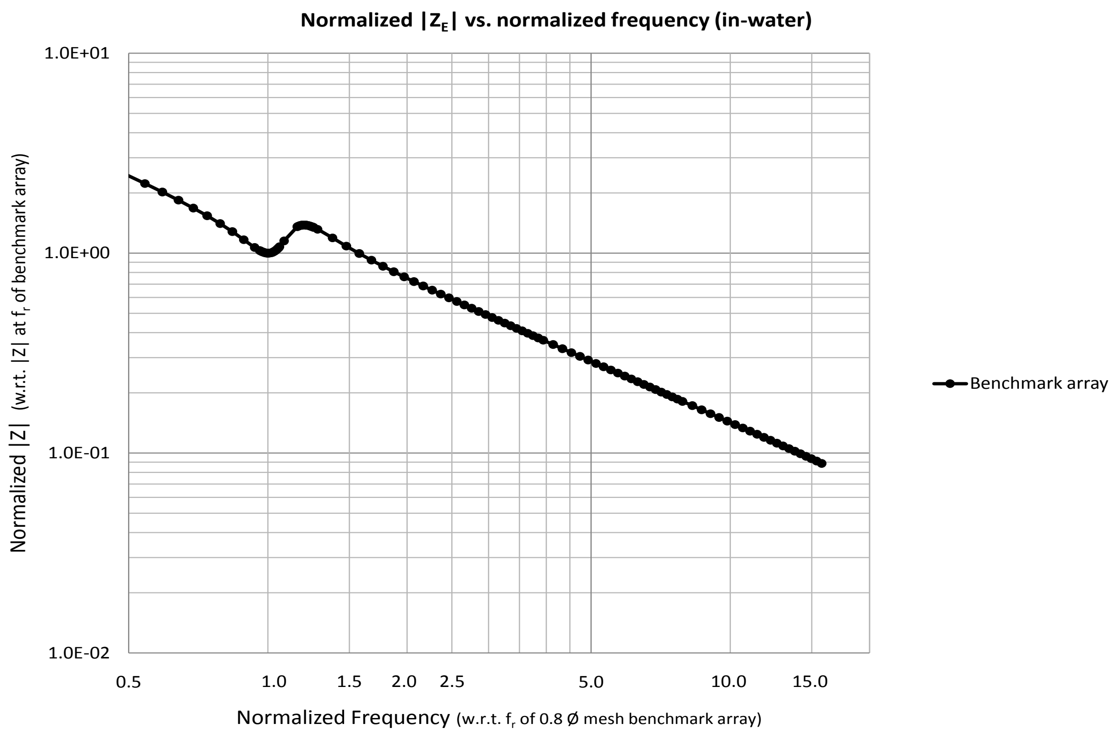

Figure 4.16. $|Z_E|$ vs. frequency for 0.6 ϕ mesh benchmark array.

4.2.1.4 In-water vs. in-air $|Z_E|$

In order to understand the influence of the water loading on the array, the impedance of the benchmark array was modeled both in-water and in-air [3]. This can be seen in Fig. 4.17. The sharp dip in the impedance at f_r and peak at f_a are indicative of a highly resonant system. The mass-loading effect of the water can be seen by the drop in resonance frequency. The increased loss (the acoustic load) is seen in the smoothing-over of the minimum and maximum impedance for the fundamental mode.

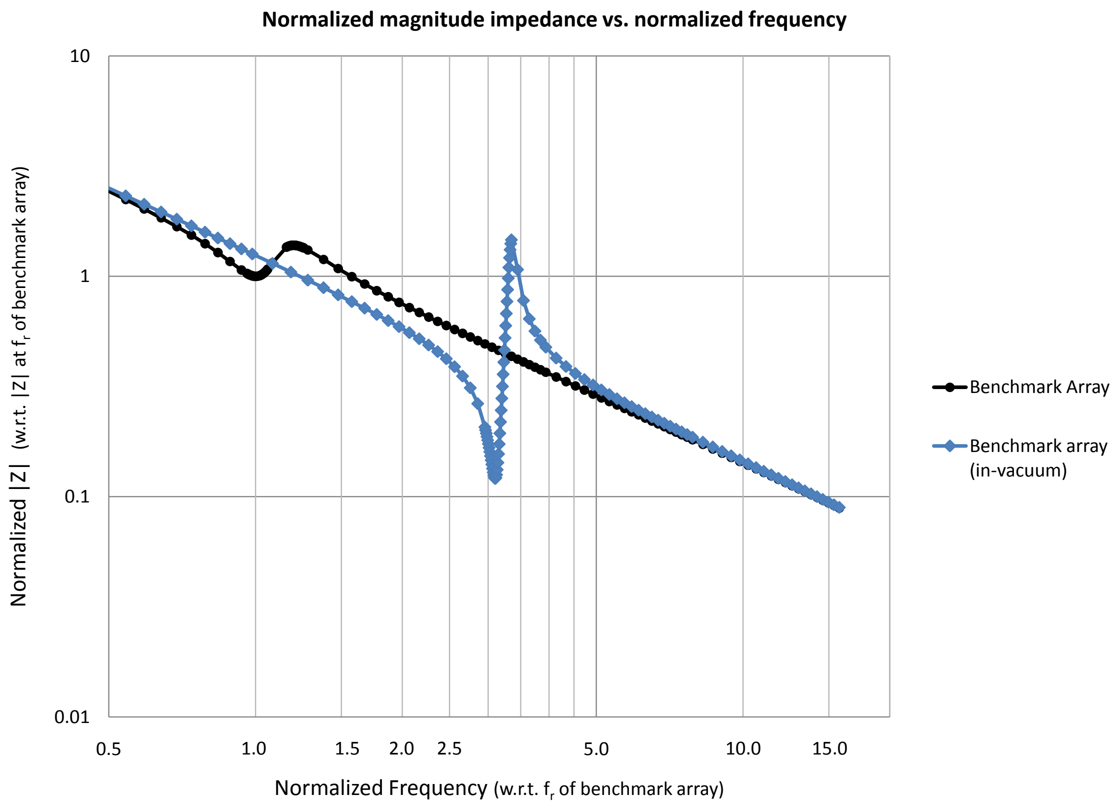

Figure 4.17. $|Z_E|$ vs. frequency for the benchmark array both in-water and in-vacuum.

[3]Technically, the model is predicting performance in a vacuum, as there is no fluid loading at all. Air-loading was assumed to be negligible so that in-air and in-vacuum are equivalent

4.2.1.5 Water boundary study

The water boundary study described in Chapter 3 was performed using the 0.4 ϕ mesh benchmark array, because it was the data set with the best spatial distribution for pressure. The color plot results are shown in Fig. 4.18, with dark red representing the maximum pressure and dark blue the minimum. The progression up in frequency shows a clear change in both directionality and the near field effects of the transducer. It appears from this plot that the water boundary is sufficiently far, but this will be clearer when looking at pressure versus distance along the axis.

Pressure versus distance on-axis was output at several frequencies, and is shown in Fig. 4.19. The ka value of the transducer is estimated for each frequency. Because the transducer is a square, half of the diagonal was used as the radius a. It appears from the plot below that the water boundary is sufficient, and $^1/_r$ decay is a good approximation for pressure data taken at water boundary.

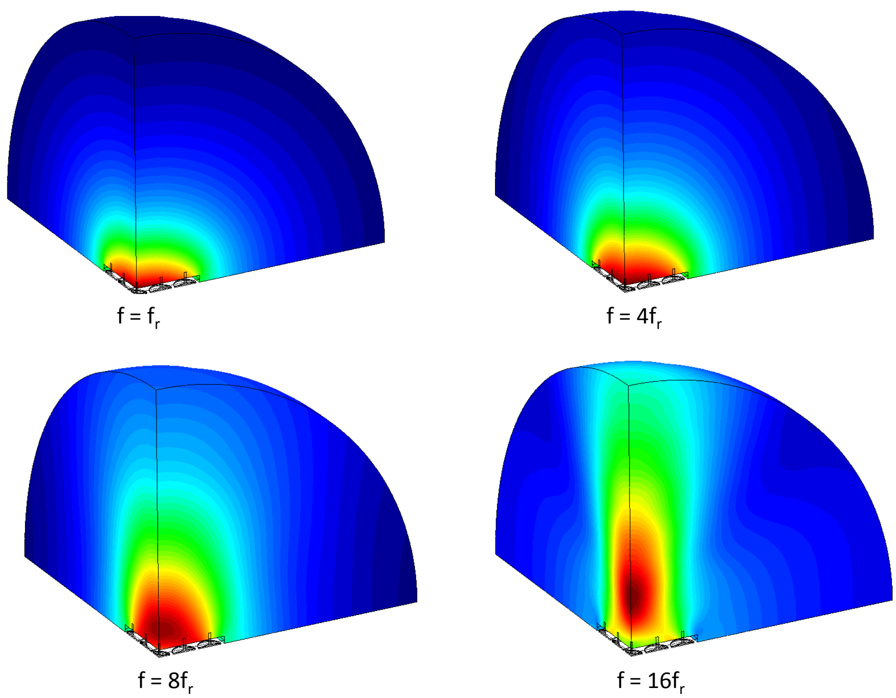

Figure 4.18. $|P|$ field color plot of benchmark array at several frequencies. Dark red represents the highest pressure and dark blue the lowest.

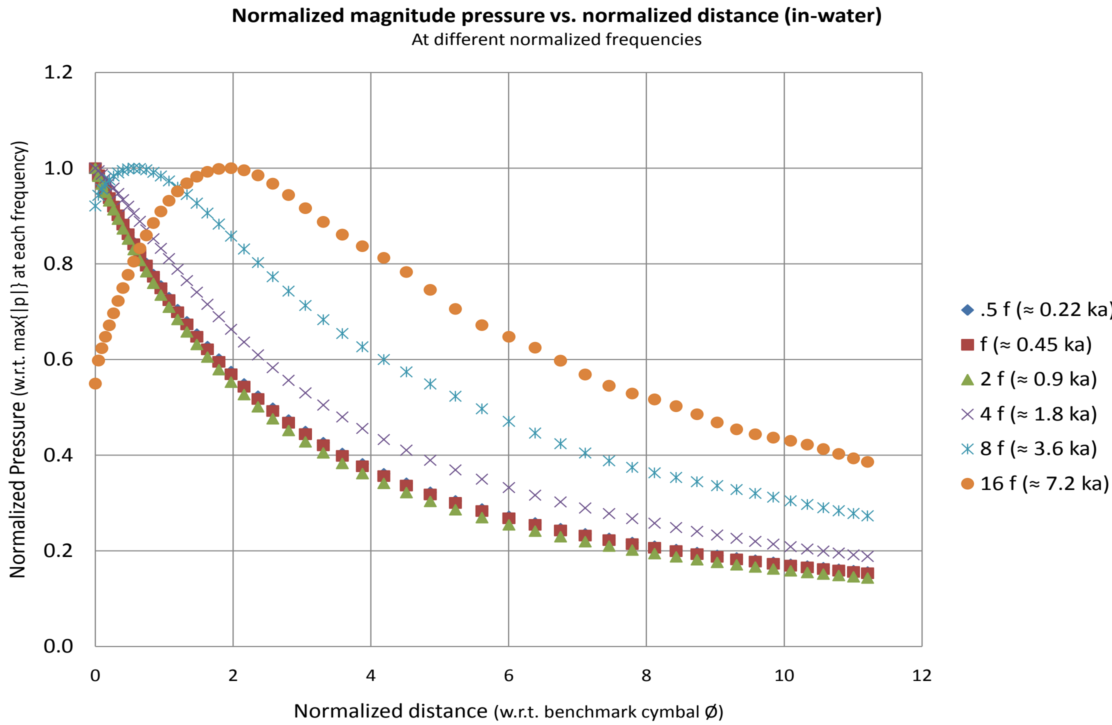

Figure 4.19. $|P|$ vs. on-axis distance for the benchmark array.

4.2.1.6 Loss modulus study

One of the assumptions made in the model was that water loading dominates the loss of the system. This isn't exactly true, as the cover plate material has an extremely high value for its loss factor ($\frac{Y''}{Y'} \approx 2.4$). Because this value was so high, and confidence in it was not, a study of the effect of this loss was performed. Models of the array with a loss modulus (Y'') that was 10% of this value, and with a loss modulus of zero were run for comparison to the benchmark array. These results can be seen in Fig. 4.20. It can be seen that this loss modulus does smooth out some modes in the cover plate, but does not fundamentally change the shape of the transducer response curve. Because of this, it was deemed acceptable to use this high-loss material in future models.

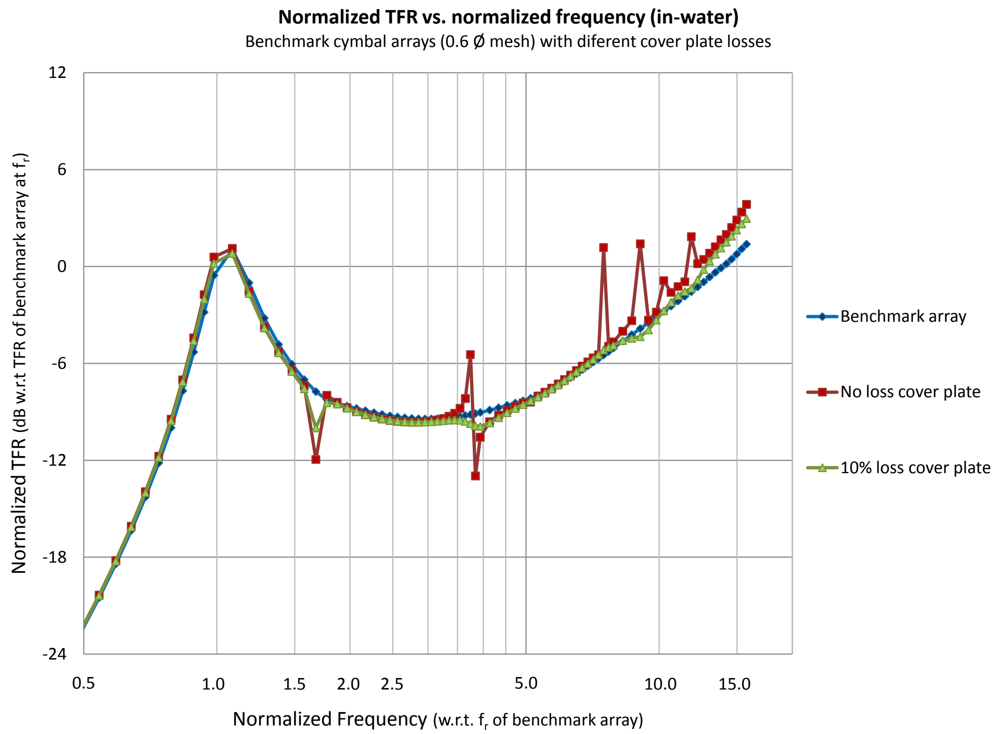

Figure 4.20. A plot of TFR vs. frequency for different loss modulus values. The benchmark array model has the loss detailed in the graphite epoxy composite material in Appendix A.

4.2.2 Rectangular cymbal array

4.2.2.1 Different cymbal lengths: TFR

The first step in determining the dimensions of the prototype rectangular cymbal was looking at several different cymbal lengths. The longer the cymbal, the fewer rows there are in the array matrix. For these initial tests, arrays of 5×8, 4×7, and 3×6 cymbals were chosen. TFR for all of these can be seen in Fig. 4.21.

The dip in response of the 3×6 array was a coupled mode that was not well understood at the time. A similar dip in response for the rectangular array variable study will be discussed further in Chapter 5. For now, it is sufficient to note that there was no obvious benefit in output to using fewer rows. For this reason a prototype array of 4×6 was chosen as the start of the variable study that will follow. It is notable that 4×6 is not what was modeled. The reason for deciding on 4×6 vs. 4×7 is that the 4×6 array allows for 6 transducers in each quadrant. Not having transducers across two of the mirror planes can significantly reduce mesh density.

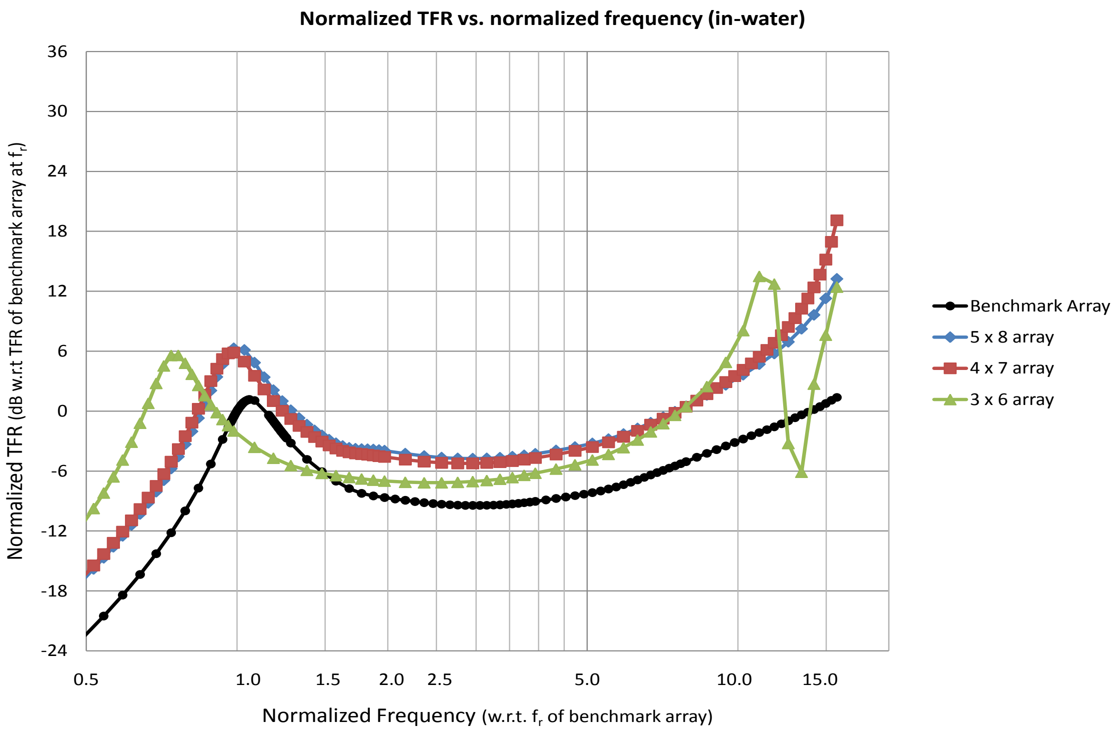

Figure 4.21. A plot of TFR vs. frequency for different rectangular cymbal lengths.

4.2.2.2 Prototype [011] poled PMN-29PT array TFR & $TVAR$

The [011] poled PMN-29PT single crystal array (prototype rectangular array) is seen in Fig. 4.22. This model used the individual rectangular cymbal prototype dimensions detailed in Chapter 3. TFR for this model and the benchmark array can be seen in Fig. 4.23. $TVAR$ for both is shown in Fig. 4.24.

Again a higher order mode shows up in the high frequency end of the curve. In this case it doesn't appear as a reduction in output, as was the case in the cymbal length study[4]. To better see what is happening, a color plot of the magnitude displacement is shown in Fig. 4.25. In an animation of this mode, it is seen that the stud moves out of phase with the two sides of the cap. This would be classified as a (2,2) mode for a clamped-free-clamped-free plate, as there are two nodes along the length and two along the width at the flanges. This mode will be discussed further in Chapter 5.

[4]It is admitted that the dip mentioned could have been part of a modal peak and dip that was not resolved in that case.

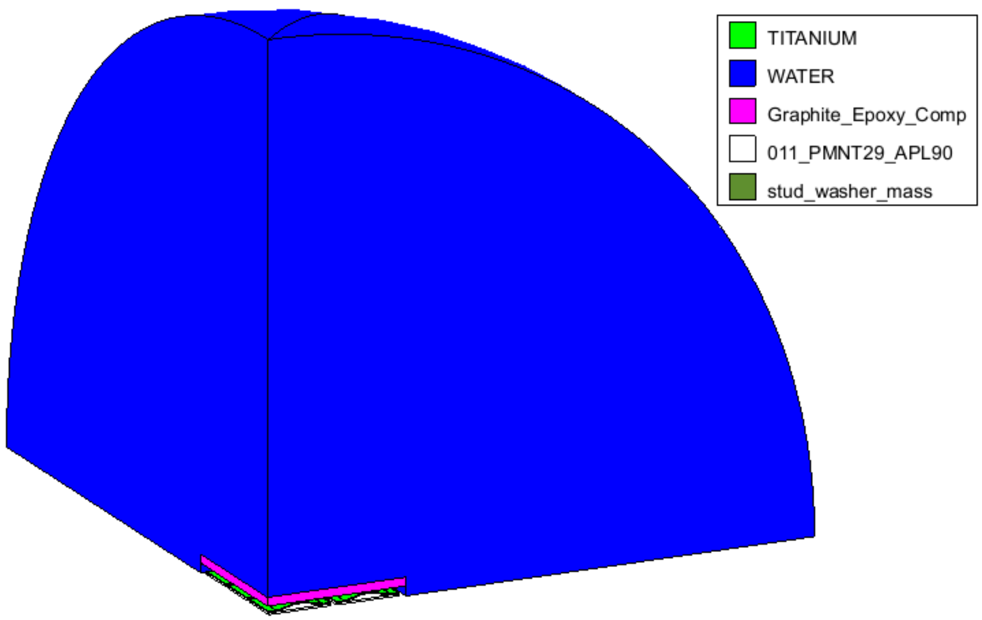

Figure 4.22. The prototype rectangular array model. The view mode in GiD is material colors.

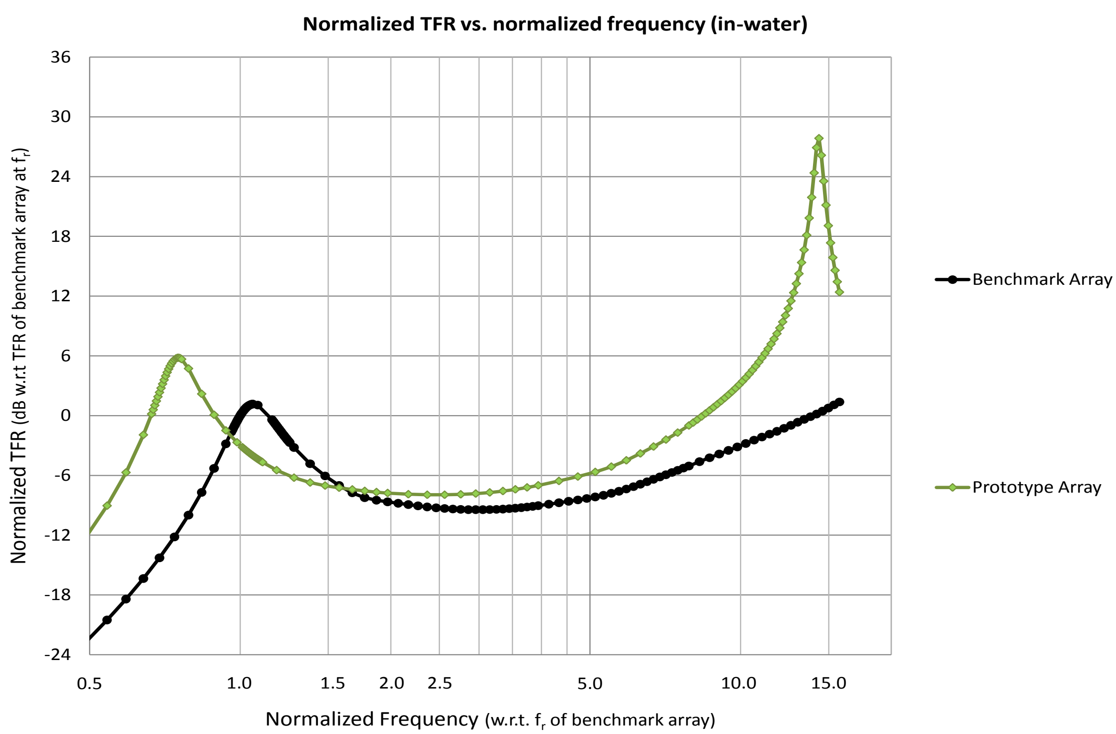

Figure 4.23. A plot of TFR vs. frequency for the prototype rectangular and benchmark arrays.

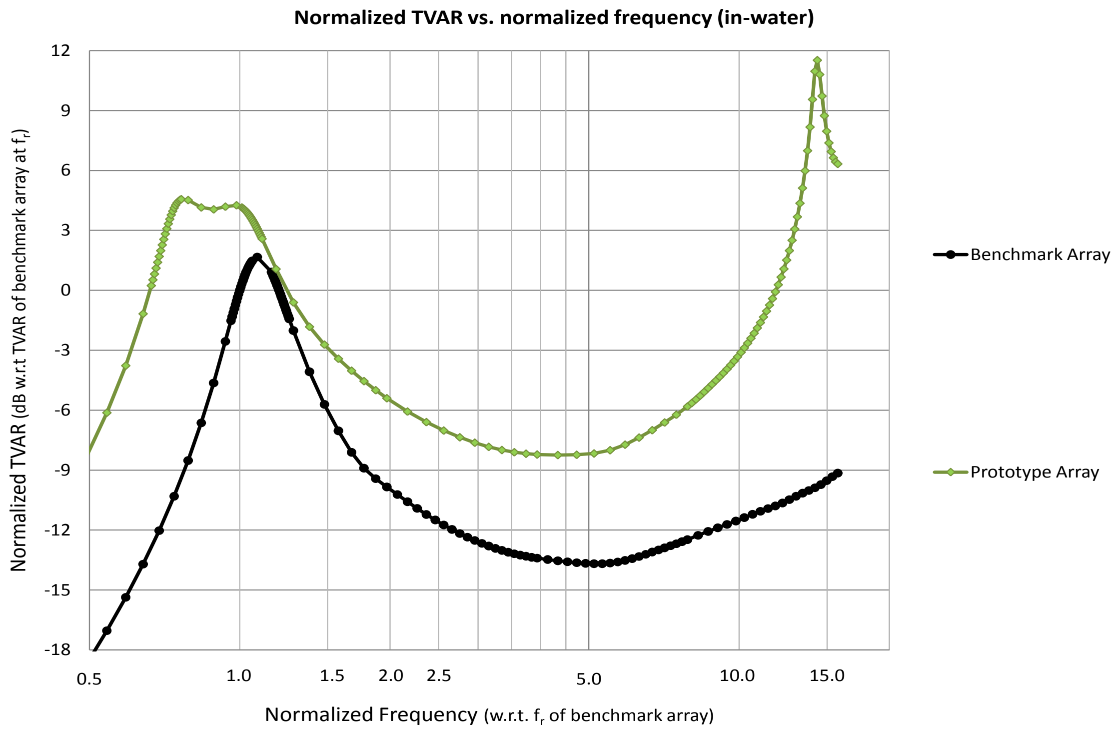

Figure 4.24. A plot of $TVAR$ vs. frequency for the prototype rectangular and benchmark arrays.

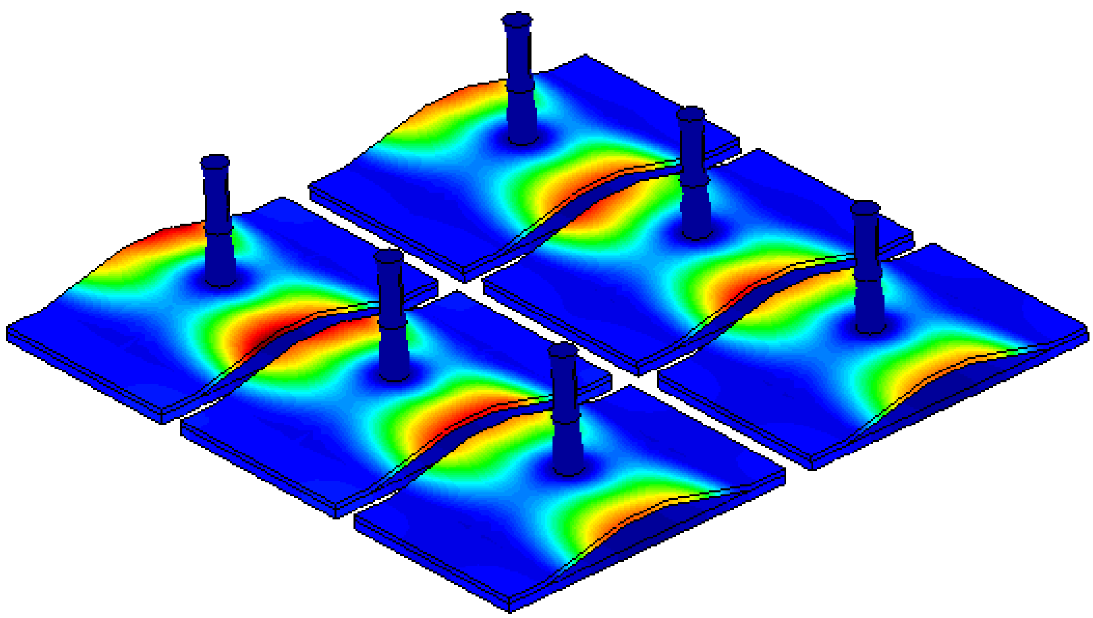

Figure 4.25. A color plot of magnitude displacement of the higher frequency prototype rectangular array mode. The view of the water boundary and cover plate have been turned off for clarity.

4.2.2.3 Prototype array $|Z_E|$ & κ_{eff}

The prototype array $|Z|$ can be seen in Fig. 4.26. The broader dip and peak in the impedance spectrum is the reason for the overall increase in $TVAR$ for the prototype rectangular array over the benchmark in Fig. 4.24. This is also reflected in the effective coupling, which is compared to the benchmark array in Table 4.3.

Design	κ_{eff}
Benchmark array	0.55
Prototype rectangular array	0.71

Table 4.3. Benchmark and prototype rectangular array κ_{eff} comparison.

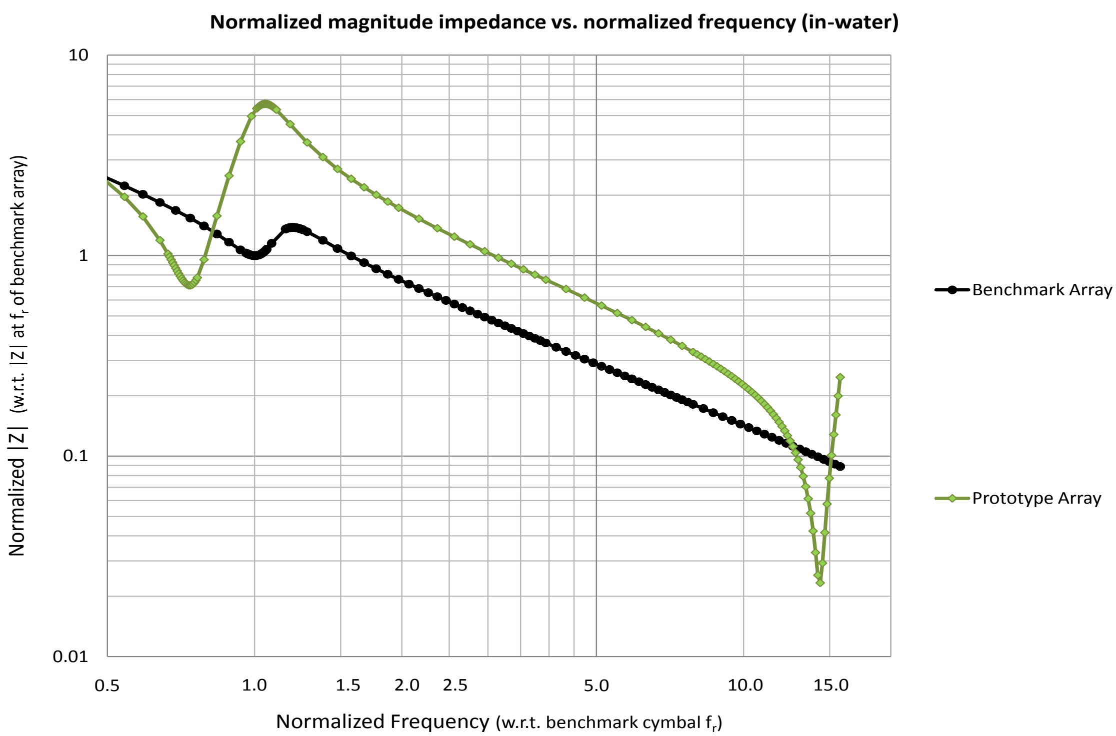

Figure 4.26. A plot of $|Z_E|$ vs. frequency for the prototype rectangular and benchmark arrays.

4.2.3 Variable study results

Once the prototype rectangular array was designed, the variable study mentioned in Chapter 3 was carried out to investigate the relative trends of each dimension on the output and coupling of the array.

As the results presented for all variables will be of the same form, a detailed explanation of each graph is not given. For each of the following subsections, TFR, $TVAR$, $|Z_E|$, and κ_{eff} are presented for the benchmark array, prototype rectangular, and the variations off of it. All variable studies follow a rainbow color convention for clarity. The benchmark array always appears in black, the prototype rectangular always appears as green (the middle of the color spectrum), and the color of curves are shifted towards red if their variable is reduced or shifted towards violet if the variable is increased.

4.2.3.1 Cap depth effects (d_c)

Cap depth for the prototype rectangular array was varied between -60% and +100%. TFR is presented in Fig. 4.27, $TVAR$ in Fig. 4.28, $|Z_E|$ in Fig. 4.29, and a coupling comparison is shown in Table 4.4.

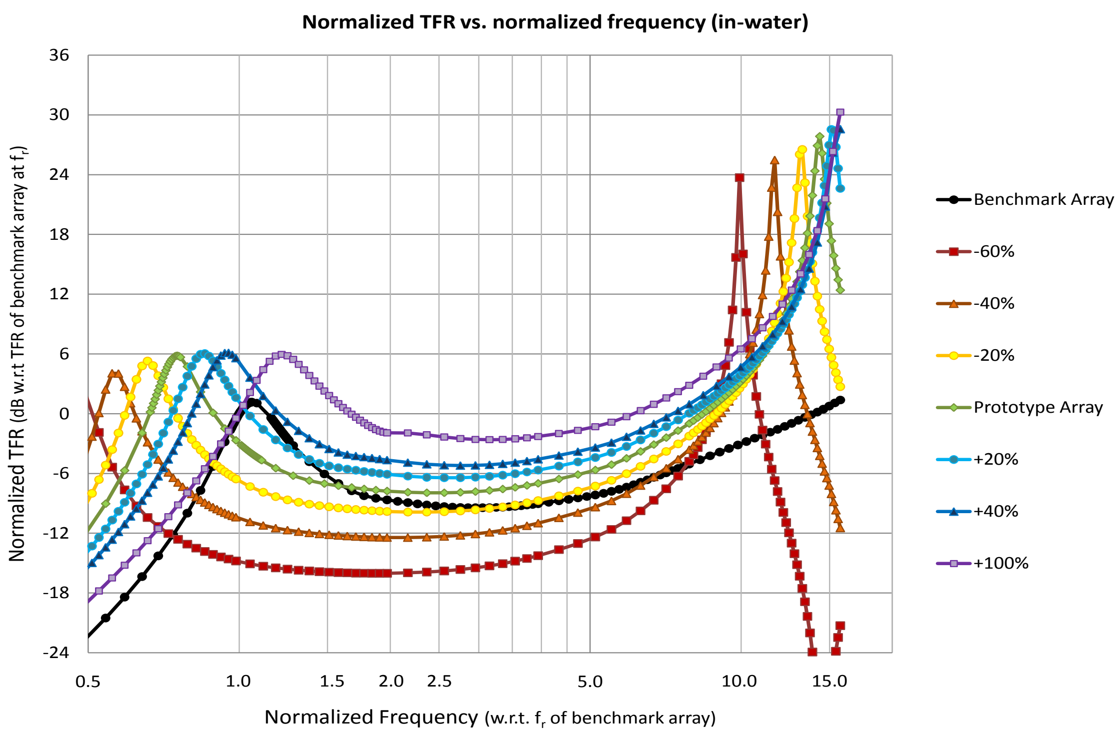

Figure 4.27. A plot of TFR vs. frequency for various values of cap depth, d_c.

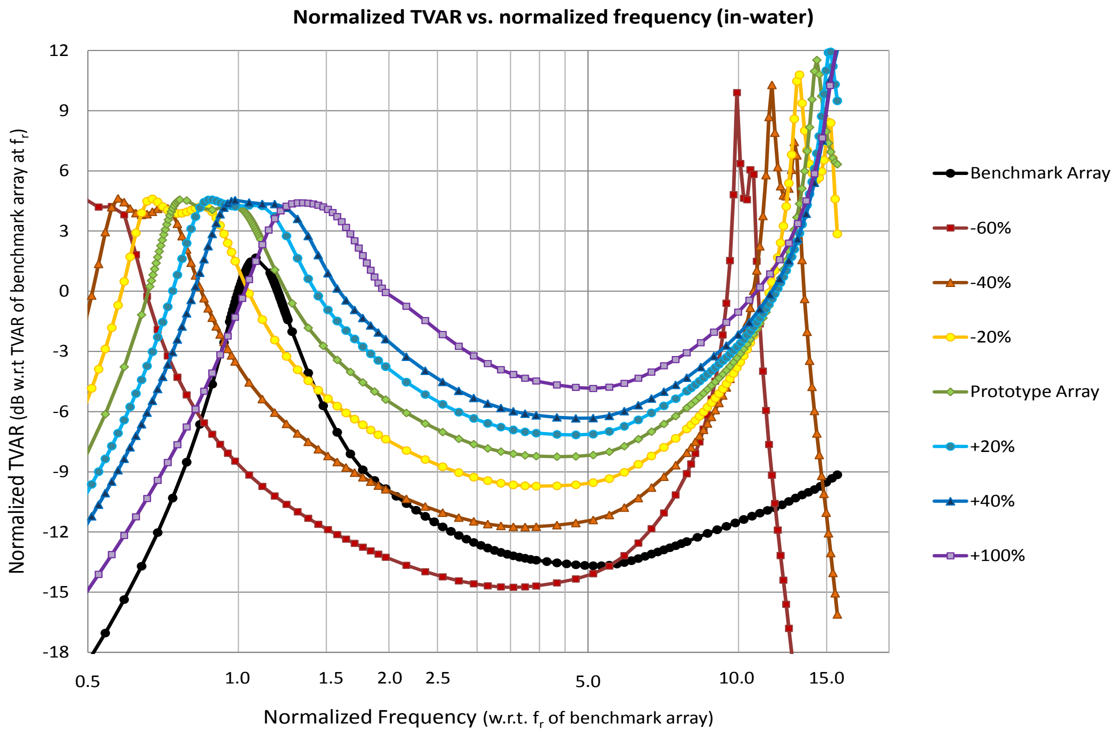

Figure 4.28. A plot of $TVAR$ vs. frequency for various values of cap depth, d_c

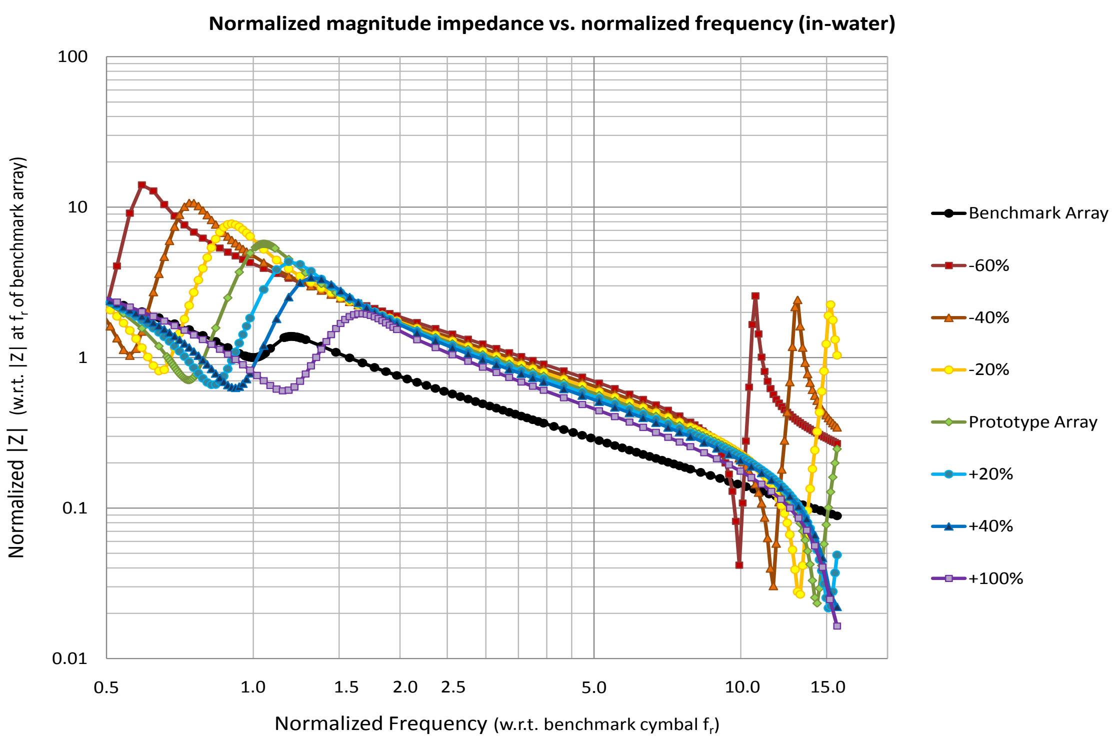

Figure 4.29. A plot of $|Z_E|$ vs. frequency for various values of cap depth, d_c

Design	κ_{eff}
Benchmark array	0.55
-60% d_c	0.60
-40% d_c	0.66
-20% d_c	0.70
Prototype array	0.71
+20% d_c	0.72
+40% d_c	0.72
+100% d_c	0.72

Table 4.4. Cap depth κ_{eff} comparison.

4.2.3.2 Apex radius effects (r_1)

Apex radius for the prototype rectangular array was varied between the prototype value and +220%. It was not reduced from its prototype value due to the fact that it interacts with the washer in this area. Because that interaction is not well defined, reducing the contact area could have predicted results that are unattainable in a real transducer. TFR is presented in Fig. 4.30, $TVAR$ in Fig. 4.31, $|Z_E|$ in Fig. 4.32, and a coupling comparison is shown in Table 4.5.

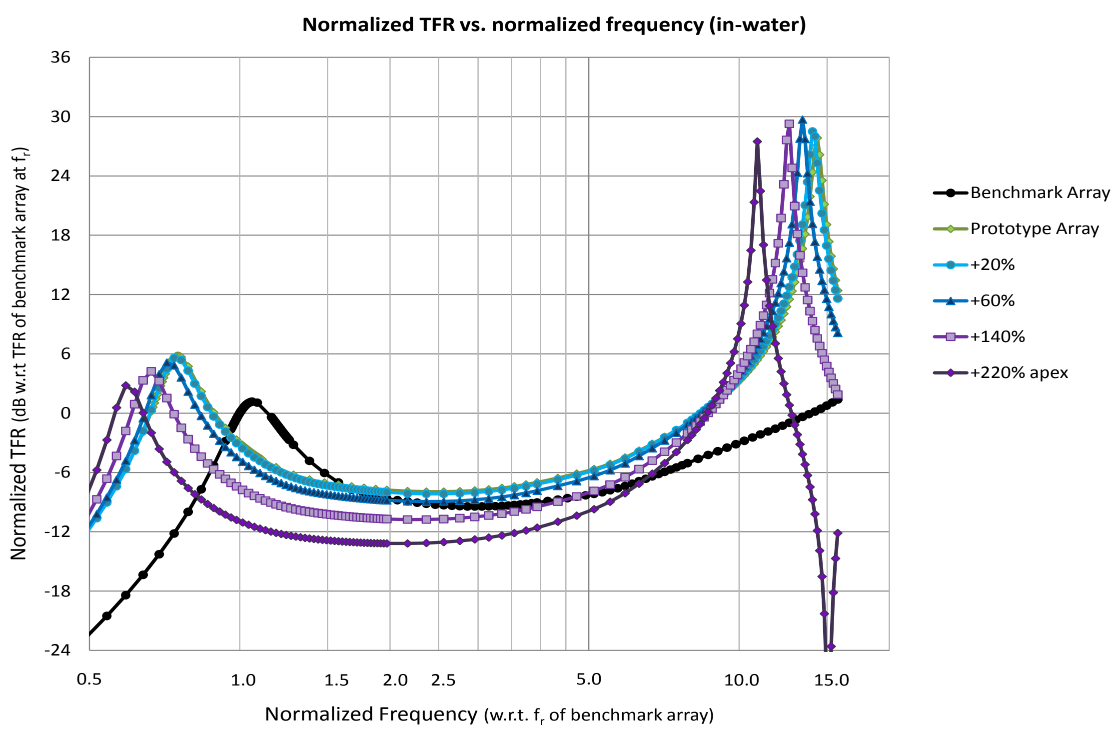

Figure 4.30. A plot of TFR vs. frequency for various values of apex radius, r_1.

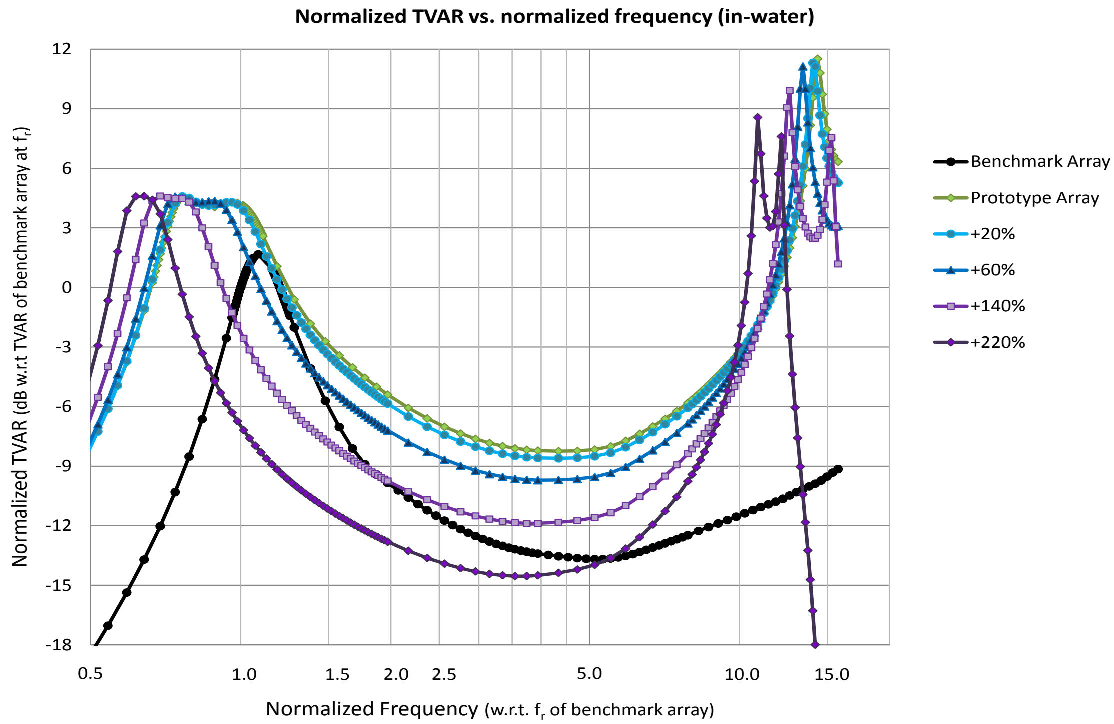

Figure 4.31. A plot of $TVAR$ vs. frequency for various values of apex radius, r_1

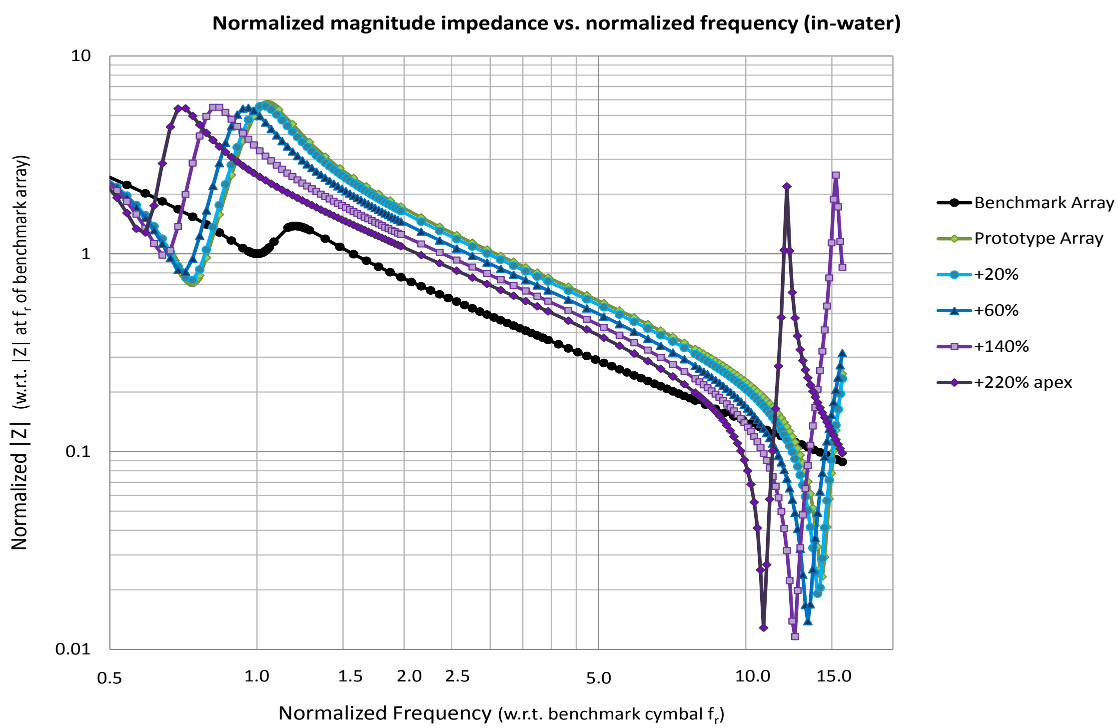

Figure 4.32. A plot of $|Z_E|$ vs. frequency for various values of apex radius, r_1

Design	κ_{eff}
Benchmark array	0.55
Prototype array	0.71
+20% r_1	0.70
+60% r_1	0.67
+140% r_1	0.62
+220% r_1	0.56

Table 4.5. Apex radius κ_{eff} comparison.

4.2.3.3 Cavity radius effects (r_2)

Cavity radius for the prototype rectangular array was varied between -22% and the prototype value. It was not increased because area needed to be left for an epoxy joint. TFR is presented in Fig. 4.33, $TVAR$ in Fig. 4.34, $|Z_E|$ in Fig. 4.35, and a coupling comparison is shown in Table 4.6.

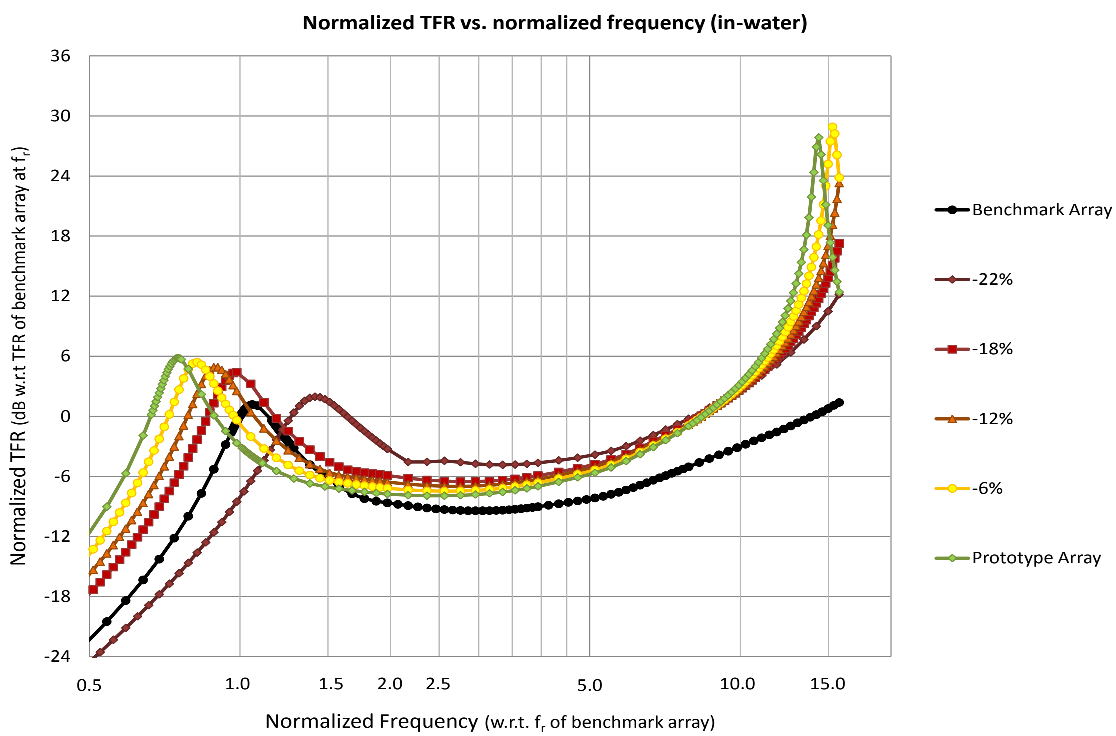

Figure 4.33. A plot of TFR vs. frequency for various values of cavity radius, r_2.

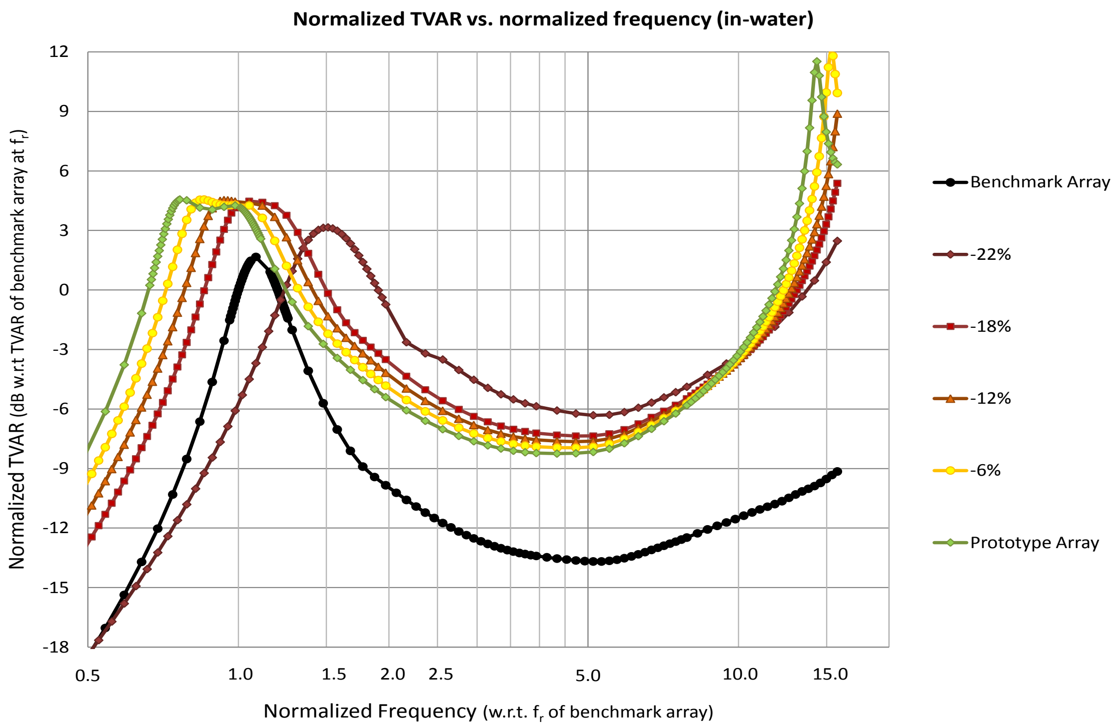

Figure 4.34. A plot of $TVAR$ vs. frequency for various values of cavity radius, r_2

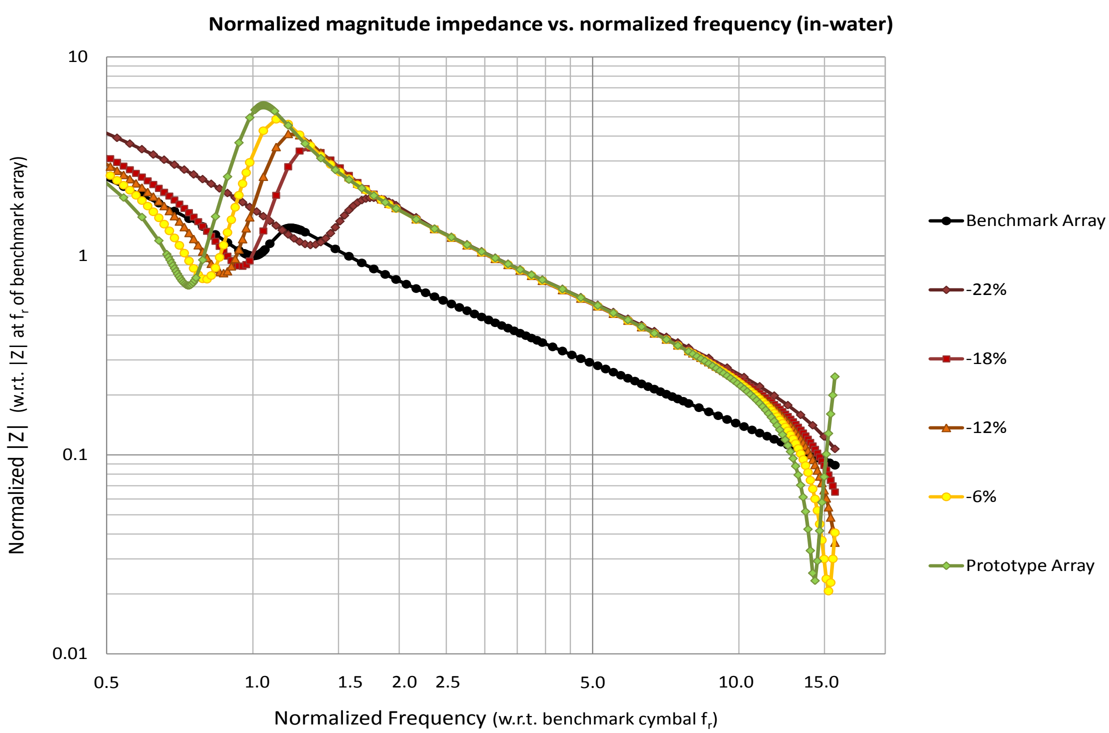

Figure 4.35. A plot of $|Z_E|$ vs. frequency for various values of cavity radius, r_2

Design	κ_{eff}
Benchmark array	0.55
-22% r_2	0.66
-18% r_2	0.69
-12% r_2	0.70
-6% r_2	0.71
Prototype array	0.71

Table 4.6. Cavity radius κ_{eff} comparison.

4.2.3.4 Cap thickness effects (t_c)

Cap thickness was varied between -17% and +150%. The limit was set at -17% because a significantly thinner cap would likely experience permanent deformation during high signal drive. The purpose of one data point below was to better understand the trend in output. TFR is presented in Fig. 4.36, $TVAR$ in Fig. 4.37, $|Z_E|$ in Fig. 4.38, and a coupling comparison is shown in Table 4.7.

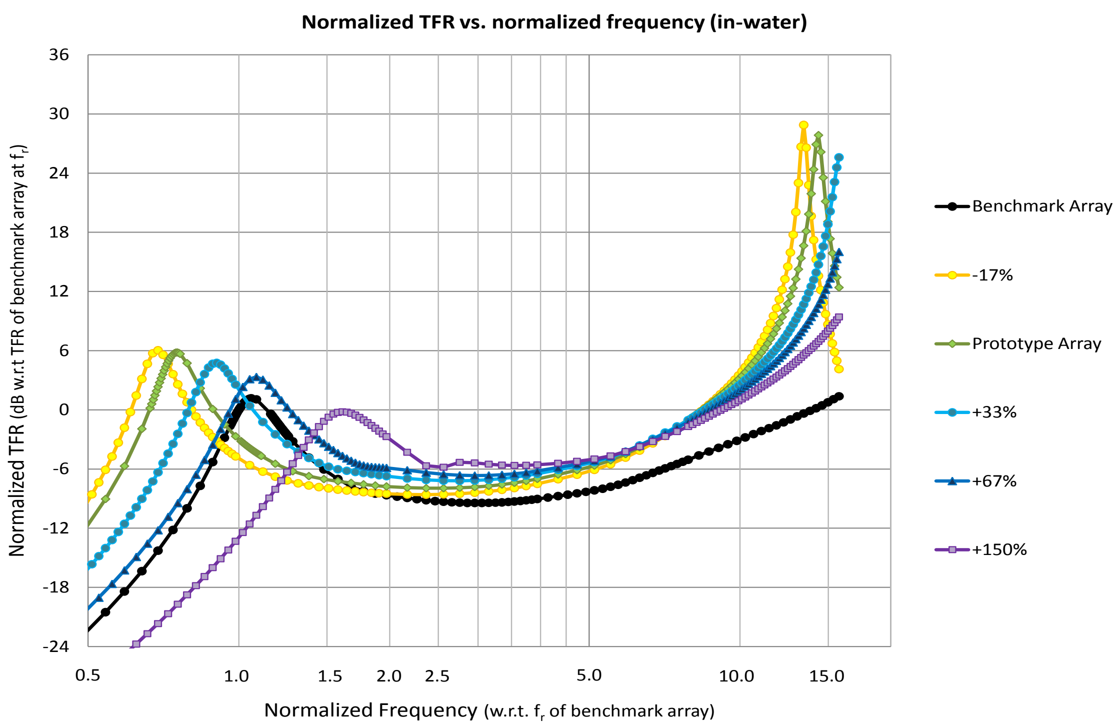

Figure 4.36. A plot of TFR vs. frequency for various values of cap thickness, t_c.

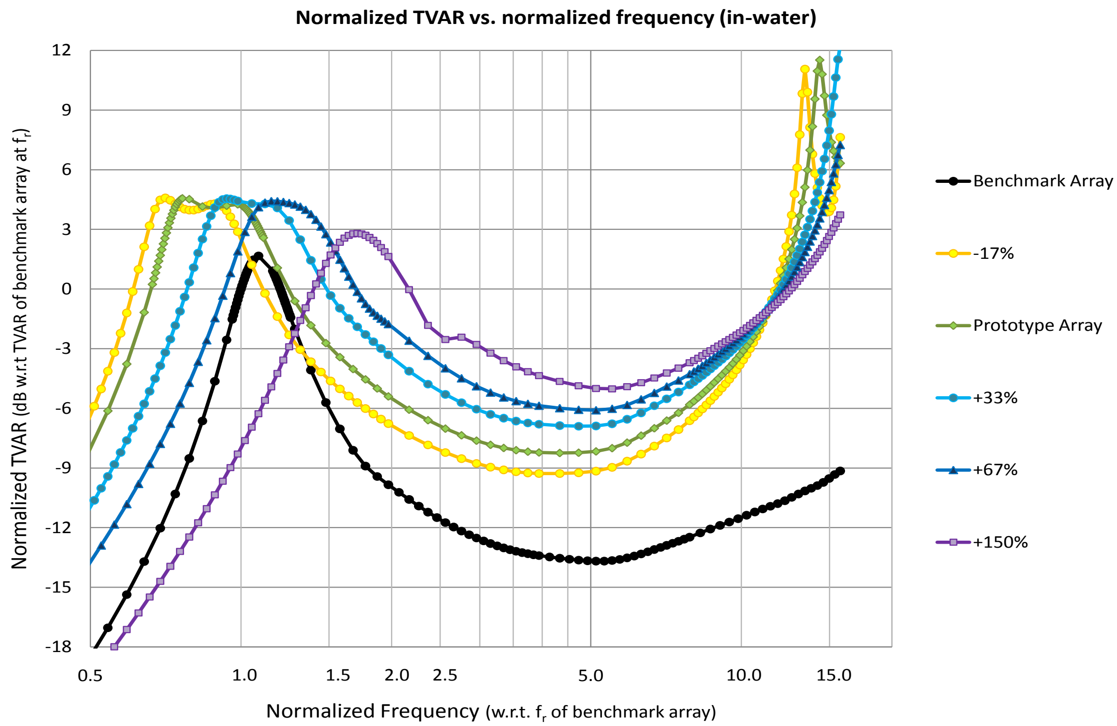

Figure 4.37. A plot of $TVAR$ vs. frequency for various values of cap thickness, t_c

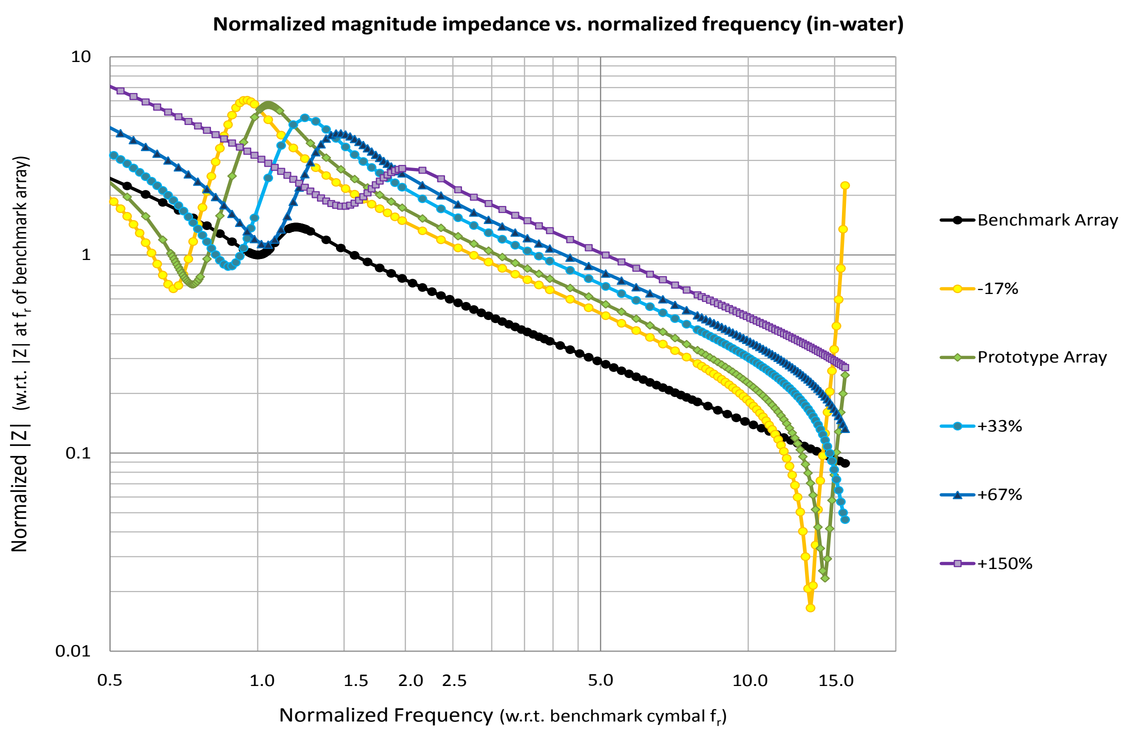

Figure 4.38. A plot of $|Z_E|$ vs. frequency for various values of cap thickness, t_c

Design	κ_{eff}
Benchmark array	0.55
-17% t_c	0.70
Prototype array	0.71
+33% t_c	0.72
+67% t_c	0.71
+150% t_c	0.69

Table 4.7. Cap thickness κ_{eff} comparison.

4.2.3.5 Crystal thickness effects (t_x)

Crystal thickness was varied between -50% and +400%. This was the original reason for reporting TFR instead of TVR. All models were run at the same 1 $\frac{V}{mm}$ as before. TFR is presented in Fig. 4.39, $TVAR$ in Fig. 4.40, $|Z_E|$ in Fig. 4.41, and a coupling comparison is shown in Table 4.8.

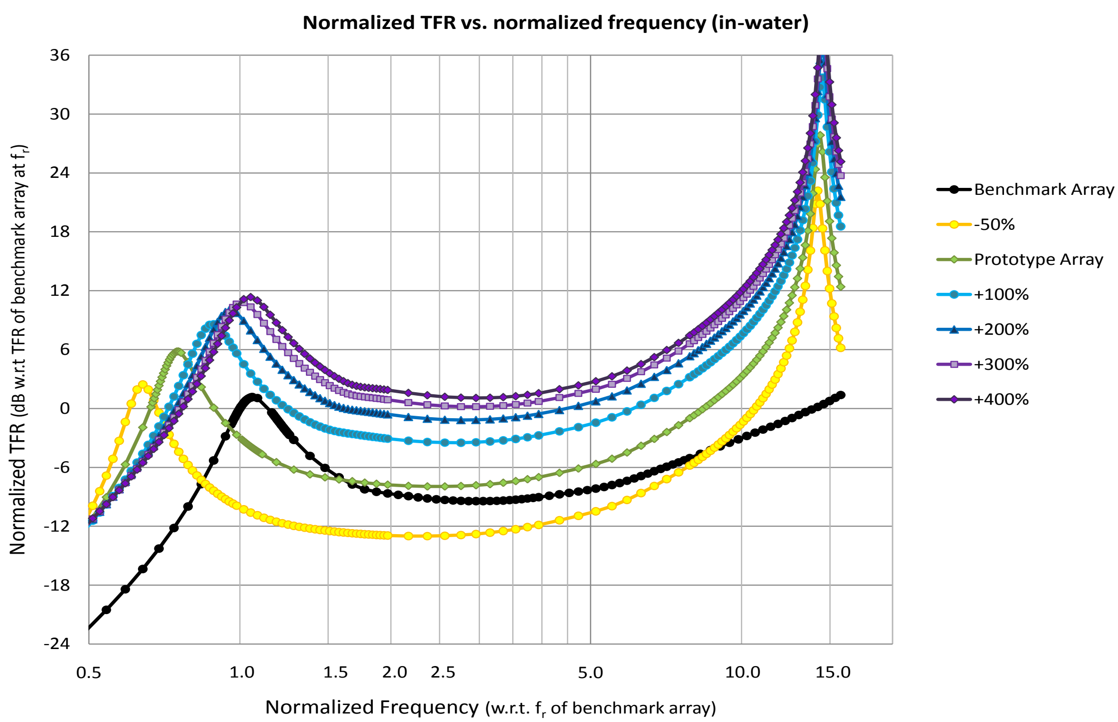

Figure 4.39. A plot of TFR vs. frequency for various values of crystal thickness, t_x.

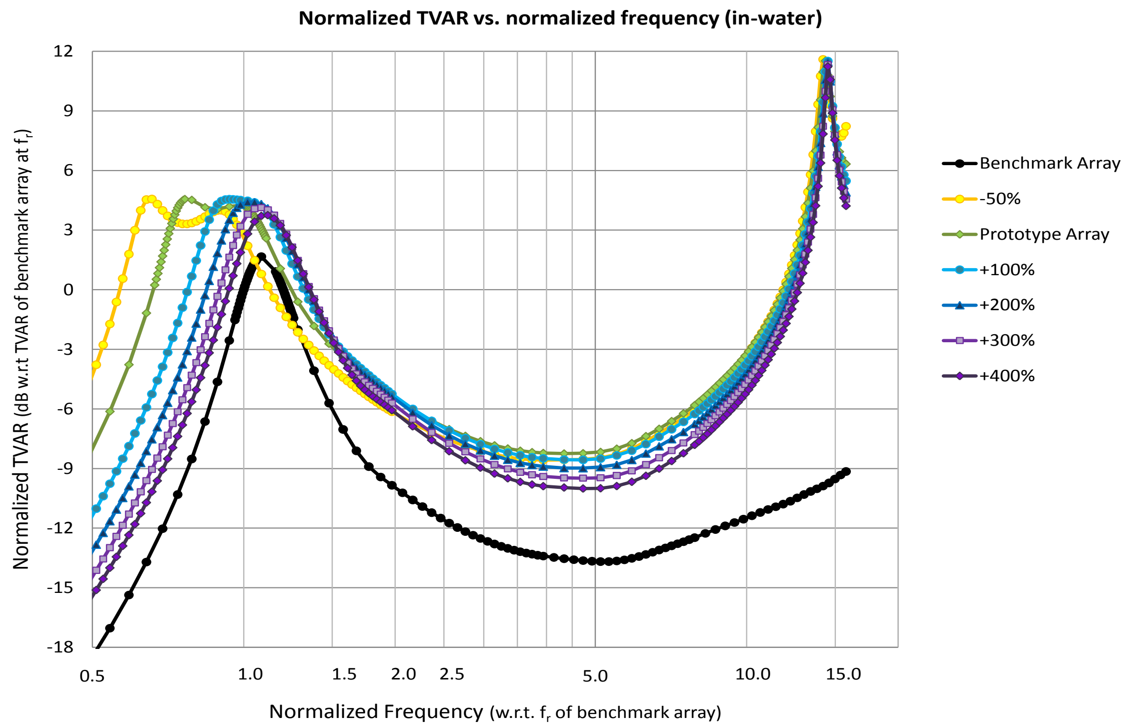

Figure 4.40. A plot of $TVAR$ vs. frequency for various values of crystal thickness, t_x

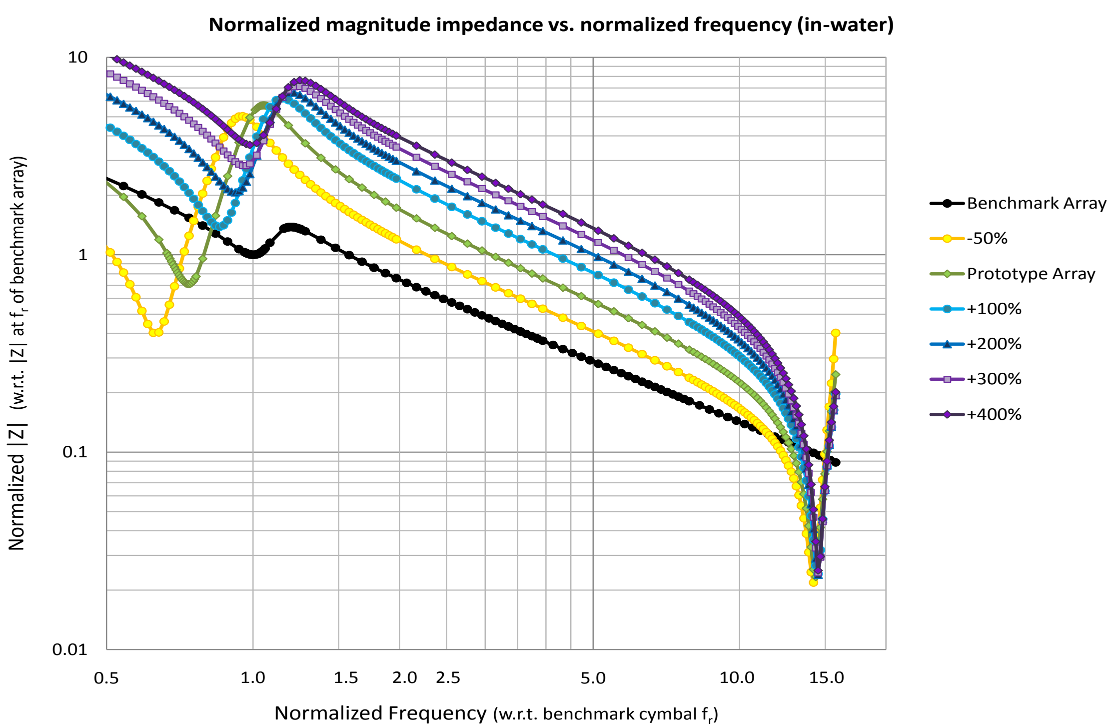

Figure 4.41. A plot of $|Z_E|$ vs. frequency for various values of crystal thickness, t_x

Design	κ_{eff}
Benchmark array	0.55
-50% t_x	0.75
Prototype array t_x	0.71
+100% t_x	0.67
+200% t_x	0.65
+300% t_x	0.63
+400% t_x	0.62

Table 4.8. Crystal thickness κ_{eff} comparison.

4.3 Direct comparison of [001] & [011] poled single crystal designs

To better understand the influence of the cap design on the relationship between the two arrays, models were run with each crystal for each cap design. In the case of the benchmark array, [001] poled PMN-30PT was replaced with [011] poled PMN-29PT. For the prototype rectangular array, the [011] poled material was replaced with the [001] poling.

TFR, $TVAR$, $|Z_E|$ and κ_{eff} are presented for each in a manner similar to the results above. The color coding for the benchmark array with [001] crystal (black) and the prototype rectangular array with [011] crystal (green) were kept.

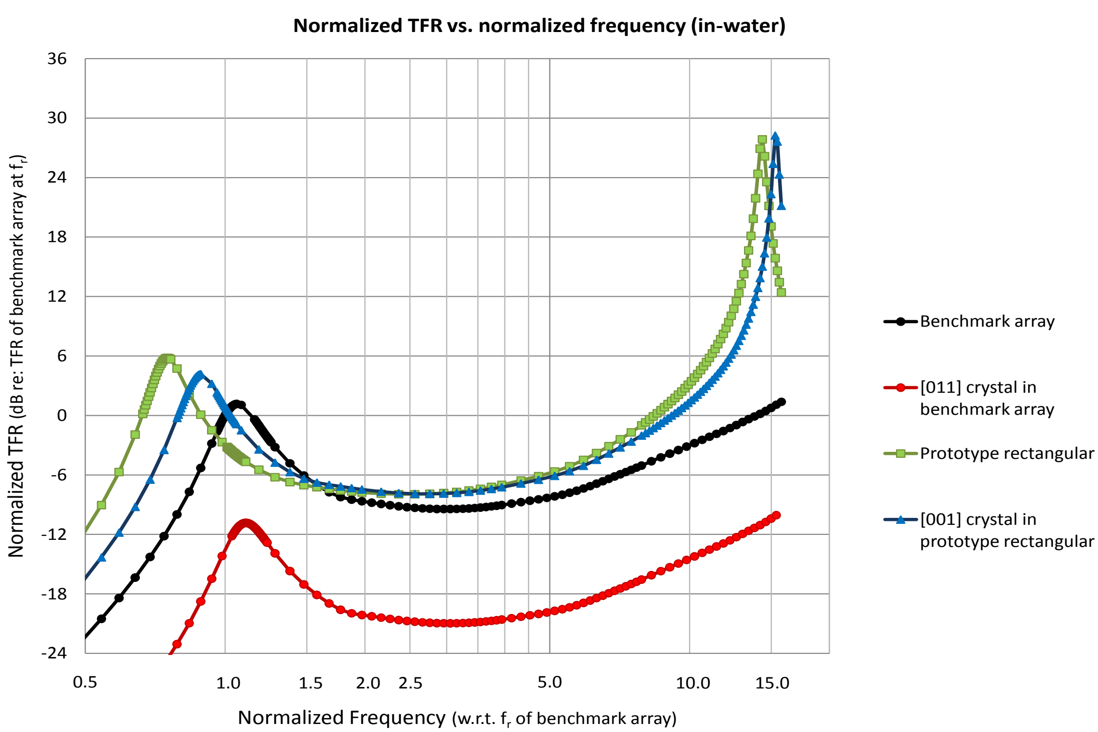

Figure 4.42. A plot of TFR vs. frequency for all combinations of cymbal cap and crystal type.

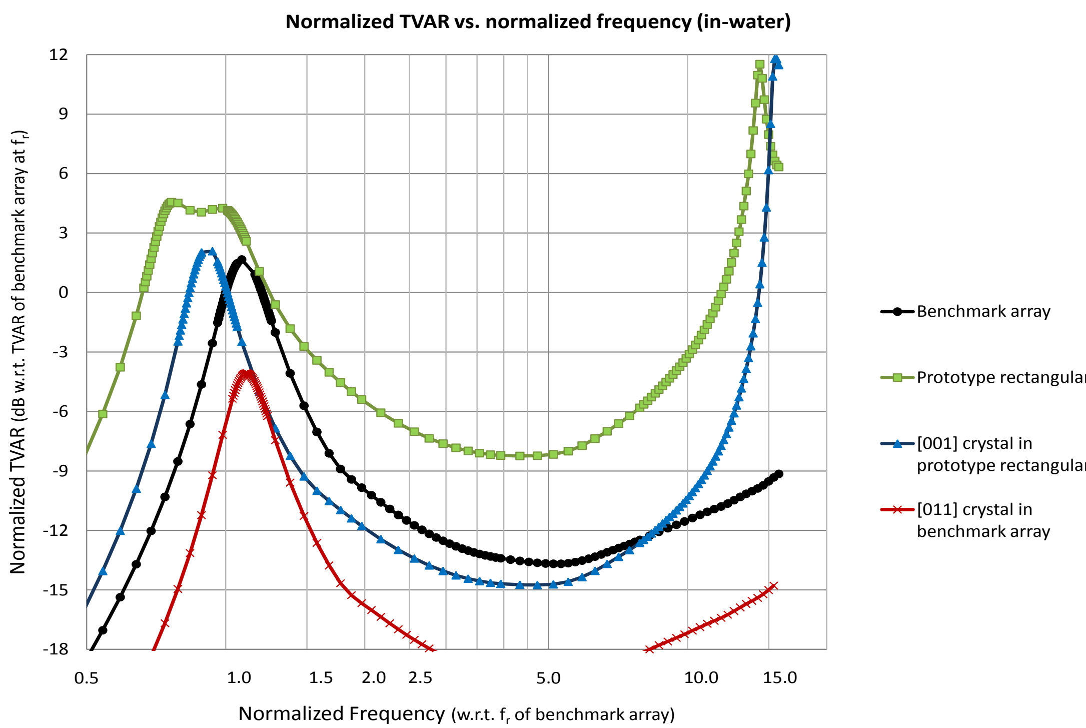

Figure 4.43. A plot of $TVAR$ vs. frequency for all combinations of cymbal cap and crystal type.

Design	κ_{eff}
Benchmark array	0.55
Benchmark w/ [011] poled PMN-29PT	0.29
Prototype rectangular array	0.71
Prototype rec. w/ [001] poled PMN-30PT	0.53

Table 4.9. Cymbal/crystal pairing κ_{eff} comparison.

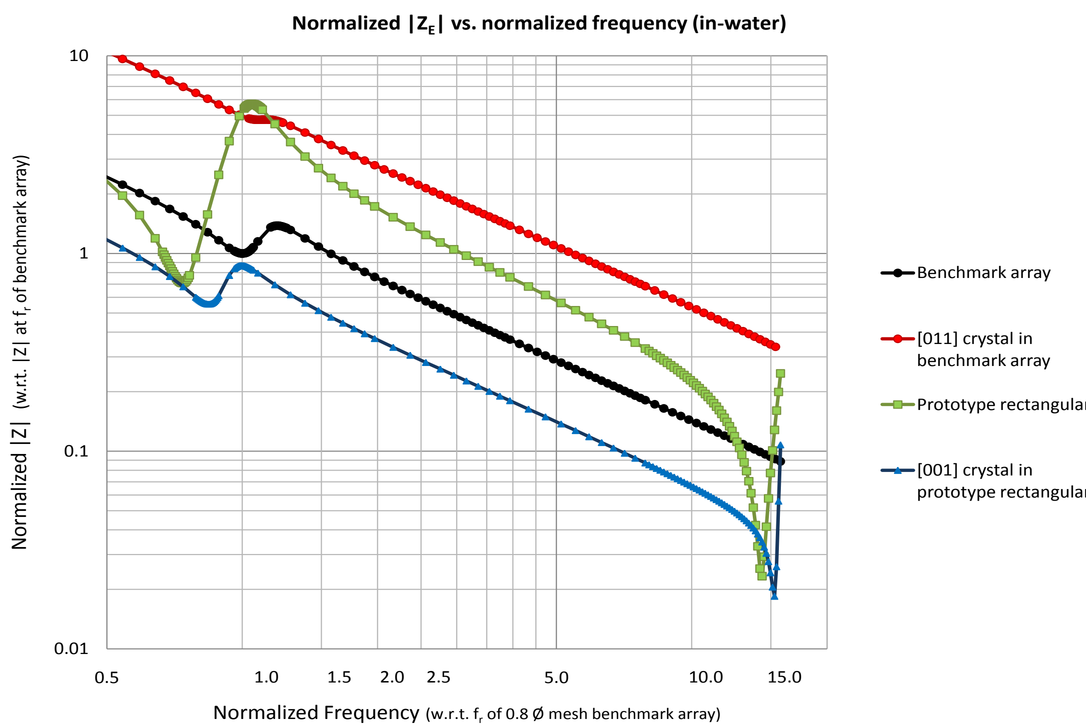

Figure 4.44. A plot of $|Z_E|$ vs. frequency for all combinations of cymbal cap and crystal type.

Chapter 5

Discussion & Conclusions

5.1 Variable Trends

The impact of each dimension of the variable study on the [011] poled crystal rectangular cymbal arrays can be gleaned from the graphs provided in Chapter 4. The major points will be discussed in the sections that follow, with a particular emphasis on designing the ideal cymbal for an array.

For a clearer view of the strength each variable has over the fundamental resonance frequency, a plot was made of f_r versus the percent change in dimension in Fig. 5.1. A similar plot showing TFR at f_r for each array versus percent change in dimension is shown in Fig. 5.2. For each graph, the location of the prototype rectangular cymbal model is shown with the green axis crossing. The trends of each dimension off of this prototype are discussed in the sections to follow.

In the case of cap depth, both individual cymbal trends and array trends are discussed. The purpose is to show that individual cymbal displacement in-air cannot be taken to be an indicator of array output in-water. Once this point became obvious, a detailed study of other individual cymbal trends became unnecessary, as the goal was improved array performance. As a point of reference, the reader is referred back to Figure 3.13 for a visual description of the variables studied.

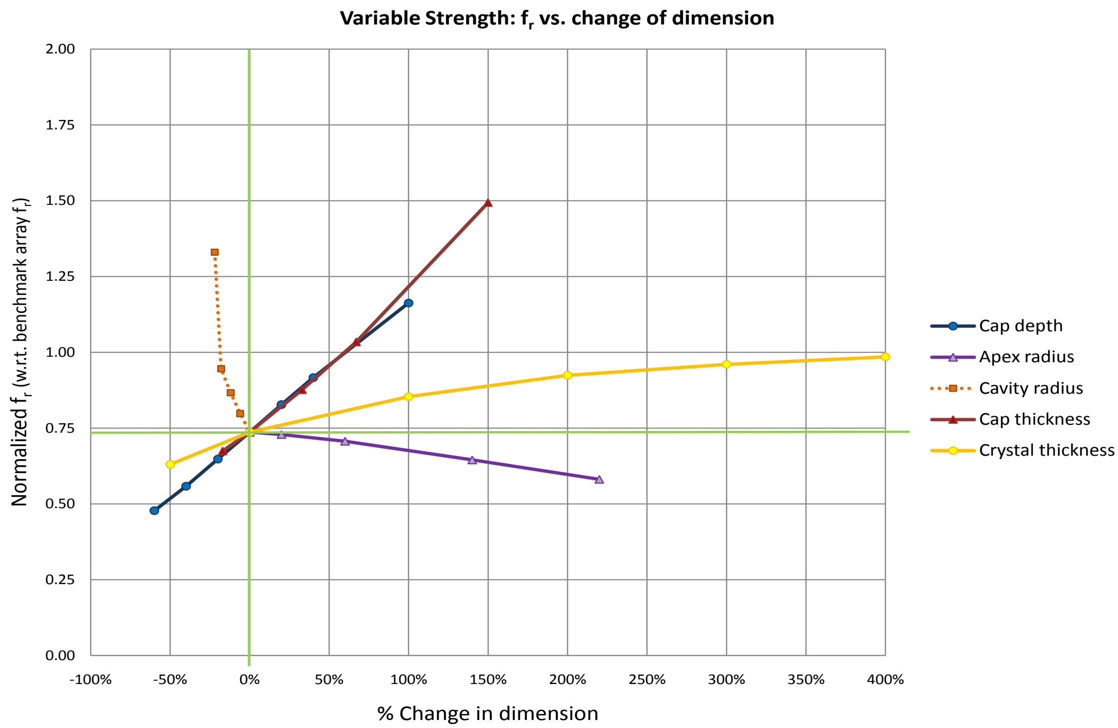

Figure 5.1. A plot of f_r vs. % change in dimension for each of the variables studied.

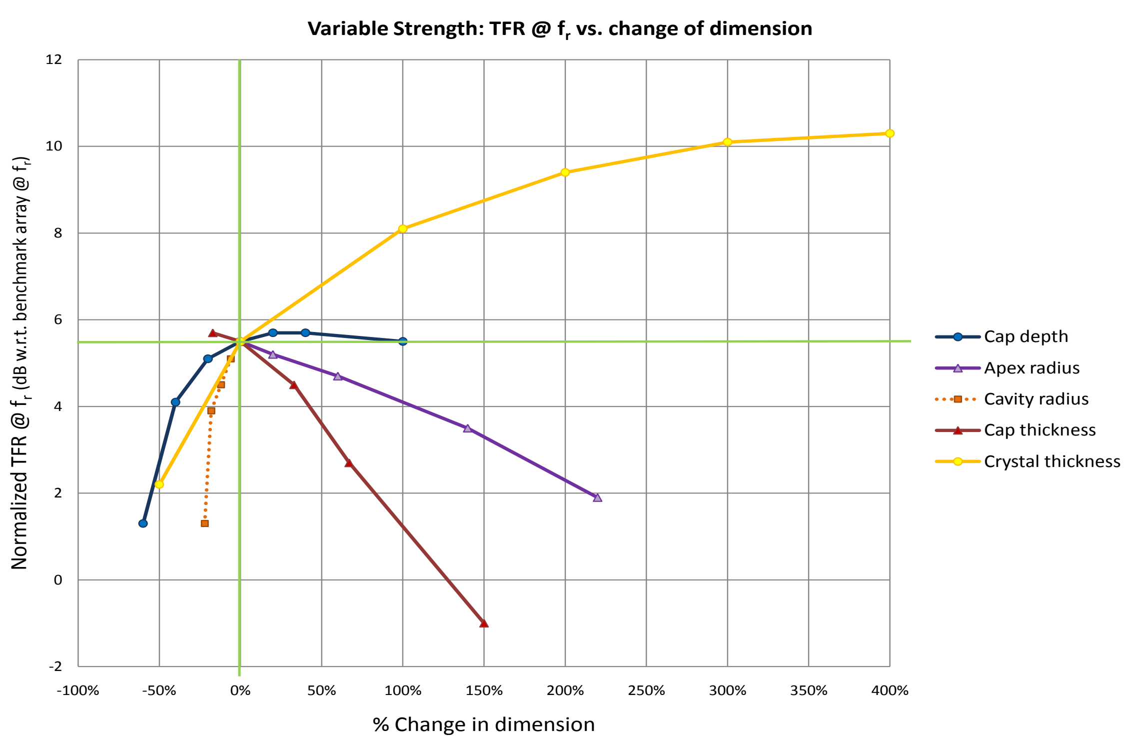

Figure 5.2. A plot of the TFR at f_r vs. % change in dimension for each of the variables studied.

5.1.1 Cap depth (d_c)

The effect of cap depth was studied for both individiual cymbal displacement and resonance frequency in-air, as well as array output and resonance frequency in-water.

5.1.1.1 Individual cymbal cap depth

To more clearly show the relationship between cap depth and both displacement and resonance frequency, both were plotted versus the change in d_c in Fig. 5.3. The displacement curve, shown in red, exhibits exponential decay with increasing d_c. The resonance frequency, shown in blue, shows an approximately linear (possibly weak logarithmic) relationship where increasing the depth of cap increases the resonance frequency.

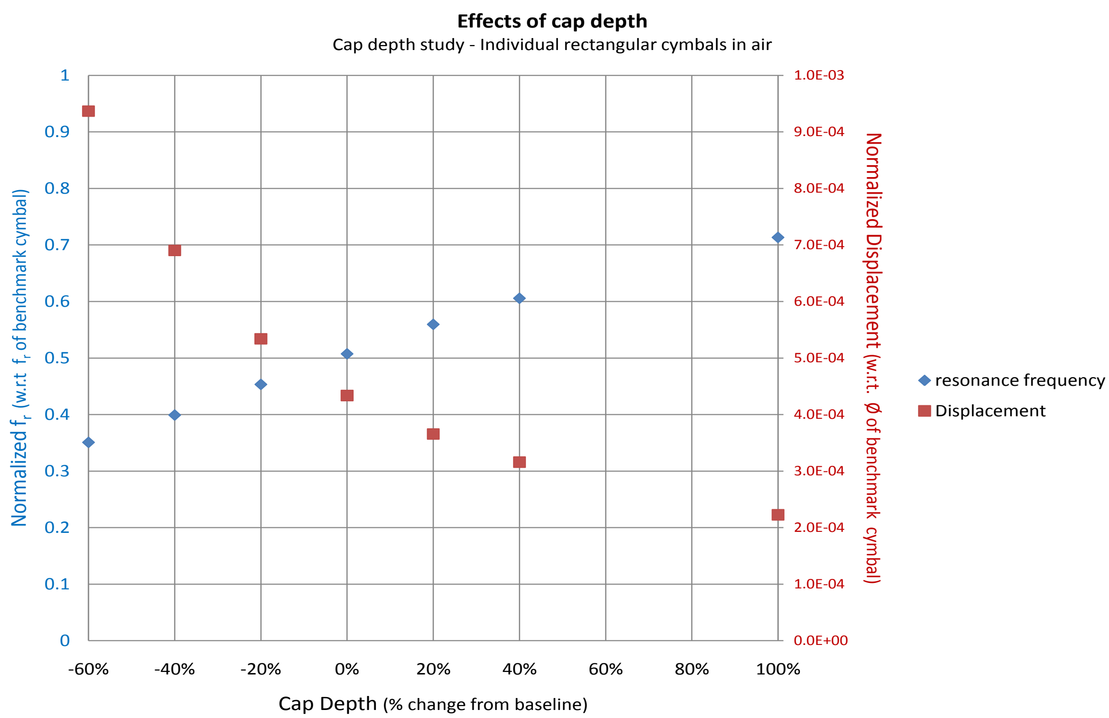

Figure 5.3. Rectangular prototype cymbal: f_r and displacement vs. change in dimension.

5.1.1.2 Array cap depth

For the array, the d_c results can be seen as the blue curve in Figs. 5.1 & 5.2. Resonance frequency scales linearly with change of dimension, again increasing with increased cap depth. The TFR shows a shoulder consistent with a logarithmic relationship, but appears to start to decline at higher values of d_c.

5.1.1.3 Conclusions on cap depth

In the case of resonance frequency, the individual cymbal trend holds loosely for the array. An increase of 100% in cap depth for the individual cymbal increases resonance frequency in-air by approximately 40% with a linear fit in between. For the array, an increase of 100% in cap depth increases resonance frequency in-water by approximately 60%, again with a linear fit between. With both exhibiting linear behavior in the range studied, it follows that resonance frequency could be tuned quite accurately with the cap depth. However, it is quite likely that the exact slope of this linear relationship is dependent upon the other cymbal dimensions, and relationships between variables cannot be pulled from this study.

For the output, no clear relationship between individual cymbal displacement in-air and array TFR in-water can be drawn. Displacement *increases* with *decreasing* cap depth, as expected from previous cymbal studies. However, this increased displacement does not translate into increased output in the water-loaded array. In fact, the converse is true, as *decreasing* individual displacement in-air follows *increasing* array output in-water.

The missing piece of information that should tie these trends together is the generative force. This was not tracked for the individual cymbal, and it is expected that it would decrease with decreasing cap depth because the cymbal cap would become less stiff in the on-axis direction. It would be interesting to see the relationship between the mechanical impedance (Z_{mech}) of the cymbal at different values of d_c, and if this follows trends in array output in-water.

Looking towards applications, it would appear that cap depth is a desirable variable to change. If the array is on the shoulder of the output vs. d_c curve, the resonance frequency can be tuned without significantly affecting output. Additionally, the depth dependence of array output should be improved with deeper cap cymbals, as they would be stiffer in supporting hydrostatic stress.

Conversely, the depth of cap would be one of the harder dimensions to accurately control in production. If the cymbal caps are stamped, the spring back of the metal could complicate precision cap depth, and would affect this dimension and the cavity radius (r_2) more than any other studied here.

5.1.2 Apex radius (r_1)

From the relatively gentle slope of the purple curves for apex radius in Figs. 5.1 & 5.2, it can be seen that this dimension affects the output of the array the least of any studied. Resonance frequency of the array doesn't change much with changing the apex radius, but an intuitive relationship can be drawn. First consider an effective length of the cap to be made up of the flange length, apex length, and the ramp length. As the apex radius is increased, a less direct connection between apex and flange results, which increases the effective length of the cap. As the effective length increases, the resonance frequency goes down. This decrease in resonance frequency shows up in Fig. 5.1.

Theoretically, the apex radius should be as small as possible, as was outlined in Chapter 2. This shows up in the array results, as increasing the apex radius decreases output. It also acts to decouple the motion of the disk from the stud by making the connection between them more compliant. This is related in the reduced coupling with increased apex radius of Table 4.5. This increased compliance is additionally detrimental in the resistance of the array to hydrostatic pressure. For these reasons, the apex radius should be kept as small as the mounting hardware allows.

5.1.3 Cavity radius (r_2)

Cavity radius is clearly the variable that has the strongest relationship to both f_r and TFR, as can be seen from its steep slope in Figs. 5.1 & 5.2. It would appear that the only consideration in determining cavity radius would be determining the amount of bonding area that is required at the flange. Once this has been determined, the cavity radius should be maximized accordingly.

5.1.4 Cap thickness (t_c)

For the cap thickness, resonance frequency scales linearly with cap thickness and TFR decreases in a complex fashion with increasing cap thickness. It would appear that the ideal cap for output is as thin as possible. This makes sense, as less stress will be built up in the cap, so it can work better as a displacement transformer. However, it is clear from the d_c results that on-axis stiffness of the cap also plays a role in output. Additionally, reducing the cap thickness to increase output should be tempered with the knowledge that stress analysis hasn't been performed on these models.

In a real-world application the stress in the caps is significant, and permanent deformation could result at high-drive and under hydrostatic loads. Any optimization of the cap thickness would have to take into account the stress in the cap and the yield strength of the material used.

5.1.5 Crystal Thickness (t_x)

Changing the crystal thickness shouldn't change the resonance frequency of the array much, as the length mode of the crystal is what is the primary mode being used. This is effectively true, as the weak relationship between t_x and f_r shows in Fig. 5.1.

Output however, changes greatly with crystal thickness. This would lead to the conclusion that increasing t_x is a great way to improve output without affecting the resonance frequency. There are several problems with this conclusion. The first is that increasing TFR this way means that the drive voltage needs to be increased accordingly, which could have a significant impact on the drive electronics. Second, it appears that low-frequency efficiency will likely decrease with increasing t_x. This can be seen in Fig. 4.40, the TVAR curve for t_x, where $TVAR$ suffers in the low-frequency band with increasing crystal thickness. Finally, effective coupling decreases with increasing crystal thickness (Table 4.8), which suggests that bandwidth would suffer.

5.2 Benefits of [011] poled PMN-29PT

5.2.1 Output

The possible increase in output for this design has been well documented at this point. The direct contribution of crystal substitution can be taken from Section 4.3. In this section the results for each cap design with each crystal type are reported. This way cap design contributions may be separated from crystal contributions. Also, because the rectangular cap allows for more active material to be fit under the cover plate, this contribution should be removed when considering the benefits of the specific crystal.

For the rectangular cymbal cap, the [011] poled crystal shows an increase in TFR of approximately 3 dB over the [001] poled crystal with the same cap. Additionally, $TVAR$ is improved by 9-12 dB below resonance and 4-20 dB above resonance.

5.2.2 Operating Bandwidth

Much has been said about the TFR and $TVAR$ of each design, but the more compliant and higher coupling [011] crystal can be used to increase array bandwidth. In this case, the bandwidth is defined to be the frequency range over which a given drive field or power gives a minimum source level target. It can now be understood that a response curve that has a wider frequency range to meet this target has wider bandwidth. The prototype rectangular [011] crystal design has increased output at a resonance frequency that is approximately 25% lower than the benchmark design (Figs. 4.42 & 4.43). Because its response doesn't drop below the benchmark array above resonance, it is classified as having greater bandwidth due to its increased low-end response.

Because the transducer becomes more highly directional at higher frequency, there will eventually be an upper limit in frequency where side lobes become problematic. This is the reason that the (0,2) mode of the circular cymbals isn't as useful in supporting the mid-band as it could be. For this reason, any gains in the low-frequency band of the transducer are that much more significant.

5.3 Open-cap cymbal design

Study of the two array designs and results, Section 4.3 in particular, shows some unique benefits and concerns about the open capped cymbal design used for the [011] poled crystal.

5.3.1 Benefits

5.3.1.1 Cap/crystal mode

The higher order mode shown in Fig. 4.25 is a coupled mode consisting of a fundamental length mode of the crystal and a higher order mode of the cymbal cap. The exact contributions of each haven't been determined, but it is clear that the system has a high mechanical quality factor (Q_m) when operating in this mode.

The benefit of this mode is that it can be used to support the mid-band output by placing it above the operating frequency of the transducer. As opposed to circular cymbal caps, where the location of the (0,1) and (0,2) modes are tied together by the same variable (the radius), this mode should be easier to control. It can be seen from the results in Chapter 4 that this mode does track with several variables (notably not with the crystal thickness). It is also very likely that this mode will be influenced by the width of the cymbals, as the higher order mode of the cap displays motion indicative of two nodes across the width. By reducing the width, and putting more cymbal columns in the array, this mode should increase in frequency.

5.3.1.2 Packing ratio

Fundamentally a rectangular cymbal design can allow for more active material to be put in between two cover plates. The packing ratio of circular cymbals cannot rival what can be achieved with rectangular cymbals, where only assembly tolerances limit how close material can be packed. This is evidenced in the percent area packing percentages for the benchmark design, at 55%, and the rectangular design at 77%.

5.3.2 Concerns

5.3.2.1 Stress

The increased output of the open capped design will likely equate to higher stresses for the same drive level as the benchmark cymbal design. Looking at Fig. 4.42, reproduced below as Fig. 5.4, it can be seen that the rectangular cap design is a source of a significant increase in output. This is likely due to reduced tangential stress in the cap, making it a more effective mechanical transformer. This comes at the expense of increased cap compliance, which is a concern at higher drive levels or under hydrostatic pressure. The higher order crystal/cap mode is of particular interest, as the cap undergoes significant strain in this mode. Testing would need to be done to assure that the cap material and thickness selected could withstand the stresses required if this mode were to be used directly.

5.3.2.2 Exposed cavity

Traditional circular cymbals can be easily waterproofed with a thin coating of polyurethane after the caps have been bonded to the active material. In the case of these rectangular cymbals, this would not be possible, as the stiff cap doesn't fully enclose the cavity. In the case of arrays, this isn't as big of a concern, as a gasket could be made to fit over the cover plates. However, if the individual cymbals were to be used in an underwater environment, a new method of waterproofing would need to be developed.

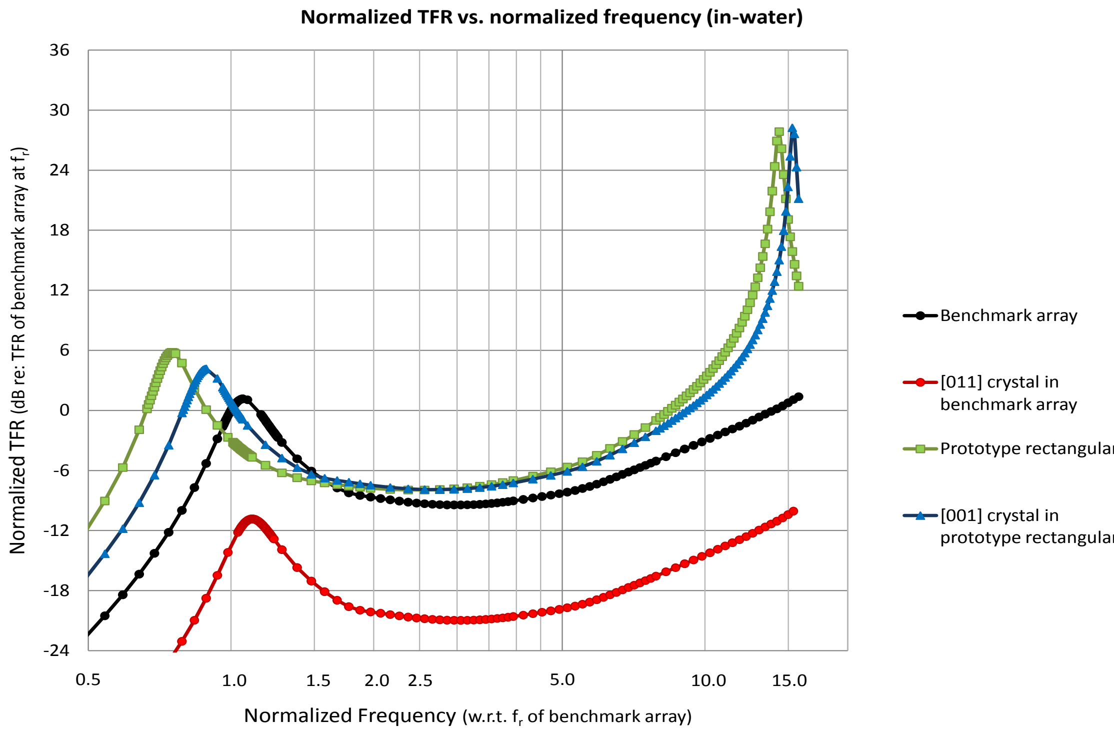

Figure 5.4. A plot of TFR vs. frequency for all combinations of cymbal cap and crystal type. Reproduced from 4.42.

5.3.2.3 Increased transducer thickness

It has been shown that, to some extent, deeper cymbal caps increase array output . Figure 5.2 shows that output increases as d_c increases. For the prototype array, the value for d_c chosen increases the overall array thickness by approximately 10% over the benchmark array. This seems like a small price to pay for an increase in output of 6 dB, but may still be a concern in applications where space is at a premium.

5.4 Future work

The results of this study encourage further consideration of using [011] poled single-crystal PMN-29PT in cymbal designs. Study of the effect of several variables on array performance provides for a better understanding of the design window, but more work must be done before fully implementing this design.

5.4.1 Experimental verification

Most importantly, the FEA results need to be confirmed with an experimental array. This will prove, or call into question, the validity of the models used in this study. It will also allow for better understanding of the efficiency of this design and how it relates to other [001] poled single-crystal designs.

Construction of an experimental array will also allow for driving the cymbals to failure after other characterization data has been collected. This, in addition to FEA stress analysis, will give insight into the weaknesses of this design. While it has been documented in the past that the epoxy bond is a weakness in cymbals, it will be interesting to see if the more compliant cap design doesn't become the primary concern at high-drive.

5.4.2 Stress analysis

5.4.2.1 Cap

The stresses in the cymbal cap are of primary interest in this design. This is the largest change that has been made compared to the traditional cymbal, and it is important to fully understand its impact. A study of the principal stress in the cymbal cap across the frequency band needs to be undertaken.

Additionally, the impact of hydrostatic stress on the compliant cap design should be studied. Significant differences in the depth dependent properties of this array design could be a limiting factor in its viability. There is a good chance that this could be mitigated with different designs (i.e. deeper caps or thicker caps), but this must be studied.

Finally, depending upon the results of the stress analysis, transverse stresses in the cap should be mitigated as much as possible in the rectangular cymbal. As was seen in Chapter 1, decreases in tangential stress in the moonie (by moving to the cymbal) and the cymbal (by slotting) lead to increased output. This is also studied in Appendix B, where slotted cymbals are studied both experimentally and with FEA models. It follows then that if there are significant transverse stresses in the rectangular cymbal, mitigating them could be beneficial to array output.

5.4.2.2 Crystal and epoxy

Unlike the cymbal cap material, accurate failure data for the crystal and epoxy is harder to obtain. Any FEA stress analysis needs to be backed with experimental failure analysis of both materials. As the single-crystal materials are relatively new, little literature exists on their strength in various failure modes. As such, FEA predicted stresses can only tell the relative change in stress state from traditional cymbal designs to this new design.

However, this is not to say that FEA stress analysis isn't still valuable. There have been previous studies of traditional cymbal failure in the literature, and predictions in relative stress between the two designs should point to glaring differences in their expected performance.

5.4.3 Optimization of aspect ratio

The length and width of the cymbal were two of the variables that weren't studied in this work. Fundamentally, there must be an ideal aspect ratio for the cymbal based on the differences in the

d_{31} and d_{32} piezoelectric field coefficients. Determination of this aspect ratio would likely require a similar parametric study of the these two dimensions where ratios between cap dimensions are held constant in hopes of removing their influence on the results.

Also, while a rectangular cymbal was an obvious starting point for competing transverse coefficients, there is no obvious reason that it is the best design. It does have the benefit of an excellent packing ratio, but there may be an elliptical cymbal profile that would better decouple the effects of d_{31} and d_{32}.

Appendix A

Material data files for benchmark and baseline rectangular cymbal arrays

A.1 [001] crystal benchmark cymbal array

The following text is from the 'Material data lookup table' that GiD/ATILA creates when a model is solved. This table is from the [001] poled PMN-30PT benchmark cymbal array model. The notes for entries are on the right and are denoted by a '-'. Any notes that ran off of the page were moved to the next line. Other than this, the file was not changed in any way from what was generated by the program.

```
GiD Name   = TITANIUM
ATILA Name = M0001

 Young's Modulus            E =   1.080000E+011 (N/m^2)         - E > 0
 Poisson ratio             nu =   3.610000E-001                 - -1 < nu < 1/2
 Density                  rho =   4.500000E+003 (kg/m^3)
 Bulk Modulus               K =   1.294964E+011 (N/m^2)         - K > 0
 Shear Modulus              G =   3.967671E+010 (N/m^2)         - G > 0
 1st Lam constant         mu =   3.967671E+010 (N/m^2)         - mu = G
 2nd Lam constant     lambda =   1.030453E+011 (N/m^2)
 Longitudinal velocity     cL =   4.199297E+003 m/s
- wavelength < 1/5 specimen lateral direction
 Shear velocity            cS =   2.969351E+003 m/s
```

```
GiD Name   = WATER
ATILA Name = M0002

 Bulk Modulus              K =   2.220000E+009 (N/m^2)         - K > 0
 Density                 rho =   1.000000E+003 (kg/m^3)
 Sound velocity           cL =   1.489966E+003 m/s

GiD Name   = GRAPHITE_EPOXY_COMP
ATILA Name = M0003

 Young's Modulus           E =   3.880000E+010 (N/m^2)         - E > 0
 Poisson ratio            nu =   3.000000E-001                 - -1 < nu < 1/2
 Density                 rho =   1.500000E+003 (kg/m^3)
 Bulk Modulus              K =   3.233333E+010 (N/m^2)         - K > 0
 Shear Modulus             G =   1.492308E+010 (N/m^2)         - G > 0
 1st Lam constant        mu =   1.492308E+010 (N/m^2)         - mu = G
 2nd Lam constant     lambda =   2.238462E+010 (N/m^2)
 Quality factor            Q =   4.217391E-001 m/s
 Longitudinal velocity    cL =   4.460654E+003 m/s
- wavelength < 1/5 specimen lateral direction
 Shear velocity           cS =   3.154159E+003 m/s
 Loss Modulus             E" =   9.200000E+010 (N/m^2)         - E" > 0
 Loss Poisson ratio      nu" =  -3.000000E-002
- -E"(1+nu)/E < nu" < (1/2-nu)/E

GiD Name   = WASHER_NUT_MASS
ATILA Name = M0004

 Young's Modulus           E =   1.080000E+011 (N/m^2)         - E > 0
 Poisson ratio            nu =   3.610000E-001                 - -1 < nu < 1/2
 Density                 rho =   4.431700E+004 (kg/m^3)
 Bulk Modulus              K =   1.294964E+011 (N/m^2)         - K > 0
 Shear Modulus             G =   3.967671E+010 (N/m^2)         - G > 0
 1st Lam constant         mu =   3.967671E+010 (N/m^2)         - mu = G
 2nd Lam constant     lambda =   1.030453E+011 (N/m^2)
 Longitudinal velocity    cL =   1.338128E+003 m/s
- wavelength < 1/5 specimen lateral direction
 Shear velocity           cS =   9.461993E+002 m/s

GiD Name   = PMN-30PT
```

```
ATILA Name = M0005

 Density                       =   8.038000E+003 (kg/m^3)
 s11E                          =   5.200000E-011 (m^2/N)
 s12E                          =  -1.890000E-011 (m^2/N)
 s13E                          =  -3.110000E-011 (m^2/N)
 s22E                          =   5.200000E-011 (m^2/N)
 s23E                          =  -3.110000E-011 (m^2/N)
 s33E                          =   6.770000E-011 (m^2/N)
 s44E                          =   1.400000E-011 (m^2/N)
 s55E                          =   1.400000E-011 (m^2/N)
 s66E                          =   1.520000E-011 (m^2/N)
 d15                           =   1.910000E-010 (m^2/N)
 d24                           =   1.910000E-010 (m^2/N)
 d31                           =  -9.210000E-010 (m^2/N)
 d32                           =  -9.210000E-010 (m^2/N)
 d33                           =   1.981000E-009 (m^2/N)
 E11T/E0                       =   3.600000E+003
 E22T/E0                       =   3.600000E+003
 E33T/E0                       =   7.800000E+003
 E11S                          =   2.926931E-008 (F/m)
 E22S                          =   2.926931E-008 (F/m)
 E33S                          =   1.104263E-008 (F/m)
 Mechanical losses             =   1.000000E-002
 Dielectric losses             =   3.700000E-003
```

A.2 [011] crystal baseline rectangular cymbal array

This material data table is from the [011] poled PMN-29PT baseline rectangular cymbal array model.

```
Lookup table for Material Names and Properties
 (some properties are not printed when equal to zero)

GiD Name   = TITANIUM
ATILA Name = M0001

 Young's Modulus             E =   1.080000E+011 (N/m^2)         - E > 0
 Poisson ratio              nu =   3.610000E-001                 - -1 < nu < 1/2
```

```
 Density                  rho =   4.500000E+003 (kg/m^3)
 Bulk Modulus               K =   1.294964E+011 (N/m^2)         - K > 0
 Shear Modulus              G =   3.967671E+010 (N/m^2)         - G > 0
 1st Lam constant          mu =  3.967671E+010 (N/m^2)         - mu = G
 2nd Lam constant      lambda =  1.030453E+011 (N/m^2)
 Longitudinal velocity     cL =   4.199297E+003 m/s
- wavelength < 1/5 specimen lateral direction
 Shear velocity            cS =   2.969351E+003 m/s

GiD Name   = WATER
ATILA Name = M0002

 Bulk Modulus               K =   2.220000E+009 (N/m^2)         - K > 0
 Density                  rho =   1.000000E+003 (kg/m^3)
 Sound velocity            cL =   1.489966E+003 m/s

GiD Name   = GRAPHITE_EPOXY_COMP
ATILA Name = M0003

 Young's Modulus            E =   3.880000E+010 (N/m^2)         - E > 0
 Poisson ratio             nu =   3.000000E-001                 - -1 < nu < 1/2
 Density                  rho =   1.500000E+003 (kg/m^3)
 Bulk Modulus               K =   3.233333E+010 (N/m^2)         - K > 0
 Shear Modulus              G =   1.492308E+010 (N/m^2)         - G > 0
 1st Lam constant          mu =  1.492308E+010 (N/m^2)         - mu = G
 2nd Lam constant      lambda =  2.238462E+010 (N/m^2)
 Quality factor             Q =   4.217391E-001 m/s
 Longitudinal velocity     cL =   4.460654E+003 m/s
- wavelength < 1/5 specimen lateral direction
 Shear velocity            cS =   3.154159E+003 m/s
 Loss Modulus              E" =   9.200000E+010 (N/m^2)         - E" > 0
 Loss Poisson ratio       nu" =  -3.000000E-002
- -E"(1+nu)/E < nu" < (1/2-nu)/E

GiD Name   = 011_PMNT29_APL90
ATILA Name = M0004

 Density                      =   8.090000E+003 (kg/m^3)
 s11E                         =   1.800000E-011 (m^2/N)
 s12E                         =  -3.110000E-011 (m^2/N)
```

```
 s13E                         =   8.400000E-012 (m^2/N)
 s22E                         =   1.120000E-010 (m^2/N)
 s23E                         =  -6.189000E-011 (m^2/N)
 s33E                         =   4.962000E-011 (m^2/N)
 s44E                         =   1.492000E-011 (m^2/N)
 s55E                         =   6.940000E-011 (m^2/N)
 s66E                         =   1.304000E-011 (m^2/N)
 d15                          =   1.188000E-009 (m^2/N)
 d24                          =   1.670000E-010 (m^2/N)
 d31                          =   6.100000E-010 (m^2/N)
 d32                          =  -1.883000E-009 (m^2/N)
 d33                          =   1.020000E-009 (m^2/N)
 E11T/E0                      =   3.564000E+003
 E22T/E0                      =   1.127000E+003
 E33T/E0                      =   4.033000E+003
 E11S                         =   1.121998E-008 (F/m)
 E22S                         =   8.109441E-009 (F/m)
 E33S                         =   2.718112E-009 (F/m)
 Mechanical losses            =   1.000000E-002
 Dielectric losses            =   3.700000E-003

GiD Name   = STUD_WASHER_MASS
ATILA Name = M0005

 Young's Modulus            E =   1.080000E+011 (N/m^2)         - E > 0
 Poisson ratio             nu =   3.610000E-001                 - -1 < nu < 1/2
 Density                  rho =   4.431700E+004 (kg/m^3)
 Bulk Modulus               K =   1.294964E+011 (N/m^2)         - K > 0
 Shear Modulus              G =   3.967671E+010 (N/m^2)         - G > 0
 1st Lam constant          mu =  3.967671E+010 (N/m^2)         - mu = G
 2nd Lam constant      lambda =  1.030453E+011 (N/m^2)
 Longitudinal velocity     cL =   1.338128E+003 m/s
- wavelength < 1/5 specimen lateral direction
 Shear velocity            cS =   9.461993E+002 m/s
```

Appendix B

Experimental measurements & slotted cymbals

B.1 Introduction

The slotted cymbal offers a possible modification to the [001] poled single-crystal benchmark cymbal array, as it is supposed to increase cymbal displacement without greatly reducing generative force. Previous literature on this design modification was discussed in Chapter 1. To study the implications of this, individual cymbal transducers were fabricated for experimental measurement of their electrical impedance and displacement characteristics. FEA models of the fabricated cymbals were made to see if the predicted results agreed with experiment. Finally, an array model of the slotted cymbal design was made to see if it would predict improved array performance.

B.1.1 Fabricated cymbals

Two single crystal disks of [001] poled PMN-30PT, poled through the thickness dimension were electroded. They were then bonded with a thin conductive epoxy layer to two titanium cymbal caps with titanium studs attached to them. Both can be seen in Fig. B.1. The caps were designed to be fabricated with similar dimensions to the benchmark cymbal laid out in Chapter 3. Both were stamped, and the slotted cymbal had 24 radial slots cut into it.

As the accuracy of the fabrication process wasn't known, caliper measurements of the cymbal cap dimensions were taken. These measured dimensions were used to create $^1/_8$ symmetry ATILA models of the two cymbal designs. The models used the same 0.8 ϕ mesh criteria described in Chapter 3.

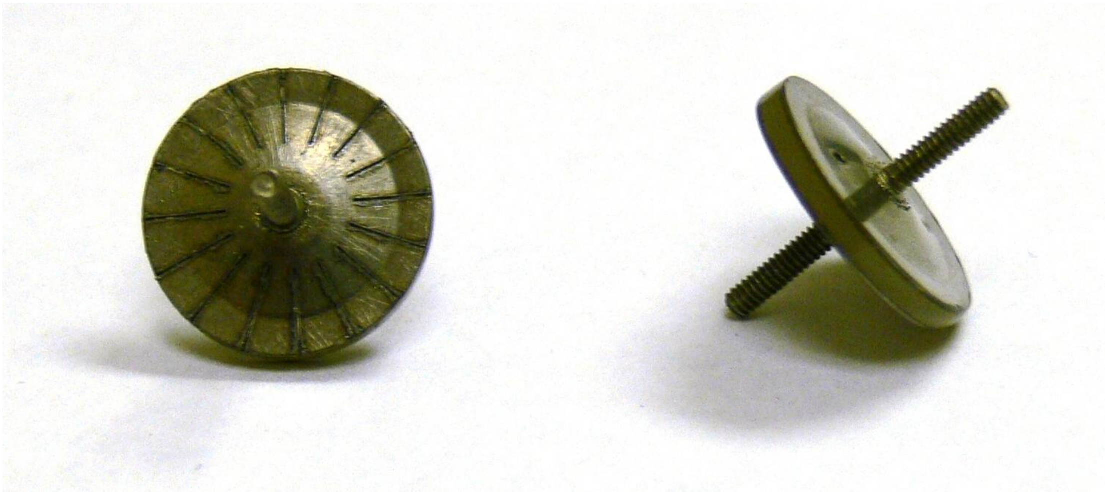

Figure B.1. A picture of fabricated slotted (left) and ‘full’ (right) cymbals.

diameter	ϕ
d_c	0.045 ϕ
r_1	0.114 ϕ
r_2	0.374 ϕ
t_c	0.020 ϕ
t_x	0.079 ϕ
stud length	0.492 ϕ
stud diameter	0.110 ϕ

Table B.1. Normalized dimensions for the measured full cymbal. Dimensions that differ from the benchmark cymbal are highlighted in red.

B.1.1.1 ‘Full’ cymbal

The use of the word full distinguishes an unmodified cymbal cap from one that has been slotted. The dimensions used in the model of the fabricated full cymbal are reported in Table B.1. There were several dimensions that differed from those laid out in Chapter 3. These are highlighted in red to distinguish them from the benchmark cymbal discussed before.

B.1.1.2 Slotted cymbal

The slotted cymbal shown in Fig. B.1 was modeled similar to the fabricated full cymbal model described above. The model is shown in Fig. B.2. There were 24 slots with the geometry shown in Fig. B.3 and the normalized dimensions reported in Table B.2. While the real slots were cut with a constant width, it was much easier to model in GiD with an angular slot. As such, the measured width of the slots was used as an average width of angular wedges. These wedges were the modeled version of the slots.

Originally the slots crossed the symmetry planes of the model, so that four equal sections of material were left. This was found to be problematic in solution of the problem, so they were rotated to the locations seen in Fig. B.2[1], leaving two half-sections at the symmetry planes.

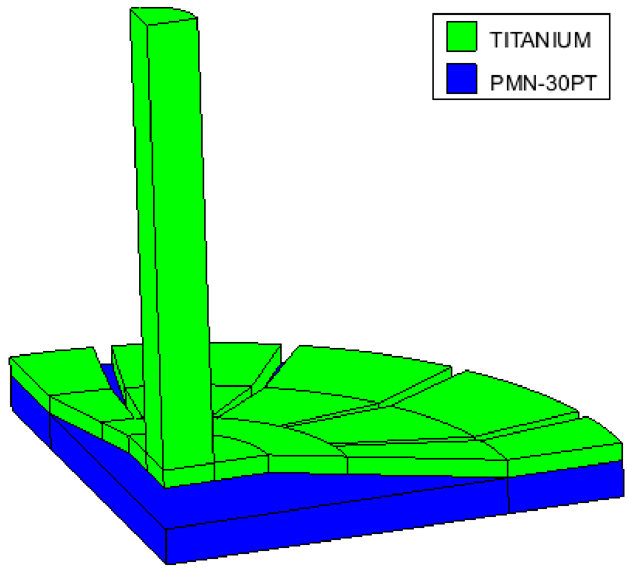

Figure B.2. An isometric view of the slotted cymbal model. The view mode is material colors.

diameter	ϕ
d_c	0.045 ϕ
r_1	0.114 ϕ
r_2	0.374 ϕ
t_c	0.020 ϕ
t_x	0.079 ϕ
stud length	0.492 ϕ
stud diameter	0.110 ϕ
slot length	0.300 ϕ
avg. slot width	0.013 ϕ

Table B.2. Normalized dimensions for the measured slotted cymbal

[1]It was never clear why this issue occurred, and it could have been the result of a mistake in modeling. Nevertheless, it is important to note that the geometry shown in Fig. B.3 was demonstrated to model the problem correctly.

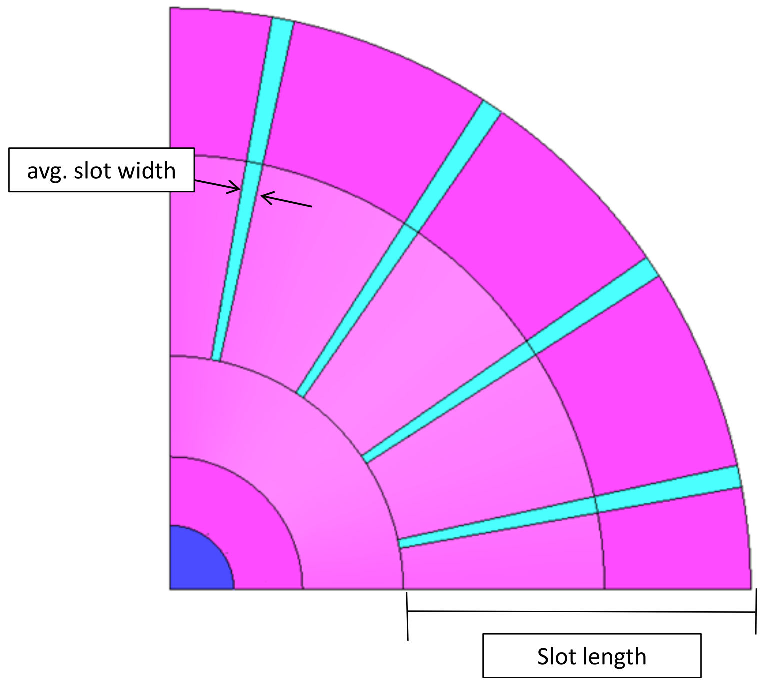

Figure B.3. A view of the top side of the slotted cymbal, showing the slot dimensions.

B.1.1.3 Slotted cymbal array

For the array results, the model was adapted from the original benchmark cymbal array of Chapter 3. Slots were added to the benchmark cymbals to see their effect on the array performance. This means that for the array results presented in this chapter, the slotted cymbals have the dimensions of the benchmark cymbal and the slots have the dimensions of the fabricated slotted cymbal. This was done for fair comparison of array results against the known benchmark array.

B.2 Experimental setup & measurements

B.2.1 Impedance sweep (in-air)

The magnitude impedance spectrum of the two fabricated cymbals was taken with an Agilent 4294A Precision Impedance Analyzer. The output was sent to a laptop running Matlab for data collection. In order to not affect the impedance with the measurement setup, two pogo pins were used for electrical connection as shown in Fig. B.4. The pogo pins were connected at the flange of the cymbal, where the mechanical impedance will be the highest. As such, the force of the pogo pins should affect the measurement least in this area.

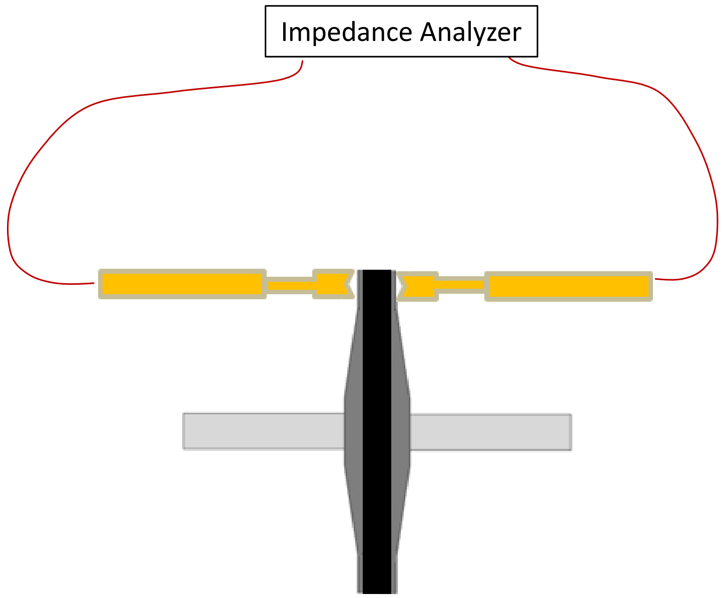

Figure B.4. A cartoon of the pogo pin connection to the cymbal transducer for impedance measurement. Notice the location of the terminals at the flange of the cymbal. This cartoon is not to scale.

B.2.2 LDV displacement measurement (in-air)

In order to properly compare the displacement results of the model and the fabricated cymbal, it was desired to obtain displacement data for the stud of the cymbal. To do this, a laser Doppler vibrometer (LDV) was used to scan the tip of the cymbal stud. A Polytec OFV-505 Sensor Head laser was connected to a Polytec OFV 5000 Vibrometer Controller to output the velocity of the stud at a given frequency. Velocity, voltage, and frequency data were then output to Matlab for data collection.

The velocity measurement from the laser is converted to displacement in Matlab using the angular frequency. This displacement was then normalized by the voltage of the drive for comparison with the displacement per volt results from the FEA model. This was done because an amplifier wasn't used, and the voltage varied across the spectrum with the varying impedance of the transducer. This can be seen in Fig. B.5. The two dips seen in the fabricated full cymbal will be discussed later.

Setting up the laser measurement was somewhat more difficult than the impedance measurement due the requirement that the laser have an on-axis view of one of the studs. Again pogo pins were used to make electrical connection, as to not influence the measurement. A cartoon of the setup can be seen in Fig. B.6. Care was taken to align the stud of the cymbal with the laser, but this was likely one of the largest sources of error in the measurement.

A comparison of the first electrical resonance frequency for each cymbal in each setup is reported in Table B.3[2]. It can be seen that the frequencies agree quite well, therefore the two different setups were comparable.

Cymbal	$\lvert Z_E \rvert\ f_r$	LDV f_r
Fabricated full	1.12	1.13
Fabricated w/ slots	1.06	1.06

Table B.3. Normalized resonance frequencies for the fabricated cymbals under the two different measurement conditions.

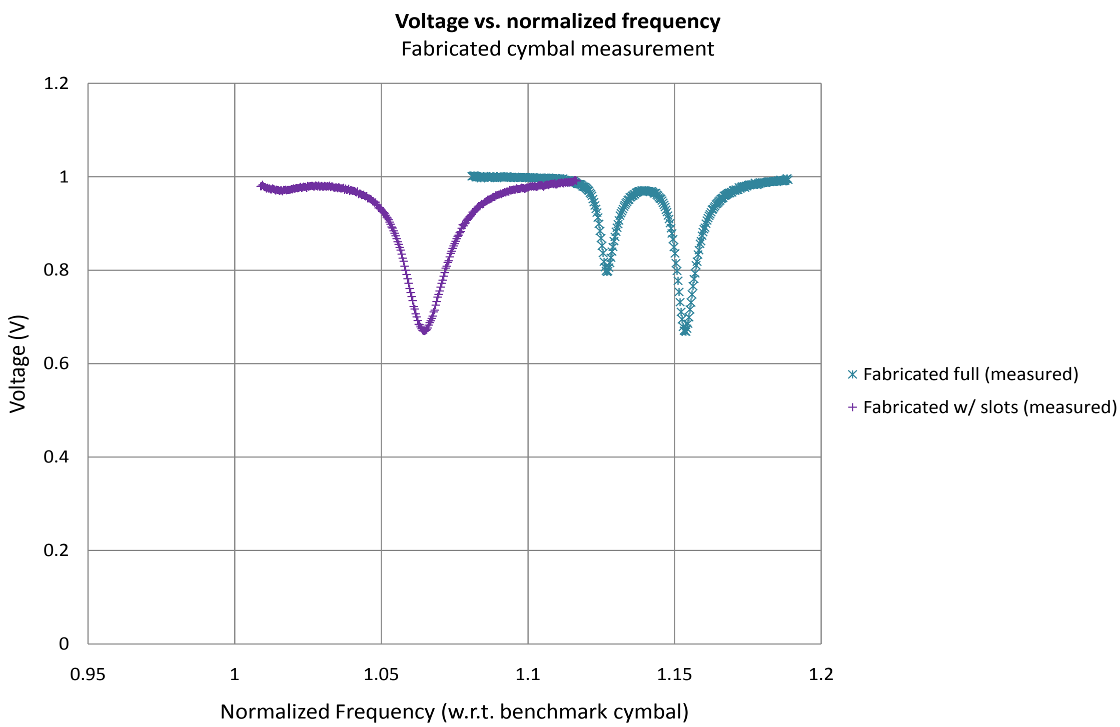

Figure B.5. A plot of voltage vs. normalized frequency for the two fabricated cymbals. This data was taken during LDV measurement.

[2]The f_r from the impedance spectrum was the frequency of the first impedance minima. The f_r from the LDV was the first frequency of displacement maxima.

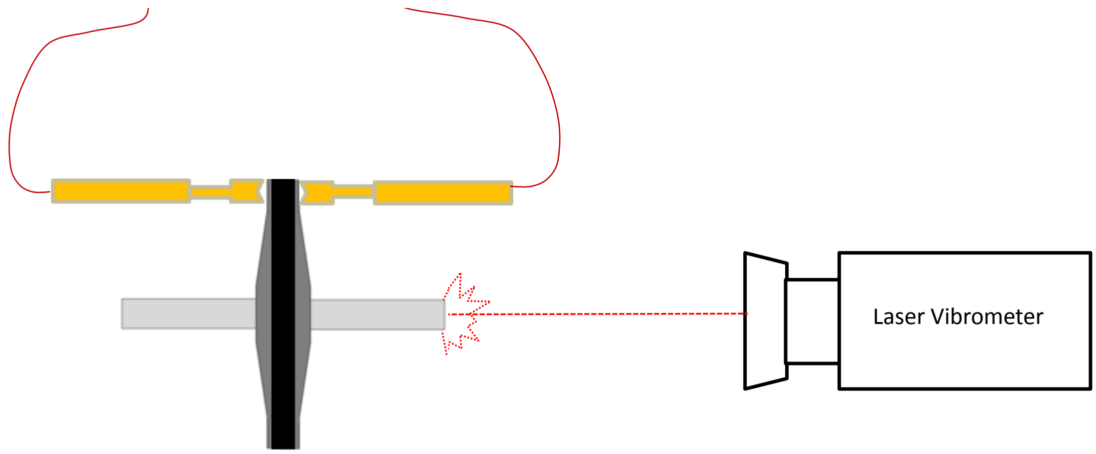

Figure B.6. A cartoon of the laser setup for the LDV measurement of the cymbal transducer. This cartoon is not to scale.

B.3 Results

B.3.1 Individual cymbal results: model vs. measured

B.3.1.1 Impedance

Both measured and modeled results for the magnitude impedance of the fabricated cymbals can be seen in Fig. B.7. A view in the area of electrical resonance is shown in Fig. B.8. In both figures, it can be seen that the model under-predicts the impedance of the actual transducer, but predicts the resonance frequency quite well. Calculation of the effective coupling of the fabricated cymbals was complicated by the split peaks in the full cymbal, but it can be seen by the spacing of f_r and f_a that the coupling was slightly lower for the measured data.

To better understand the differences between model and measured impedance, normalized plots of the resistance vs. frequency and reactance vs. freqeuncy can be seen in Fig. B.9 & B.10, respectively. Notice that the vertical scale is logarithmic for resistance and linear for reactance.

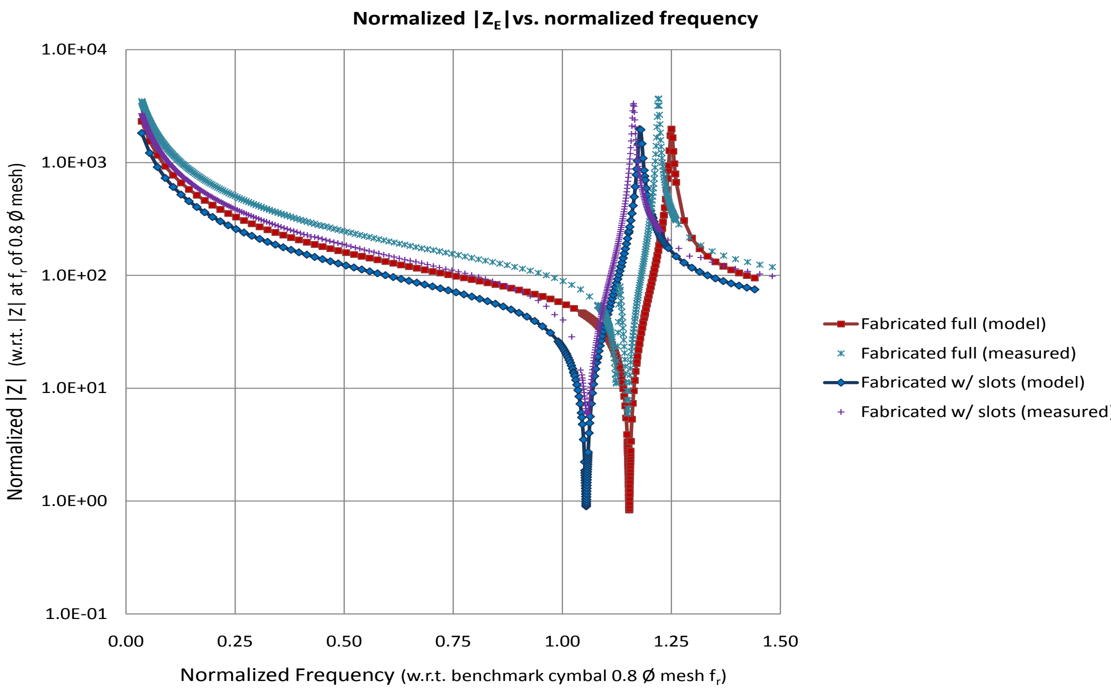

Figure B.7. A normalized plot of $|Z_E|$ vs. frequency for the modeled fabricated cymbal w/ and w/o slots, and the measured impedance spectrum for the fabricated cymbals.

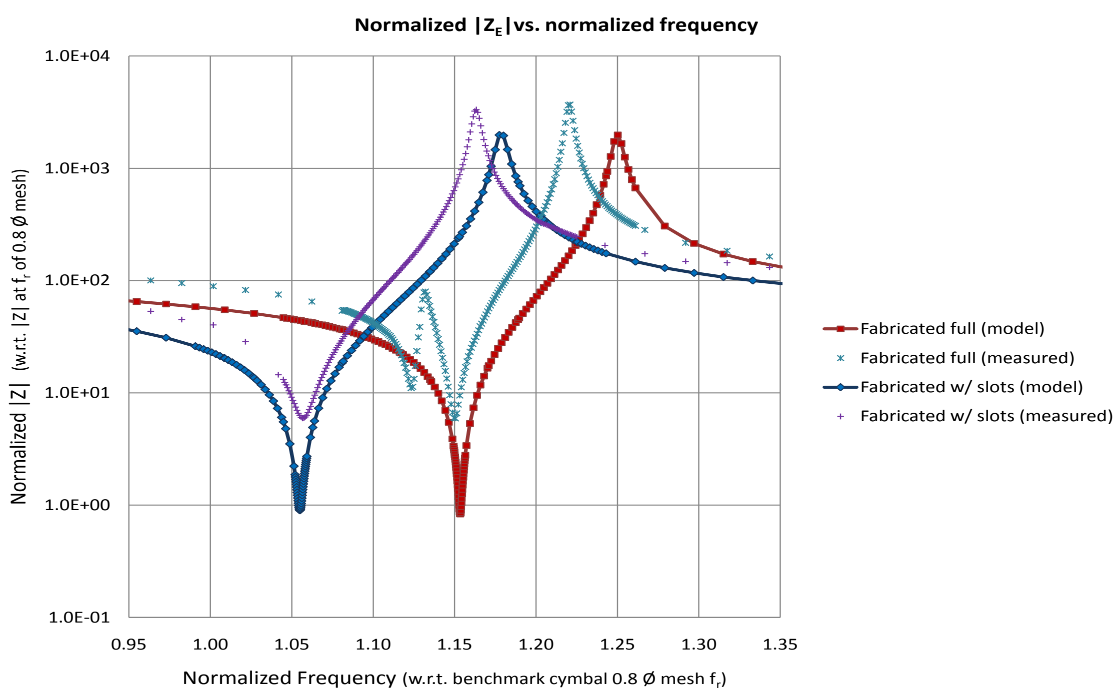

Figure B.8. A closer view of $|Z_E|$ vs. frequency for the modeled fabricated cymbal w/ and w/o slots, and the measured impedance spectrum for the fabricated cymbals.

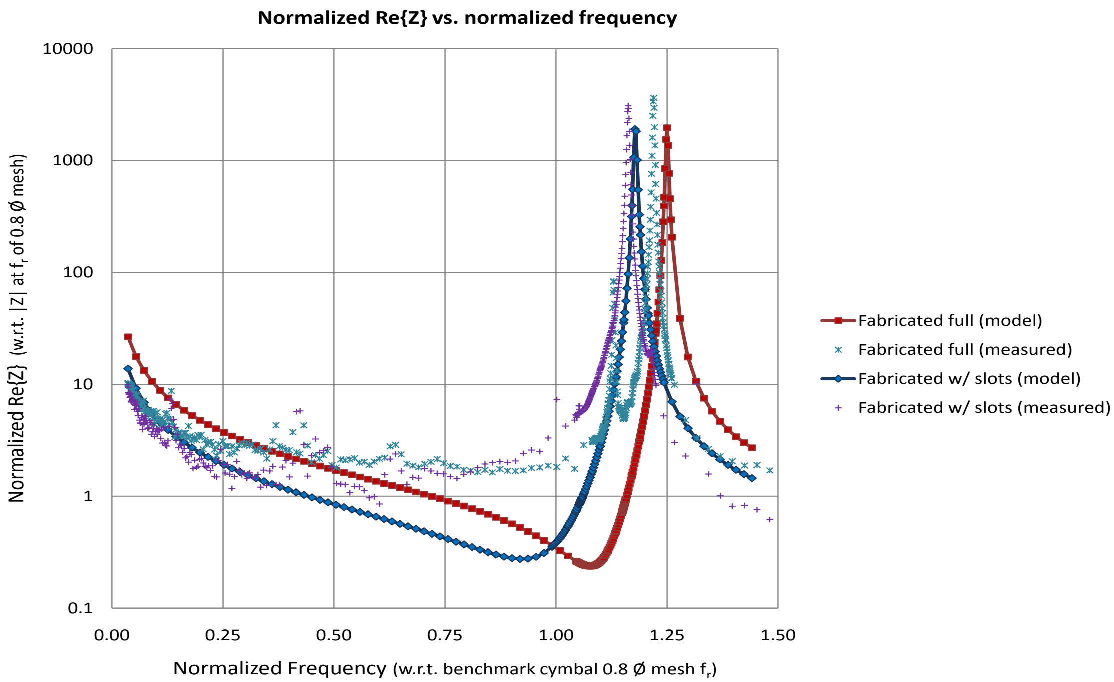

Figure B.9. A normalized plot of $Re\{Z\}$ vs. frequency for the modeled fabricated cymbal w/ and w/o slots, and the measured impedance spectrum for the fabricated cymbals.

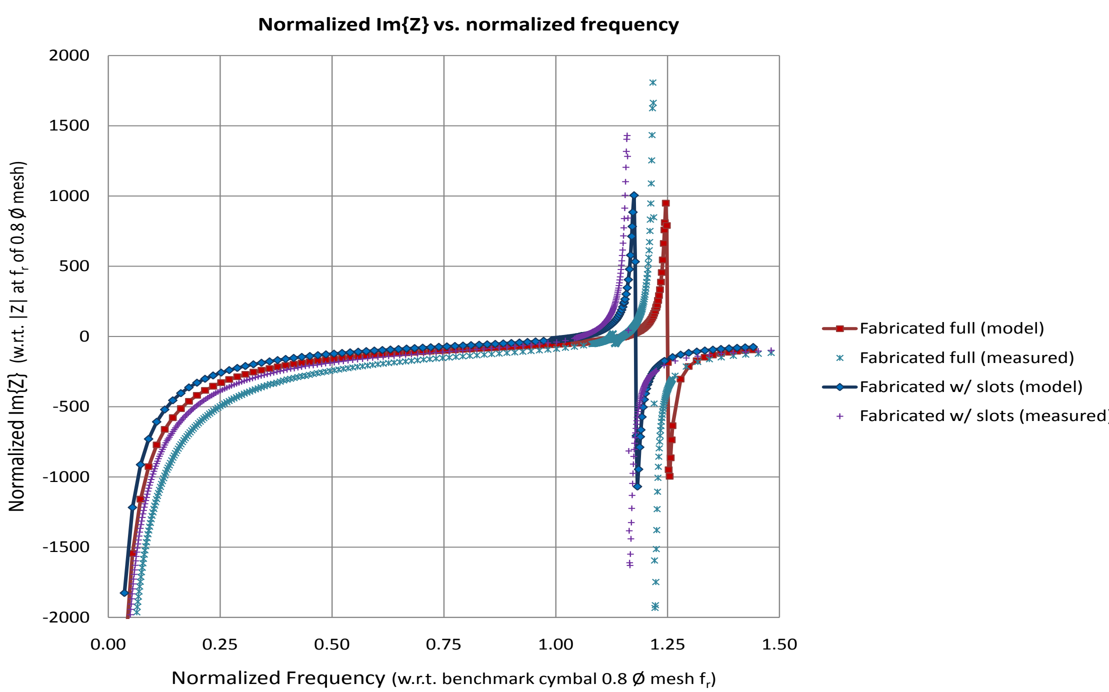

Figure B.10. A normalized plot of $Im\{Z\}$ vs. frequency for the modeled fabricated cymbal w/ and w/o slots, and the measured impedance spectrum for the fabricated cymbals.

B.3.1.2 Displacment

A normalized plot of displacement versus frequency in-air can be seen in Fig. B.11. The benchmark cymbal of Chapter 3, along with a slotted version of it mentioned in Section B.1.1.3, are shown for reference. It can be seen that the small dimensional changes in the fabricated cymbals (from the benchmark dimensions) affect the resonance frequency more than the displacement. A zoomed in view of the fabricated cymbals and their models is shown in Fig. B.12.

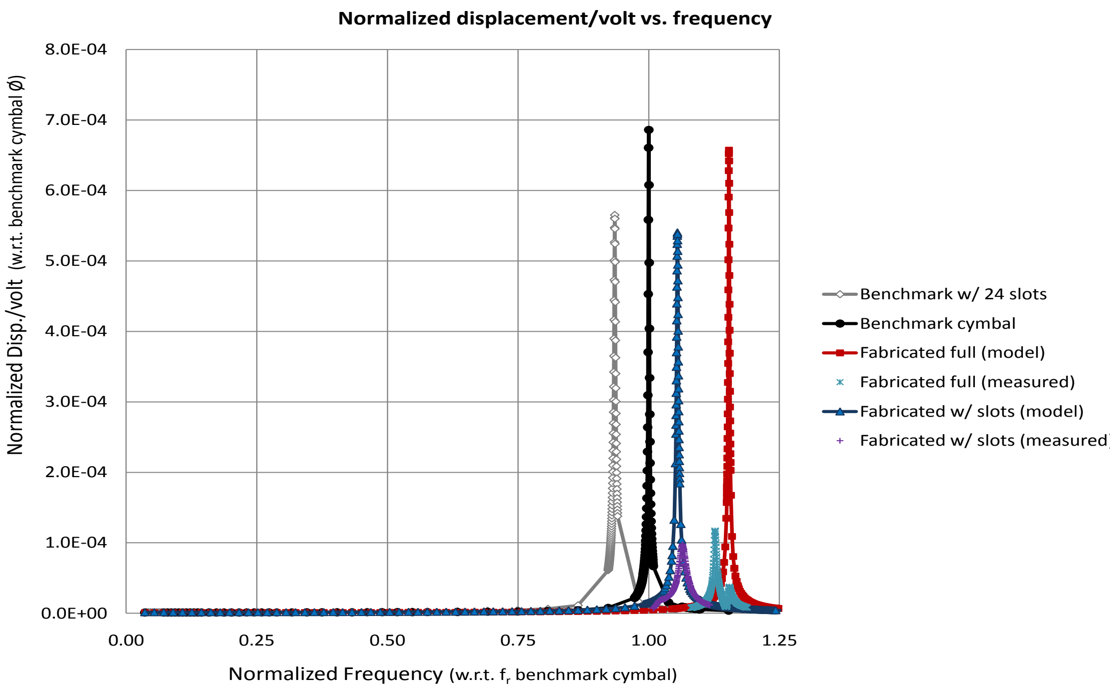

Figure B.11. A normalized plot of displacement vs. frequency for the modeled fabricated cymbal w/ and w/o slots, the benchmark cymbal w/ and w/o slots, and the measured LDV results for the fabricated cymbals.

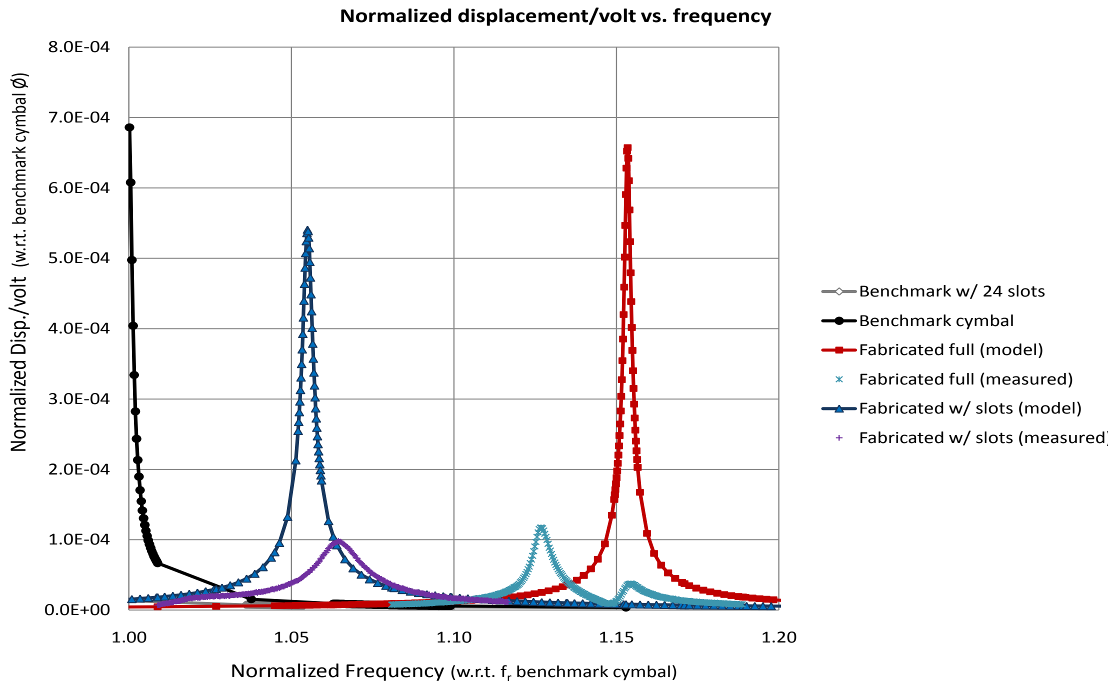

Figure B.12. A normalized plot of displacement vs. frequency for the fabricated cymbal w/ and w/o slots, the benchmark cymbal w/ and w/o slots, and the measured LDV results for the fabricated cymbals.

B.3.2 Array results: model only

Results for the benchmark array with slots in-water are shown in the Figs. B.13-B.15. A comparison of the coupling of the two arrays is shown in Table B.4.

Design	κ_{eff}
Benchmark array	0.55
Benchmark w/ 24 slots	0.57

Table B.4. Slotted cymbal κ_{eff} comparison.

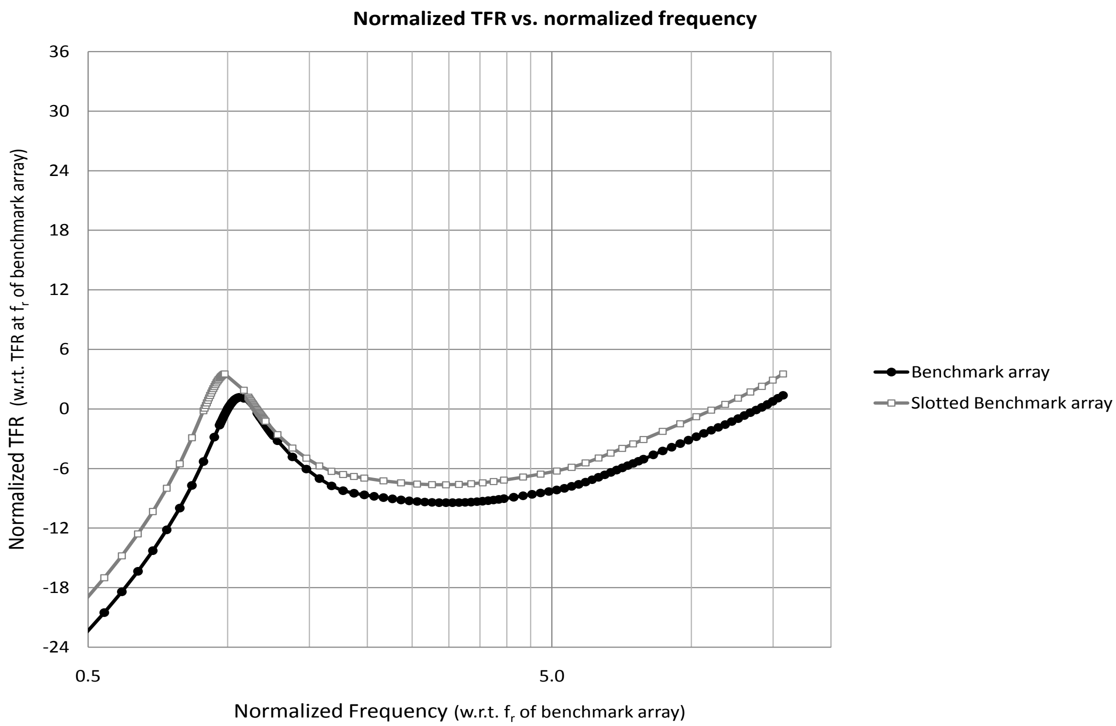

Figure B.13. A plot of TFR vs. frequency for both the benchmark array w/ and w/o 24 slots.

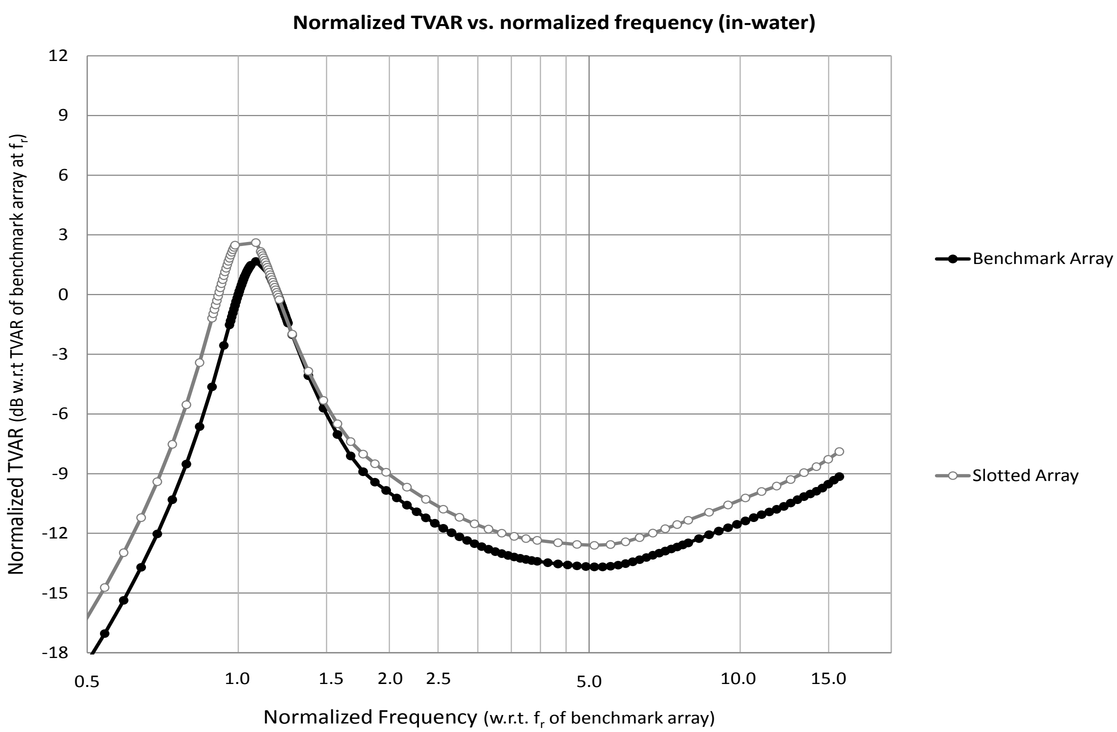

Figure B.14. A plot of $TVAR$ vs. frequency for both the benchmark array w/ and w/o 24 slots.

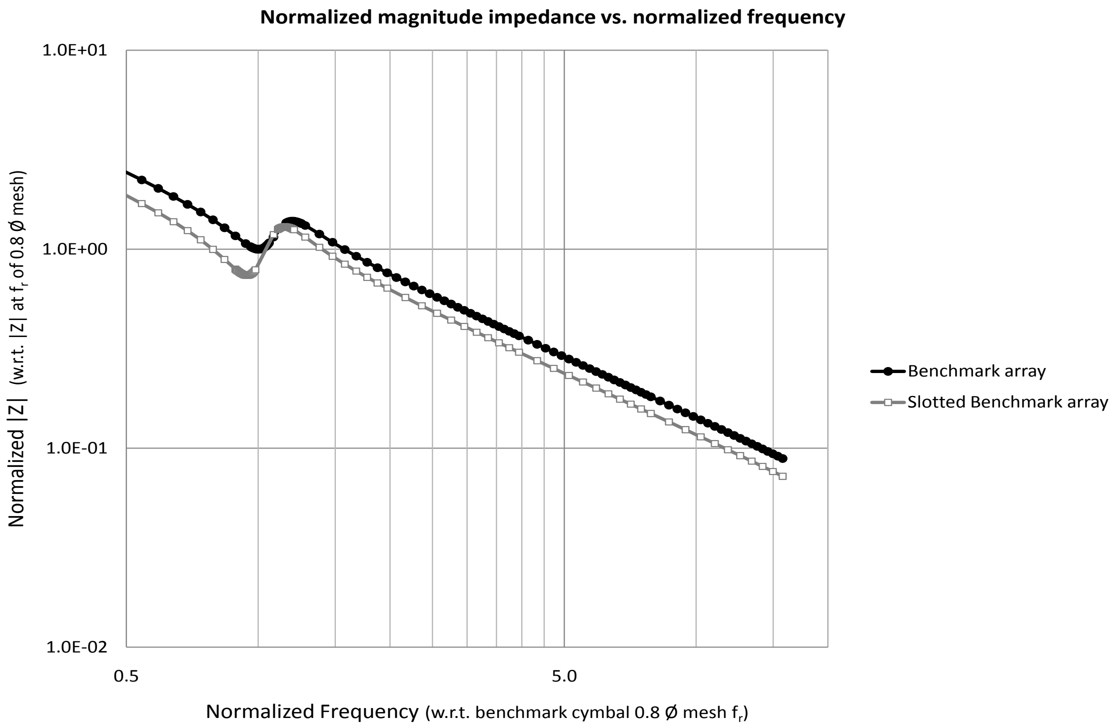

Figure B.15. A plot of $|Z_E|$ vs. frequency for both the benchmark array w/ and w/o 24 slots.

B.4 Discussion

B.4.1 Individual cymbal results

B.4.1.1 Impedance measurement

It was obvious from the impedance results that the model under-predicts the impedance of the fabricated transducer. Specifically, resistance is under-predicted in the area of resonance and reactance is under-predicted across the band. The under-prediction of resistance was expected, as laid out in Chapter 3. The reactance measurement was more surprising.

Because the reactance is primarily negative, under-prediction of the reactance means that the model is less capacitive than the fabricated transducer. This is due to the differences in electrical connection between the model and measurement. In the measurement setup, electrical connection was made to the caps, through the conductive epoxy, and then to the electrodes on the single-crystal disk. In the model, there are ideal electrodes on the single-crystal disk.

The main contributing factor to the under-prediction of capacitance is likely the lack of the conductive epoxy in the model. This material isn't an ideal conductor, and as such has a higher relative permittivity than the ideal electrode of the model[3]. This will add capacitance in the real-life measurement that has not been accounted for in the model.

[3]Because the model electrode has no thickness, it could be considered to be an ideal conductor with a relative permitivitty of zero.

B.4.1.2 Split peaks in the 'full' cymbal

The fabricated full cymbal clearly shows split modes near its resonance. This is a known concern with cymbals, and was discussed previously in Chapter 1. It is likely due to dimensional or bonding differences from one side of the cap to the other.

It is interesting to note how 'clean' the slotted cymbal spectrum is in comparison. While the measurement of two cymbals isn't statistically significant, it is possible that by slotting the cymbal cap, it becomes less sensitive to differences in geometry. The stress relief mechanism could be enforcing a more uniform response on the device. It would be interesting to study this further on a larger scale.

B.4.1.3 Effects of slotting

Both the FEA models and the measured cymbals show that the slots used for these caps reduce displacement and decrease the resonance frequency of the transducer. The normalized displacement, resonance frequency, and change from the full cymbal are reported in Table B.5.

Cymbal	f_r	slot effect	norm. disp.	slot effect
Benchmark	1.00		6.86×10^{-4}	
Benchmark w/ slots	0.94	-6%	5.61×10^{-4}	-18%
Fabricated full (model)	1.15		6.52×10^{-4}	
Fabricated w/ slots (model)	1.05	-9%	5.36×10^{-4}	-18%
Fabricated full (measured)	1.13		1.17×10^{-4}	
Fabricated w/ slots (measured)	1.06	-6%	0.98×10^{-4}	-16%

Table B.5. Comparison of normalized resonance frequency, displacement, and the effect of slotting for each pair. The first displacement peak of the full cymbal was used for this table.

B.4.2 Array results

The array results show a similar reduction in resonance frequency of approximately 6% when slots are added to the benchmark cymbals. Conversely to displacement, however, there is an increase in TFR with slotting. While this is reminiscent of the converse trend seen with cap depth in Chapter 5, it is doubtful that the same mechanical impedance hypothesis applies. In this case, the cymbals must behave differently under the large load of the water. The slots reduce the amount of tangential stress that can build up in the transducer, making them more effective (i.e. less lossy) under loading.

The $TVAR$ of the two arrays is seen to be approximately equal across the band, with an improvement of about 3 dB below resonance. This is due to the fact that while the TFR of the slotted array is higher, its impedance is lower. Without the large increase in coupling that was seen with the rectangular cymbal arrays in Chapter 4, the $TVAR$ does not improve much. The improvement that is seen below resonance matches up with the increase in TFR seen below resonance.

B.4.3 Conclusions

B.4.3.1 Effects of slotting

It appears from the above results that slotting can improve array performance if unwanted tangential stresses are present in the transducer. It would be interesting to see if a different slot design could further improve array performance. Previous reports contend that displacement in cymbals can be improved by slotting [63, 64], without effecting generative force. This suggests that increased output should be possible with a different slot design, as incremental improvement has already been predicted despite *decreased* displacement.

It is unclear if slotting would be beneficial in the rectangular cymbal design. If there is not a significant transverse stress in the cap, then slotting may not increase output in the array. However, it has been shown that resonance frequency can be reduced without reducing output by adding slots to the circular cymbal. This means that slotting could possibly be used to tune resonance frequency of an array downward without affecting output.

B.4.3.2 Modeling displacement

Clearly from the results of Fig. B.12, the FEA model significantly over predicts displacement of a cymbal transducer. Looking at the slotted cymbal resistance results[4] of Fig. B.8, it can be seen that the resistance in the area of resonance is under-predicted by a factor of approximately 6. This claim is tempered by the fact that this resistance measurement is quite hard to make. The low level of resistance, and the high reactance across most of the band make accurate resistance measurements difficult. However, it is the opinion of the author that the discrepancy between measured and modeled resistance is a failure of the model, and not of the measurement.

Looking at the displacement results, displacement is over-predicted by a factor of approximately 5.5 at resonance. Values for the normalized resonance frequency, displacement, and resistance for the slotted cymbal model and measurement are detailed in Table B.6.

Cymbal	$\mathbf{f_r}$	**displacement**	**R**
Model w/ slots	1.05	5.41×10^{-4}	0.9
Fabricated w/ slot	1.06	0.98×10^{-4}	6.0

Table B.6. Comparison of normalized resonance frequency, displacement, and resistance of the slotted cymbal model and measurement.

To make a connection between these two, let us consider an equivalent circuit model of a simple harmonic oscillator (SHO). The mechanical impedance of the oscillator is given by:

$$Z_{mechanical} = \frac{F}{v} = \frac{F}{j\omega d} = R + j\omega m + \frac{1}{j\omega C}$$

[4]The slotted cymbal results are being considered due to the fact that the spectrum is 'cleaner' without the split peaks of the fabricated full cymbal

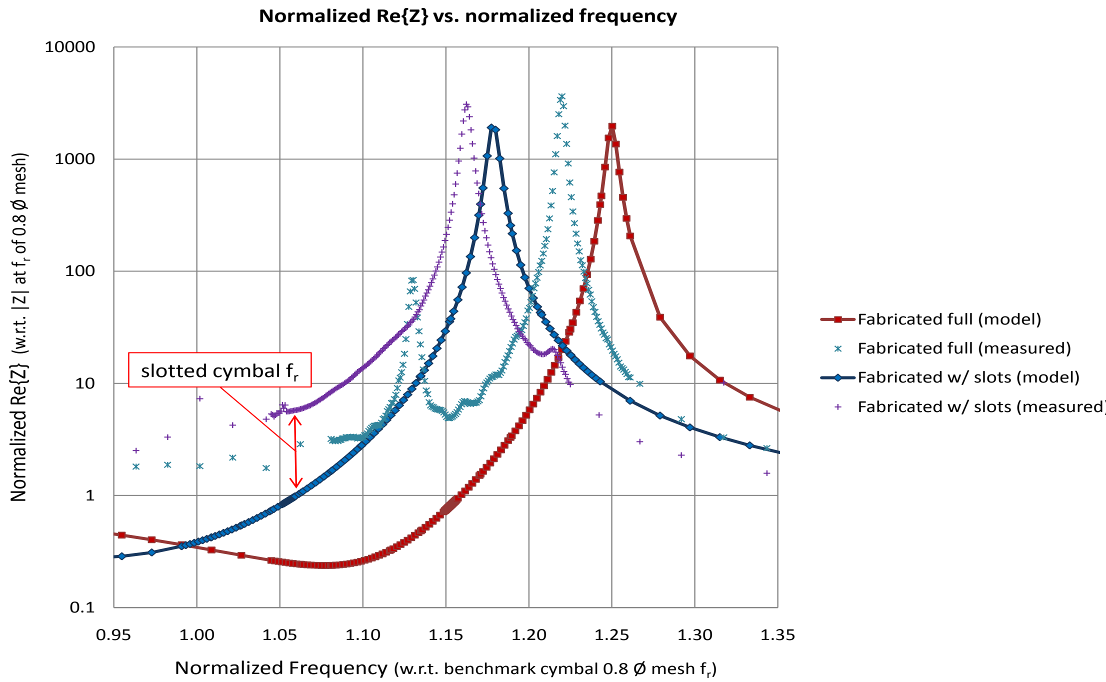

Figure B.16. A normalized plot of $Re\{Z\}$ vs. frequency for the modeled fabricated cymbal w/ and w/o slots, and the measured impedance spectrum for the fabricated cymbals.

where F is the force, v is the velocity, d is the displacement, R is the resistance, m is the mass, and C is the compliance. At resonance, the impedance reduces to the resistance, giving the following approximation for the displacement in our transducer at resonance:

$$d \approx \frac{F}{j\omega R} \tag{B.1}$$

Assuming the force (analogous to voltage in our case) stays constant, it can be seen from Eq. (B.1) that we would expect a 6-fold reduction in displacement for a 6-fold increase in resistance. This SHO approximation should hold quite well for a resonant transducer like the cymbal, and explains why the displacement modeling of the transducer is inaccurate.

The resistance of the model could be improved with more accurate loss properties for the materials used. Additionally, inclusion of the epoxy layer would improve the resistance prediction. However, it is unlikely that either of these will influence array results significantly, as the resistance of an array will be dominated by the fluid loading.

Bibliography

[1] Wang, F., L. Luo, D. Zhou, X. Zhao, and H. Luo (2007) "Complete set of elastic, dielectric, and piezoelectric constants of orthorhombic $0.71Pb(Mg_{1/3}Nb_{2/3})O_3$-$0.29PbTiO_3$ single crystal," *Applied Physics Letters*, **90**(212903).

[2] Newnham, R. E. and A. Dogan, "Metal-electroactive ceramic composite transducer," United States Patent #5,729,077, filed December 15, 1995, published March 17, 2008.

[3] Hunt, F. V. (1982) *Electroacoustics*, The Acoustical Society of America.

[4] Wente, E. C., "Telephone-transmitter," United States Patent #1,333,744, filed December 20, 1916, published March 16, 1920.

[5] (1941) "Occasional Papers, No. 73: The History and Developments of Sounding, With Particular Reference to Precise Supersonic-Echo Sounding Methods as Recently Developed in the U.S. Engineer Department," United States Government Printing Office, pp. 1–92, this article was prepared under the direction of Lt. Col. H.B. Vaughan, Jr., Corps of Engineers, United States Army.

[6] Ørsted, H. C. (1820) "Experiments on the Effect of a Current of Electricity on the Magnetic Needle," *Annals of Philosophy*, **16**, pp. 273–276.

[7] Sturgeon, W. (1824) "III. Improved Electro-Magnetic Apparatus," in *Transactions of the Society instituted at London for the encouragement of arts, manufacturers, and commerce, Volume 43*, T. & J.B. Flindell, pp. 37–52.

[8] Morse, S. F. B., "Improvement in the Mode of Communicating Information by Signals by the Application of Electro-magnetism," United States Patent #1,647, published June 20, 1840.

[9] Bell, A., "Improvement in Telegraphy," United States Patent #174,465, filed February 14, 1876, published March 7, 1876.

[10] Siemens, E. W., "Magneto-Electric Apparatus," United States Patent #149,797, published April 14, 1874.

[11] Fessenden, R. A., "Signaling by Sound and Other Longitudinal Elastic Impulses," United States Patent #1,108,895, filed January 10, 1914, published September 1, 1914.

[12] Rolt, K. D. (1994) "The Fessenden oscillator: History, electroacoustic model, and performance estimate," *The Journal of the Acoustical Society of America*, **95**(5), pp. 2832–2832. URL `http://link.aip.org/link/?JAS/95/2832/3`

[13] JOULE, J. P. (1847) "XVII. On the effects of magnetism upon the dimensions of iron and steel bars," *Philosophical Magazine Series 3*, **30**(199), pp. 76–87.

[14] SHERMAN, C. H. and J. L. BUTLER (2008) *Transducers and Arrays for Underwater Sound*, Springer.

[15] "TERFENOL-D® data sheet," Etrema Products, Inc., www.etrema-usa.com.

[16] CLARK, A. E., J. B. RESTORFF, M. WUN-FOGLE, T. A. LOGRASSO, and D. L. SCHLAGEL (2000) "Magnetostrictive properties of body-centered cubic Fe-Ga and Fe-Ga-Al alloys," *Magnetics, IEEE Transactions on*, **36**(5), pp. 3238 –3240.

[17] PORTER, S. P. (2011) *A Design Approach for a Configurable High-Power Magnetostrictive Drive Made from Iron-Gallium Alloy (Galfenol)*, Master's thesis, The Pennsylvania State University.

[18] LANG, S. B. (1974) *Sourcebook of Pyroelectricity, Volume 2*, Gordon and Breach, Science Publishers, Inc.

[19] CADY, W. G. (1946) *Piezoelectricity*, McGraw-Hill Book Company, Inc.

[20] KATZIR, S. (2006) *The Beginning of Peizoelectricity*, Springer.

[21] THOMSON, W. (LORD KELVIN) "*209. Extracted from Nichol's "Cyclopedia of the Physical Sciences,*" second edition 1860," in *Mathematical and Physical Papers, Vol. I*, (1882) Cambridge: At the University Press, pp. 315–316.

[22] JAFFE, H. W. (1988) *Introductiopn to Crystal Chemistry*, Cambridge University Press.

[23] (1988) "IEEE Standard on Piezoelectricity," *ANSI/IEEE Std 176-1987*, Withdrawn Standard.

[24] CURIE, P-J. and P. CURIE "Crystal Physics - Development by Pressure of Polar Electricity in Hemihedral Crystals with Inclined Faces," in *Acoustics: Historical and Philosophical Development* (R. B. Lindsay, ed.), Benchmark Papers in Acoustics, Dowden, Hutchinson, & Ross, pp. 373–4, translated from *Compt. Rend. Acad. Sci. Paris*, **91**, 294 (1880) by R. B. Lindsay.

[25] R.B. LINDSAY *Acoustics: Historical and Philosophical Development*, Benchmark Papers in Acoustics, Dowden, Hutchinson, & Ross.

[26] KINGERY, W. D., H. K. BOWEN, and D. R. UHLMANN (1976) *Introduction to Ceramics, Second Edition*, John Wiley & Sons.

[27] VALASEK, J. (1921) "Piezo-Electric and Allied Phenomena in Rochelle Salt," *Phys. Rev.*, **17**(4), pp. 475–81.

[28] ——— (1922) "Piezo-electric Activity of Rochelle Salt Under Various Conditions," *Phys. Rev.*, **19**(5), pp. 478–91.

[29] JAFFE, B., W. COOK, and H. JAFFE (1971) *Piezoelectric Ceramics*, CBLS Publisher & Book Distributor.

[30] GRAY, R. B., "Transducer and Method of Making the Same," United States Patent #2,486,560, filed September 20, 1946, published November 1, 1949.

[31] Cross, L. E. and R. E. Newnham (1987) "History of Ferroelectrics," in *Ceramics and Civilization, Volume III, High Technology Ceramics - Past, Present, and Future*, The American Ceramic Society, Inc., pp. 289–305.

[32] Jaffe, B., R. S. Roth, and S. Marzullo (1954) "Piezoelectric Properties of Lead Zirconate-Lead Titanate Solid-Solution Ceramics," *J. Appl. Phys.*, **25**(6), pp. 809–10.

[33] Guo, R., L. E. Cross, S.-E. Park, B. Noheda, D. E. Cox, and G. Shirane (2000) "Origin of the High Piezoelectric Response in $PbZr_{1-x}Ti_xO_3$," *Phys. Rev. Lett.*, **84**(23), pp. 5423–5426.

[34] Haertling, G. H. (1999) "Ferroelectric Ceramics: History and Technology," *Journal of the American Ceramic Society*, **82**(4), pp. 797–818.
URL `http://dx.doi.org/10.1111/j.1151-2916.1999.tb01840.x`

[35] Schäufele, A. B. and K. Heinz Härdtl (1996) "Ferroelastic Properties of Lead Zirconate Titanate Ceramics," *Journal of the American Ceramic Society*, **79**(10), pp. 2637–2640.
URL `http://dx.doi.org/10.1111/j.1151-2916.1996.tb09027.x`

[36] Military Standard *Piezoelectric Ceramic Material and Measurements: Guidelines for Sonar Transducers*, under MIL-STD-1376B(SH) 24 February 1995. FSC 5845. Cancelled Standard.

[37] Wilson, O. B. (1988) *Introduction to Theory and Design of Sonar Transducers*, Peninsula Publishing.

[38] © Copyright of The Morgan Crucible Company plc and its affiliates, 2009. All rights reserved.
URL `http://www.morganelectroceramics.com/materials/piezoelectric/`

[39] Fett, T., D. Munz, and G. Thun (1999) "Tensile and bending strength of piezoelectric ceramics," *Journal of Materials Science Letters*, **18**, pp. 1899–1902, 10.1023/A:1006698724548.
URL `http://dx.doi.org/10.1023/A:1006698724548`

[40] Heywang, W., K. Lubitz, W. Wersing, and L. E. Cross (2008) "Relaxor Ferroelectrics," in *Piezoelectricity*, vol. 114 of *Springer Series in Materials Science*, Springer Berlin Heidelberg, pp. 131–155.

[41] Nomura, S., T. Takahashi, and Y. Yokomizo (1969) "Ferroelectric Properties in the System $Pb(Zn_{1/3}Nb_{2/3})O_3$-$PbTiO_3$," *Journal of the Physical Society of Japan*, **27**(1), pp. 262–262.
URL `http://jpsj.ipap.jp/link?JPSJ/27/262/`

[42] Kuwata, J., K. Uchino, and S. Nomura (1981) "Phase Transitions in the $Pb(Zn_{1/3}Nb_{2/3})O_3$-$PbTiO_3$ System," *Ferroelectrics*, **37**, pp. 579–582.

[43] Yamashita, Y. (1994) "Large Electromechanical Coupling Factors in Perovskite Binary Material System," *Japanese Journal of Applied Physics*, **33**(Part 1, No. 9B), pp. 5328–5331.
URL `http://jjap.jsap.jp/link?JJAP/33/5328/`

[44] Shrout, T. R., Z. P. Chang, N. Kim, and S. Markgraf (1990) "Dielectric behavior of single crystals near the (1-x) $Pb(Mg_{1/3}Nb_{2/3})O_3$-(x)$PbTiO_3$ morphotropic phase boundary," *Ferroelectrics Letters Section*, **12**, pp. 63–69.

[45] Park, S.-E. and T. R. Shrout (1997) "Ultrahigh strain and piezoelectric behavior in relaxor based ferroelectric single crystals," *Journal of Applied Physics*, **82**(4), pp. 1804–1811.

[46] Zhang, S., N. P. Sherlock, R. J. Meyer, Jr., and T. R. Shrout (2009) "Crystallographic dependence of loss in domain engineered relaxor-PT single crystals," *Applied Physics Letters*, **94**(16), 162906.
URL http://link.aip.org/link/?APL/94/162906/1

[47] Lu, Y., D.-Y. Jeong, Z.-Y. Cheng, Q. M. Zhang, H.-S. Luo, Z.-W. Yin, and D. Viehland (2001) "Phase transitional behavior and piezoelectric properties of the orthorhombic phase of $Pb(Mg_{1/3}Nb_{2/3})O_3$–$PbTiO_3$ single crystals," *Applied Physics Letters*, **78**(20), pp. 3109–3111.
URL http://link.aip.org/link/?APL/78/3109/1

[48] Guo, Y., H. Luo, T. He, and Z. Yin (2002) "Peculiar properties of a high Curie temperature $Pb(In_{1/2}Nb_{1/2})O_3$-$PbTiO_3$ single crystal grown by the modified Bridgman technique," *Solid State Communications*, **123**(9), pp. 417 – 420.

[49] Zhang, S., J. Luo, W. Hackenberger, and T. R. Shrout (2008) "Characterization of $Pb(In_{1/2}Nb_{1/2})O_3$–$Pb(Mg_{1/3}Nb_{2/3})O_3$–$PbTiO_3$ ferroelectric crystal with enhanced phase transition temperatures," *Journal of Applied Physics*, **104**(6), 064106.
URL http://link.aip.org/link/?JAP/104/064106/1

[50] Jaffe, H. and D. A. Berlincourt (1965) "Piezoelectric transducer materials," *Proceedings of the IEEE*, **53**(10), pp. 1372 – 1386.

[51] Zhang, S., J. Luo, W. Hackenberger, N. P. Sherlock, R. J. Meyer, Jr., and T. R. Shrout (2009) "Electromechanical characterization of $Pb(In_{0.5}Nb_{0.5})O_3$–$Pb(Mg_{1/3}Nb_{2/3})O_3$–$PbTiO_3$ crystals as a function of crystallographic orientation and temperature," *Journal of Applied Physics*, **105**(10), 104506.
URL http://link.aip.org/link/?JAP/105/104506/1

[52] Moffet, M. B., H. C. Robinson, J. M. Powers, and P. D. Baird (2007) "Single-crystal lead magnesium niobate-lead titanate (PMN/PT) as a broadband high power transduction material," *J. Acoust. Soc. Am.*, **121**(5), pp. 2591–2599.

[53] Sherlock, N. P., S. Zhang, J. Luo, H.-Y. Lee, T. R. Shrout, and J. Richard J. Meyer (2010) "Large signal electromechanical properties of low loss (1 - x)$Pb(Mg_{1/3}Nb_{2/3})O_3$] - x$PbTiO_3$ single crystals," *Journal of Applied Physics*, **107**(7), 074108.
URL http://link.aip.org/link/?JAP/107/074108/1

[54] Amin, A., E. McLaughlin, H. Robinson, and L. Ewart (2007) "Mechanical and thermal transitions in morphotropic PZN-PT and PMN-PT single crystals and their implication for sound projectors," *Ultrasonics, Ferroelectrics and Frequency Control, IEEE Transactions on*, **54**(6), pp. 1090 –1095.

[55] Rolt, K. D. (1990) "History of the flextensional electroacoustic transducer," *The Journal of the Acoustical Society of America*, **87**(3), pp. 1340–1349.
URL http://link.aip.org/link/?JAS/87/1340/1

[56] Hayes, H. C., "Sound Generating and Directing Apparatus," United States Patent #2,064,911, filed April 18, 1990, published March 12, 1991.

[57] Newnham, R. E., Q. C. Xu, and S. Yoshikawa, "Transformed stress direction acoustic transducer," United States Patent #4,999,819, filed April 19, 1990, published March 12, 1991.

[58] Dogan, A., K. Uchino, and R. E. Newnham (1997) "Composite piezoelectric transducer with truncated conical endcaps "cymbal"," *Ultrasonics, Ferroelectrics and Frequency Control, IEEE Transactions on*, **44**(3), pp. 597 –605.

[59] Newnham, R. E. and J. Zhang, "Flextensional metal-ceramic composite transducer," United States Patent #6,232,702, filed August 18,1999, published May 15, 2001.

[60] Zhang, J., A. C. Hladky-Hennion, W. J. Hughes, and R. E. Newnham (2001) "A miniature class V flextensional cymbal transducer with directional beam patterns: the double-driver," *Ultrasonics*, **39**(2), pp. 91 – 95.

[61] Dogan, A., E. Uzgur, D. C. Markley, R. J. Meyer, Jr., A. C. Hladky-Hennion, and R. E. Newnham (2004) "Materials for High Performance Cymbal Transducers," *Journal of Electroceramics*, **13**, pp. 403–407, 10.1007/s10832-004-5132-9.
URL `http://dx.doi.org/10.1007/s10832-004-5132-9`

[62] Newnham, R. E., J. Zhang, and R. J. Meyer, Jr. (2000) "Cymbal transducers: a review," in *Applications of Ferroelectrics, 2000. ISAF 2000. Proceedings of the 2000 12th IEEE International Symposium on*, vol. 1, pp. 29 –32 vol. 1.

[63] Ke, Y., T. Guo, and J. Li (2004) "A new-style, slotted-cymbal transducer with large displacement and high energy transmission," *Ultrasonics, Ferroelectrics and Frequency Control, IEEE Transactions on*, **51**(9), pp. 1171 – 1177.

[64] Narayanan, M. and R. Schwartz (2010) "Design, fabrication and finite element modeling of a new wagon wheel flextensional transducer," *Journal of Electroceramics*, **24**, pp. 205–213, 10.1007/s10832-008-9559-2.
URL `http://dx.doi.org/10.1007/s10832-008-9559-2`

[65] Luo, L., Y. Tang, F. Wang, C. He, and H. Luo (2007) "Displacement amplification and electric characteristics of modified rectangular cymbal transducers using electroactive materials," *Solid State Communications*, **143**(6-7), pp. 321 – 325.

[66] Luo, L., H. Wang, Y. Tang, X. Zhao, Z. Feng, D. Lin, and H. Luo (2006) "Ultrahigh transverse strain and piezoelectric behavior in (1 - x)$Pb(Mg_{1/3}Nb_{2/3})O_3$–x$PbTiO_3$ crystals," *Journal of Applied Physics*, **99**(2), p. 024104.

[67] Snyder, B., S. Lee, N. B. Smith, and R. E. Newnham (2006) "Ferroelectric transducer arrays for transdermal insulin delivery," *Journal of Materials Science*, **41**, pp. 211–216.

[68] Luis, J., E. J. Park, R. J. Meyer, Jr., and N. B. Smith (2007) "Rectangular cymbal arrays for improved ultrasonic transdermal insulin delivery," *The Journal of the Acoustical Society of America*, **122**(4), pp. 2022–2030.
URL `http://link.aip.org/link/?JAS/122/2022/1`

[69] Smith, N. B. (2007) "Perspectives on transdermal ultrasound mediated drug delivery," *International Journal of Nanomedicine*, **2**(4), pp. 585–594.

[70] Kim, H. W., A. Batra, S. Priya, K. Uchino, D. Markley, R. E. Newnham, and H. F. Hofmann (2004) "Energy Harvesting Using a Piezoelectric "Cymbal" Transducer in Dynamic Environment," *Japanese Journal of Applied Physics*, **43**(9A), pp. 6178–6183.
URL `http://jjap.jsap.jp/link?JJAP/43/6178/`

[71] Ren, B., S. W. Or, X. Zhao, and H. Luo (2010) "Energy Harvesting using a modified rectangular cymbal transducer based on 0.71$Pb(Mg_{1/3}Nb_{2/3})O_3$-0.29$PbTiO_3$ single crystal," *Journal of Applied Physics*, **107**(034501).

[72] A. Doğan and E. Uzgur (2008) "Piezoelectric Actuator Designs," in *Piezoelectric and Acoustic Materials for Transducer Applications* (Ahmad Safari and E Koray Akdoğan, eds.), Springer.

[73] Wise, S. A. (1998) "Displacement properties of RAINBOW and THUNDER piezoelectric actuators," *Sensors and Actuators A: Physical*, **69**(1), pp. 33 – 38.

[74] Cochran, Jr., J. K., "Methods for Producing Fiber Reinforced Microspheres Made from Dispersed Particle Compositions," United States Patent #4,867,931, filed February 10, 1986, published September 19, 1989.

[75] Newnham, R., S. Alkoy, A. Hladky, W. Hughes, D. Markley, R. J. Meyer, Jr., and J. Zhang (2001) "Underwater flat-panel transducer arrays," in *OCEANS, 2001. MTS/IEEE Conference and Exhibition*, vol. 3, pp. 1529 –1535 vol.3.

[76] Meyer, Jr., R. J., W. J. Hughes, T. C. Montgomery, D. C. Markley, and R. E. Newnham (2002) "Design of and Fabrication Improvements to the Cymbal Transducer Aided by Finite Element Analysis," *Journal of Electroceramics*, **8**, pp. 163–174, 10.1023/A:1020512231158.
URL `http://dx.doi.org/10.1023/A:1020512231158`

[77] Tressler, J. F. (2006) "Fabrication and Characterization of Single Crystal Cymbals," *Ferroelectrics*, **331**(1).

[78] (2005) *ATILA-6.0.0 User's Manual: Finite-Element Software Package for the analysis of 2D & 3D structures based on smart materials*, Institut Supérieur d'Electronique et du Numérique, Acoustics Laboratory.

[79] Pierce, A. D. (1991) *Acoustics: An Introduction to its Physical Principles and Applications*, published by The Acoustical Society of America through the American Institute of Physics.

[80] Kinsler, L. E., A. R. Frey, A. B. Coppens, and J. V. Sanders (2000) *Fundamentals of Acoustics*, John Wiley & Sons, Inc.

[81] Maza, V. M. (1977) *An Experimental Determination of the Dynamic Modulus of Selected Viscoelastic Materials*, Master's thesis, The Pennsylvania State University.

[82] Gabrielson, T. B. "Electroacoustic Transducers," Unpublished course notes ©2008.

[83] Fernández, J., A. Dogan, J. T. Fielding, K. Uchino, and R. E. Newnham (1998) "Tailoring the performance of ceramic-metal piezocomposite actuators, "cymbals"," *Sensors and Actuators A: Physical*, **65**(2-3), pp. 228 – 237.

[84] Sun, C.-L., S. S. Guo, W. P. Li, Z. B. Xing, G. C. Liu, and X.-Z. Zhao (2005) "Displacement amplification and resonance characteristics of the cymbal transducers," *Sensors and Actuators A: Physical*, **121**(1), pp. 213 – 220.

[85] Newnham, R. E., A. Dogan, D. C. Markley, J. F. Tressler, J. Zhang, E. Uzgur, R. J. Meyer, Jr., A.-C. Hladky-Hennion, and W. J. Hughes (2002) "Size effects in capped ceramic underwater sound projectors," in *OCEANS '02 MTS/IEEE*, vol. 4, pp. 2315 – 2321 vol.4.

[86] Howarth, T. R., J. F. Tressler, and W. L. Carney, "Lightweight Underwater Acoustic Projector," United States Patent #6,798,888, filed November 5, 2002, published September 28, 2004.

[87] Zhang, R., W. Jiang, B. Jiang, and W. Cao (2002) "Elastic, Dielectric and Piezoelctric Coefficients of Domain Engineered $0.70Pb(Mg_{1/3}Nb_{2/3})O_3$-$0.30PbTiO_3$ Single Crystal," *AIP Conference Proceedings*, **626**(1), pp. 188–197.
URL http://link.aip.org/link/?APC/626/188/1

[88] "GiD The Personal Pre and Postprocessor," ©2011 CIMNE International Center for Numerical Methods in Engineering.
URL http://gid.cimne.upc.es/